NATIONAL AERONAUTICS AND SPACE ADMINISTRATION

Technical Report 32-1587

Tracking System Analytic Calibration Activities for the Mariner Mars 1971 Mission

G. A. Madrid, C. C. Chao, H. F. Fliegel, R. K. Leavitt,
N. A. Mottinger, F. B. Winn, R. N. Wimberly,
K. B. Yip, J. W. Zielenbach

JET PROPULSION LABORATORY
CALIFORNIA INSTITUTE OF TECHNOLOGY
PASADENA, CALIFORNIA

March 1, 1974

NATIONAL AERONAUTICS AND SPACE ADMINISTRATION

Technical Report 32-1587

Tracking System Analytic Calibration Activities for the Mariner Mars 1971 Mission

G. A. Madrid, C. C. Chao, H. F. Fliegel, R. K. Leavitt,
N. A. Mottinger, F. B. Winn, R. N. Wimberly,
K. B. Yip, J. W. Zielenbach

JET PROPULSION LABORATORY
CALIFORNIA INSTITUTE OF TECHNOLOGY
PASADENA, CALIFORNIA

March 1, 1974

Prepared Under Contract No. NAS 7-100
National Aeronautics and Space Administration

Preface

The work described in this report was performed by the Mission Analysis Division of the Jet Propulsion Laboratory.

Acknowledgment

The authors wish to express their thanks to Prof. Hibberd of the University of New England, Armidale, New South Wales, Australia; to G. Levy, C. Stelzreid, B. Seidel, and B. Parham of JPL and E. Jackson and his staff at DSS 13 for their support in obtaining Faraday rotation measurements; to B. D. Mulhall of JPL and Dr. Taylor Howard of Stanford Electronic Laboratory for their cooperation in verifying the Faraday rotation measurements; to D. L. Gordon and R. Miller of JPL for providing the assistance of the appropriate operational personnel to perform the data gathering and processing functions that were so essential to the successful culmination of this task; and, of course, to the dedicated Philco-Ford operational personnel whose efforts made this report possible: Mary Montez and Gloria Smock.

Contents

The Tracking System Analytic Calibration Activity for Mariner Mars 1971: Its Function and Scope 1
G. A. Madrid

Station Locations 13
N. A. Mottinger and J. W. Zielenbach

Charged Particles 43
G. A. Madrid

The Tropospheric Calibration Model for Mariner Mars 1971 61
C. C. Chao

Time and Polar Motion 77
H. F. Fliegel and R. N. Wimberly

Calibration Effects on Orbit Determination 83
G. A. Madrid, F. B. Winn, J. W. Zielenbach, and K. B. Yip

Polynomial Smoothing of DRIVID Data 97
R. K. Leavitt

Abstract

This report describes the functions of the Tracking System Analytic Calibration activity for Mariner Mars 1971 (MM'71), its objectives for this and future missions, and the support provided to the MM'71 Navigation Team during operations. The support functions encompass calibration of tracking data by estimating physical parameters whose uncertainties represent limitations to navigational accuracy, and detailed analysis of the tracking data to uncover and resolve any anomalies. Separate articles treat the activities and results of producing calibrations for the various error sources: Deep Space Station Locations, timing and polar motion, charged particles, and the troposphere. Two other articles are also included discussing the effects of the media error sources on orbit determination and the merits of the smoothing technique used for DRIVID.

N74-16980

The Tracking System Analytic Calibration Activity for Mariner Mars 1971: Its Function and Scope

G. A. Madrid

I. Introduction

This report is the second in a series dedicated to reporting the accomplishments of the Tracking System Analytic Calibration (TSAC) activity in support of unmanned interplanetary missions. The first report (Ref. 1) described the TSAC support provided to the Mariner Mars 1969 mission; the present report discusses the calibration support provided to the Mariner Mars 1971 (MM'71) mission and evaluates the effect of calibration on spacecraft navigation. Contributions to this report are organized as a collection of articles describing the distinct calibration tasks, the calibration effects, and the data processing and operational aspects.

It is the purpose of this article to present the background information required to relate the TSAC achievements in support of MM'71 to the overall goals and plans of this activity. This information will consist of a description of the on-going TSAC development process and its objectives, along with a description of the TSAC system developed for use in support of the MM'71 mission.

During the time period covered by this report, the TSAC activity was a function of the Deep Space Network (DSN). This is the global tracking network established by the NASA Office of Tracking and Data Acquisition for two-way communications with unmanned spacecraft traveling to interplanetary distances. The DSN, which operates under the system management and technical direction of the Jet Propulsion Laboratory (JPL), at that time was comprised of three main elements. The Deep Space Instrumentation Facility (DSIF), the Ground Communications Facility (GCF), and the Space Flight Operations Facility (SFOF).[1] The tracking and data acquisition stations of the DSIF, identified as Deep Stations (DSS), are situated so that three stations may be selected approximately 120 deg apart in longitude to provide continuous coverage of distant spacecraft. The DSS serial designations and locations are listed in Table 1.

[1]Organizational changes subsequent to the flight of MM'71 have resulted in the name of the SFOF being changed to Mission Control and Computing Center (MCCC), and the MCCC's removal from DSN responsibility.

Table 1. Deep Space Station locations

Deep Space Communications Complex (DSCC)	Location	Deep Space Station (DSS)	Serial designation
Goldstone	California	Pioneer	DSS 11
		Echo	DSS 12
		Venus	DSS 13
		Mars	DSS 14
—	Australia	Woomera	DSS 41
Tidbinbilla	Australia	Weemala	DSS 42
—	South Africa	Johannesburg	DSS 51
Madrid	Spain	Robledo	DSS 61
		Cebreros	DSS 62

Ground communications among the elements of the DSN are provided by GCF links consisting of voice, teletype, and high-speed data circuits.

The SFOF is the control center for DSN operations during the flight of a deep space probe. SFOF functions include controlling the spacecraft by generating and transmitting commands, computing trajectories, determining the spacecraft orbit during flight from range and doppler data obtained from the tracking and data acquisition stations, and processing the spacecraft telemetry data from space science experiments.

The TSAC functions include the calibration of tracking data by estimating physical parameters whose uncertainties represent limitations to navigational accuracy, validation of the calibration data, utilization of these data during a mission, and detailed postflight analysis of tracking data to uncover and resolve any anomalies that may exist. TSAC is responsible for calibrations dealing with transmission media effects due to the troposphere, ionosphere, and space plasma, and with errors in locating the earth-based tracking platform such as those resulting from Earth's rotation rate as measured by Universal Time (UT1), polar motion, and tracking station locations with regard to the earth's crust. Measurements of phenomena that permit these calibrations are received from external sources and processed by software in the SFOF. The following sections indicate the methodology used in developing new techniques and software capabilities for calibrating the transmission media and platform error sources, with emphasis on the system developed to support MM'71.

II. TSAC Development Sequence

To provide calibration support geared to the increasing tracking precision demands of future unmanned missions, the TSAC activity is involved in a continuous process of development, demonstrations, and operations support. Each new capability that is provided by TSAC for use during a mission is the result of a specific sequence of activities designed to ensure that these new capabilities are developed, designed, implemented, and maintained on a schedule consistent with the needs and requirements of the utilizing missions. The following is an outline of the basic steps in that sequence:

(1) Establish a need or requirement.

(2) Develop a technique to satisfy the requirement.

(3) Demonstrate the feasibility of the technique.

(4) Demonstrate the technique operationally.

(5) Maintain the capability for the technique.

(6) Transfer the technique to operations.

These activities are shown in greater detail in Fig. 1.

The paragraphs that follow are intended to provide a greater insight into this process and, in so doing, establish clearly the breadth and scope of the activities that are properly identified as TSAC. With this background, the reader may more profitably proceed to the details of the calibration support for MM'71 as reported in the articles that follow.

The logical first step in a system engineering process is the determination of the needs or requirements to be satisfied and the selection of techniques required in such a manner as to optimize the returns from a fixed or constrained set of resources. In the TSAC system, a requirement or need to calibrate a particular error source is established by evaluating the current level at which all of the error sources affecting a radio metric signal can be calibrated and comparing these sources with the navigation accuracy requirements of the mission. The calibrations for the outstanding error sources are then selected as candidates for improvement or as objectives for developing a more precise method of calibration.

Balancing this error budget must be performed in such a way that the resultant navigation errors are minimized with a given expenditure of resources. In general, this necessitates advancing the state of the art for the most critical error sources and, within the above-listed con-

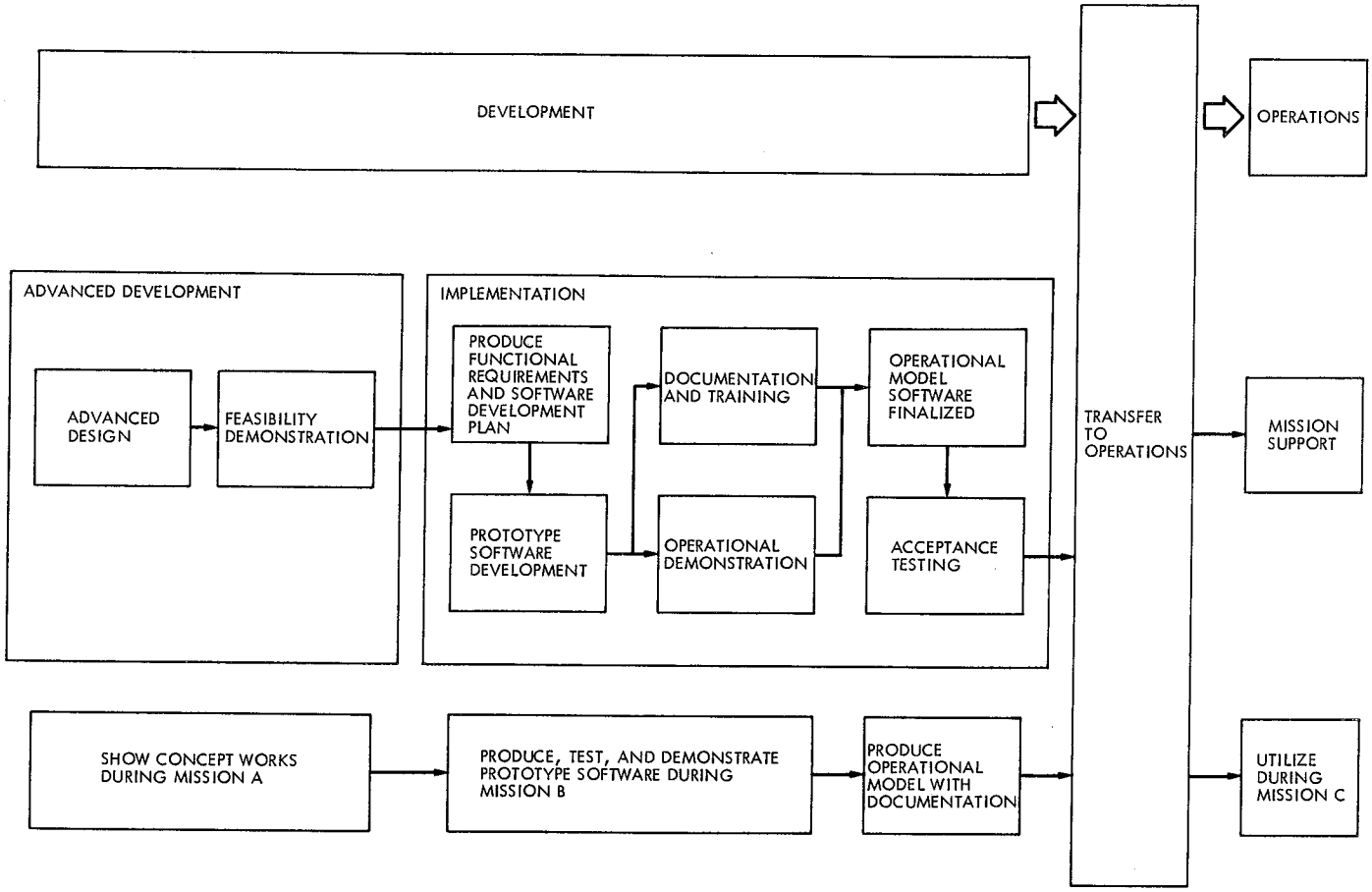

Fig. 1. Development to operations process, Tracking System Analytic Calibration

straints, reducing the effects of other error sources to a negligible level in comparison with the most critical error source.

For a mission such as Mariner Mars 1971, the tightest bounds on the allowable errors are from the navigational accuracy requirements during the Mars Orbit Insertion phase. The planned insertion maneuver required that the position of the spacecraft with respect to Mars be known to within 250 km (3σ) to place the spacecraft into the desired Mars orbit. The geometry of the orbit was of prime importance if Mariner 9 was to achieve its mapping objectives and thereby assure the success of the mission. To ensure the accuracy of the insertion, a midcourse maneuver was planned before the influence of Mars gravity was sufficient to determine the position of the spacecraft. The decision for the midcourse maneuver had to be made on the basis of the best estimate of the spacecraft trajectory obtained from the tracking data. The optimum accuracy could be extracted from these data only if errors affecting the radiometric signals could be removed.

The principal error sources that corrupt radio doppler data are listed in Table 2. These error sources can be grouped into four categories:

(1) Platform error sources. These include uncertainty in time and the location of the earth's pole, the uncertainty of the tracking station's location with respect to the earth's rotational axis, as well as the uncertainty of the station location with respect to the earth's crust.

(2) Transmission media error sources, arising from the media through which the radio signal passes. These media include the charged particles in the earth's ionosphere, in the solar wind, and in the ionospheres of other planets. The neutral medium of the lower atmosphere—the troposphere—is also an error source in this category.

Table 2. Error sources that limit doppler navigation accuracy

Tracking data error sources	Critical region for the error source	Area of improvement		Possible action/improvement	References[c]
		Hardware[a]	Software[b]		
Oscillator instability	Effect of medium-term instability [~24-h period] in α, δ is proportional to the DSS–probe distance, ρ	√		Cesium standards or better, plus appropriate cleanup loops to replace rubidium standards	Trask and Hamilton, 37-38, pp. 8–13; Curkendall, 37-41, pp. 42–47, and 37-46, pp. 4–8; Motsch and Curkendall, 37-43, pp. 37–39
Phase jitter		√		Constant design improvements improve SNR[d]	Motsch and Curkendall, 37-43, pp. 37–39
Electrical path-length variation through:					
DSS	Primarily proportional to temperature variation on external cabling between control room and antenna	√	√	Strict temperature control at equipment and active cable delay compensation	
Spacecraft	Important for target orbiter subjected to temperature fluctuations (i.e., passes through shadow)	√	√	Improved spacecraft transponder delay and preflight calibration, or active compensation	
Antenna motion:					
DSS		√	√	Basic design (structure, painting for temperature compensation) and software model of motion during a tracking pass	Motsch, 37-39, pp. 16–18
Spacecraft		√	√	Placement with respect to spacecraft CG, and control of limit cycle motion; utilize telemetry information of motion (or reject data)	
Timing:					
DSS sync to common time standard	Generally critical in support of target orbiters	√		Utilize: 1. X-band lunar bounce 2. Traveling clocks 3. Three-way ranging 4. Local "standards lab" 5. "Loran C"-type implementation	Trask and Muller, 37-39, pp. 7–16
A.1 (atomic time one)—UT1	Affects only right ascension		√	1. Improve data reduction technique (for post as well as future PZT observations)	Muller, 37-41, pp. 18–24

[a]Data user realizes benefit automatically.

[b]Data user "responsible" for incorporating improvement.

[c]References given here list the authors, issue numbers, and page numbers of articles that appeared in the Tracking and Navigation Accuracy Analysis Section of *The Deep Space Network*, a periodical publication of the JPL Space Programs Summary series; those entries preceded by a dagger list the authors, volume, and page numbers of TR 32-1526, *The Deep Space Network Progress Report*, another periodical publication of JPL.

[d]Signal-to-noise ratio.

Table 2 (contd)

Tracking data error sources	Critical region for the error source	Area of improvement		Possible action/improvement	References[c]
		Hardware[a]	Software[b]		
Timing:					
A.1 (atomic time one)—UT1 (contd)				2. New method for determining A.1—UT1, such as use of interferometric tracking of distant radio sources	
	Data accuracy		√	Improved source data	Fliegel and Lieske, 37-62, pp. 46–49; †Fliegel, V, pp. 66–74
Precession, nutation (spin axis with respect to inertial space)			√	Further reduction of available data and use of interferometric tracking of distant radio sources	
Pole motion (earth's crust with respect to spin axis)			√	1. Improve predictions a. "Hattori" model b. Sequential estimation technique	Muller, 37-45, pp. 10–14; Chao and Muller, 37-56, pp. 69–74
				2. Reduce time interval over which predictions must be extrapolated (reduce lag between observations and availability of results)	
				3. New method for determining polar motion, such as use of interferometric tracking of distant radio sources	
				4. Polar satellite	Chao and Fliegel, 37-66, pp. 23–26
Charged particles:					
Ionosphere	Worst effect at sun–earth probe angle SEP = 90°		√	Utilize ionosonde data, Faraday rotation data from spacecraft or earth satellites, dual frequency, group vs phase velocity technique (DRVID), empirical model, etc.	Trask and Efron, 37-41, pp. 3–12; Liu, 37-41, pp. 38–41; Winn, 37-53, pp. 20–25; Webb and Mulhall, 37-55, pp. 13–15; Mulhall and Thuleen, 37-55, pp. 15–19; Mulhall and Wimberly, 37-55, pp. 19–23; Mulhall and Wimberly, 37-56, pp. 58–61; Ondrasik and Mulhall, 37-57, pp. 29–42; Mulhall, 37-57, pp. 24–29; Mulhall, 37-58, pp. 66–73; Ondrasik, 37-59, pp. 97–110; Ondrasik, Mulhall, and Mottinger, 37-60, pp. 89–95; Madrid, 37-60, pp. 95–97; Mulhall and

Table 2 (contd)

Tracking data error sources	Critical region for the error source	Area of improvement		Possible action/improvement	References[c]
		Hardware[a]	Software[b]		
Charged particles: Ionosphere (contd)					Stelzreid, 37-64, pp. 21–25; Mulhall, 37-64, pp. 25–27; Mulhall and Thuleen, 37-65, pp. 35–40; †Miller and Mulhall, V, pp. 58–66
Space plasma	Worst at SEP = 0 and effect increases with ρ. Little increase above ρ = 5 AU and most of the effect by ρ = 3 AU		√	Dual frequency and DRVID techniques	Mulhall and Wimberly, 37-56, pp. 58–61; Efron and Lisowski, 37-56, pp. 61–69; Anderson, 37-58, pp. 77–81; Ondrasik, Mulhall, and Mottinger, 37-60, pp. 89–95; Reynolds, Mottinger, and Ondrasik, 37-62, pp. 24–28; †MacDoran, Callahan, and Zygielbaum, I, pp. 14–22; †von Roos, III, pp. 71–77; †von Roos, VI, pp. 46–57
Tropospheric refraction	Worst at low elevation angles γ, but deletion of data at low γ degrades ability to determine α, δ		√	Model based on: 1. Average local conditions at DSS	Liu, 37-50, pp. 93–97; Mottinger, 37-50, pp. 97–104; Winn, 37-51, pp. 42–50
				2. Local atmospheric measurements near DSS	
				3. Radiosonde measurements	Ondrasik and Thuleen, 37-65, pp. 24–25; †Winn and Leavitt, I, pp. 31–41; †Miller, Ondrasik, and Chao, I, pp. 22–31; †Chao and Moyer, III, pp. 63–71; †Chao, VI, pp. 67–83; †Thuleen and Ondrasik, VI, pp. 83–99; †von Roos, VI, pp. 99–102; †Chao, VI, pp. 57–67
	Influence on Doppler	√	√	4. Surface weather	Berman, 37-65, pp. 140–153
Software			√	Replace SPODP[e] with DPODP[f], incorporating above model improvements	Moyer, issues 37-38, -39, and -41 through -46; Warner, 37-47, pp. 35–41
			√	MEDIA calibrations	†Madrid, III, pp. 52–63

[e]Single Precision Orbit Determination Program.

[f]Double Precision Orbit Determination Program.

Table 2 (contd)

Tracking data error sources	Critical region for the error source	Area of improvement		Possible action/improvement	References[c]
		Hardware[a]	Software[b]		
DSS locations			√	Statistically combine results of several missions, utilizing above improvements	Vegos and Trask, 37-43, pp. 18–24; Mottinger and Trask, 37-48, pp. 12–22; Mottinger, 37-49, pp. 10–23, and 37-56, pp. 45–58; Mottinger, 37-62, pp. 41–46; †Ondrasik and Mottinger, IV, pp. 71–80

(3) Error sources related to the spacecraft and ground equipment (not discussed in this report). Included in this category are variations of the effective path through the microwave equipment in the spacecraft and at the tracking station, and drift in the frequency system that controls the frequency of the S-band signal.

(4) Errors in the ephemerides of the earth, moon, and target planet.

A variance circle comparison of the errors is useful in evaluating the relative importance of the various types of errors. The variance circles in Fig. 2 are intended to compare the value of the errors for MM'69 and MM'71. These diagrams are scaled so that the area of the circle allocated to each error source is proportional to the variance contribution of that error source. The variance circles are given in terms of the uncertainty in right ascension (α) and declination (δ) of the spacecraft. These coordinates correspond to a right-handed system in which the α-δ plane lies normal to the line of sight between the earth and the spacecraft.

Errors in locating the station in longitude dominate the overall right ascension uncertainties σ_α^2 with UT1, polar motion, and ephemeris errors being the next most dominant set. The transmission media errors and ground station errors exert a greater influence on the declination variance ($\sigma_\delta^2 \tan^2 \delta$) and, for MM'71, can be considered to be evenly balanced with all the platform errors except for the DSS location error source, which is still by far the dominant error. The ephemeris and ground system errors are not a TSAC system responsibility, but their effect on the overall error must be taken into account in evaluating the relative importance of the errors for which TSAC is responsible.

Improvements in UT1 and polar motion indicate that a high priority should be allocated to the improvement of the locations of the stations. In the past this information has been gleaned from the tracking data of prior missions but a point of diminishing returns has been reached using this technique so that dramatic improvements are not foreseen. The recent development of the Very Long Baseline Interferometry (VLBI) technique (Ref. 2) and the successful initiation of a series of tests to prove its feasibility (Ref. 2) have increased hopes of obtaining at least a factor of two improvement in station locations by permitting a coordinate tie between the ill-defined stations (i.e., overseas) and the better defined stations (i.e., Goldstone). Combining this technique with the present methods should permit the platform errors to be more equally balanced with the transmission media and ground system errors.

The development of the software systems required to utilize technological advances is also a TSAC objective. Aside from the VLBI example, new approaches to measuring the columnar water vapor content along the line of sight of the radar antenna (system noise temperature measurements[2]) are being evaluated for possible incorporation into the TSAC system. This innovation, it is felt, would permit the calibration of short- and long-term tropospheric effects to the 0.25-m level (currently only long-term effects are calibratable to the 0.5-m level). Under development for the post-MM'71 era is a capability to utilize dual-frequency observables (range,

[2]These techniques involve the passive sensing of water vapor radiation effects along the line of sight in received frequencies in the S, X, or K bands. If the results of investigations in these bands are positive then it is possible that these techniques could be utilized using current DSN equipment. If not, additional equipment would be required and the costs could be prohibitive.

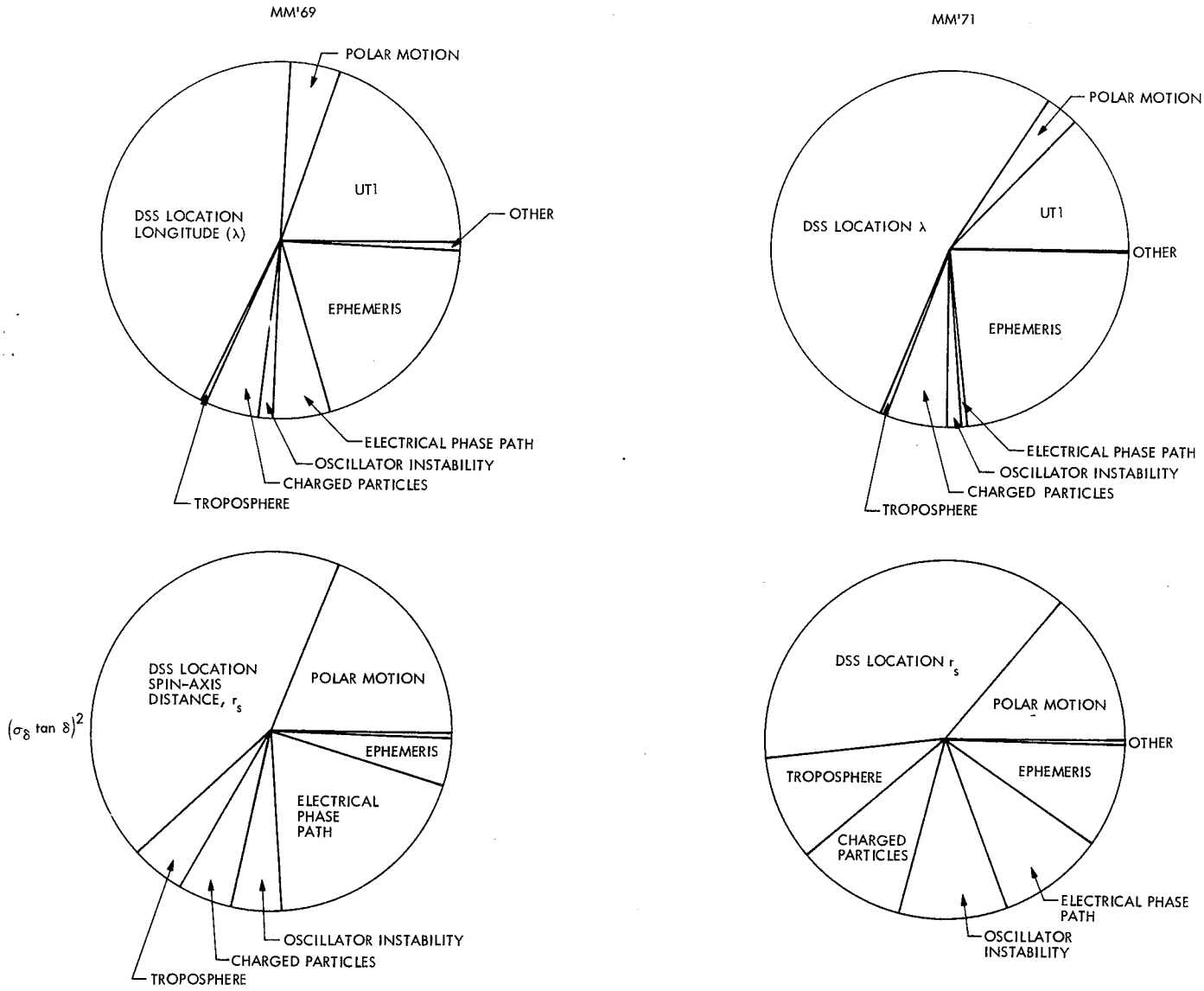

Fig. 2. Variance circle comparison of plane of sky errors from a Goldstone station: MM'69 vs MM'71

doppler) as a means of calibrating charged particle effects on the radio signal.

Once a technique has been selected for implementation as an operational support package, a prototype software element is developed and tested in an operational environment during a mission. If the operational demonstration is successful, the element is eligible for conversion to operational status after it has been integrated with the operational TSAC system and the necessary training and documentation have been provided. A capability that has been demonstrated operationally but not committed for mission support is placed on "engineering sustenance" status; i.e., it may be unofficially maintained and operated during a mission to provide a capability that may be required later.

The transfer of a TSAC capability to operations and its successful use during a mission is the culmination of the development effort. Capabilities so transferred become a fixed part of the TSAC operational capability repertoire and are available for commitment to mission support.

III. MM'71 TSAC System

The prime objective of the MM'71 TSAC system design was to provide to MM'71 flight operations a set of cali-

Table 3. MM'71 calibration techniques and expected accuracy

Calibration technique	Source	Form of calibrations	Accuracy	Type of commitment
DSS location	Postflight analysis	Station locations	DSS 12, 14: $\sigma_{r_s} = 0.6$ m, $\sigma_\lambda = 2.0$ m	Best efforts
Timing (UT1)	BIH	Interpolation tables	4 ms	Best efforts
Polar motion	BIH	Interpolation tables	$\sigma_x = 0.7$ m, $\sigma_y = 0.7$ m	Best efforts
DRVID	DSS 14	Polynomials	$\sigma_{\Delta\rho/\text{pass}} = 1.0$ m	Operational demonstration
Surface weather	Near all DSS	Polynomials	$\sigma_{\Delta\rho/\text{pass}} = 0.5$ m	Best efforts
Faraday rotation data	DSS 13, Stanford Armindale	Polynomials	$\sigma_{\Delta\rho/\text{pass}} = 2$ m	Best efforts

brations for the station platform and the transmission media that was consistent with the mission targeting objectives. The calibration techniques to be provided, their source, presentation format, accuracy, and level of commitment are listed in Table 3.

The design of the TSAC processing system to produce the required calibrations for transmission media effects (troposphere, ionosphere, and space plasma) and platform location inaccuracies (DSS locations, time, polar motion) inherent in the radio metric data from the MM'71 spacecraft is shown in Fig. 3. The function of this system is to collect and process measurements of the phenomena affecting the information content of the tracking data and to produce a suitable set of calibrations for use in the orbit determination process.

The central elements of the TSAC processing system for MM'71 were two computer programs operated in the Univac 1108 computer prior to the orbit determination process. One of these programs was the Transmission Media Calibration Program (MEDIA), which was responsible for the processing of troposphere and charged particle measurements and the production of a set of polynomials from which the doppler observable could be calibrated by the Orbit Determination Program (ODP). The other TSAC program was the Platform Observable Calibration Program (PLATO); its function was to process time and pole information so as to produce a set of tables to compensate for the lack of uniformity in Universal Time (UT1) and to correct for the motion of the pole about the spin axis.

The data processed by the system originated at various sources; some within the DSN and some external to it. The Differenced - Range - Versus - Integrated - Doppler (DRVID) data, for example, were provided by the DSIF from two of its stations (DSS 12 and DSS 14), whereas the time and polar motion information was provided by the Bureau International de l'Heure (BIH) in Paris, France. DRVID from DSS 14 was provided using the Tau ranging system, and that from DSS 12 was provided using the Mu ranging system. Table 4 lists the complete set of inputs to the MM'71 TSAC system and tabulates their sources and collection rates.

Information regarding the location of the Deep Space Tracking Stations (DSS) was obtained from an analysis of prior missions and from surveys tying together all of the stations in each complex. Since there are no specific hardware or software elements that can be identified with this calibration procedure, it is not represented in the system diagram (Fig. 3).

The seasonal troposphere models prepared prior to launch were empirical models of the signal delay due to the wet and dry components of the troposphere as measured at the zenith. The troposphere components were obtained from past measurements of pressure, temperature, and relative humidity at DSS sites and/or nearby facilities that could provide these data. Radiosonde measurements were used to model the mapping of the corrections to the elevation angle of the MM'71 spacecraft.

Measurements for the time (UT1) and polar motion corrections were obtained from the BIH in Paris, France, and consist of a reduction of observations taken at observatories around the world. The BIH reports were received on a weekly basis during cruise and on a daily basis at critical events (for example, prior to orbit insertion).

Charged particle measurements were obtained using the DRVID technique (Ref. 3) and the Faraday rotation

Table 4. MM'71 TSAC system inputs

Calibration application	Input data type	Input data units	Origin/source	Reception/collection rate
DSS locations	Distance from spin axis Longitude Z component	Meters Degrees Meters	Postflight analysis of prior missions	Prior to launch and as required
UT1	A.1—UT1	Milliseconds	BIH	Weekly (cruise) Daily (MOI)
Polar motion	ΔZ coordinate ΔY coordinate	Meters Meters	BIH	Weekly (cruise) Daily (MOI)
Troposphere	Altitude Pressure Temperature Relative humidity	Feet Millibars °C %	Seasonal model using surface measurements from DSS sites; elevation mapping models using radiosonde data from nearby sites	Prior to launch
Ionosphere charged particles	Electron content	Electrons/m^2	Faraday polarimeters DSS 13, Stanford, Armindale	Sampled daily; sent in 1-week batches
Ionosphere and space plasma charged particles	Round-trip path change due to electron content	Meters	DRVID using Tau ranging at DSS 14	Sampled at 2-min rate during range and doppler tracking
	Round-trip path change due to electron content	Meters	DRVID using Mu ranging at DSS 12	Sampled at 1- and 2-min rate during range and doppler tracking

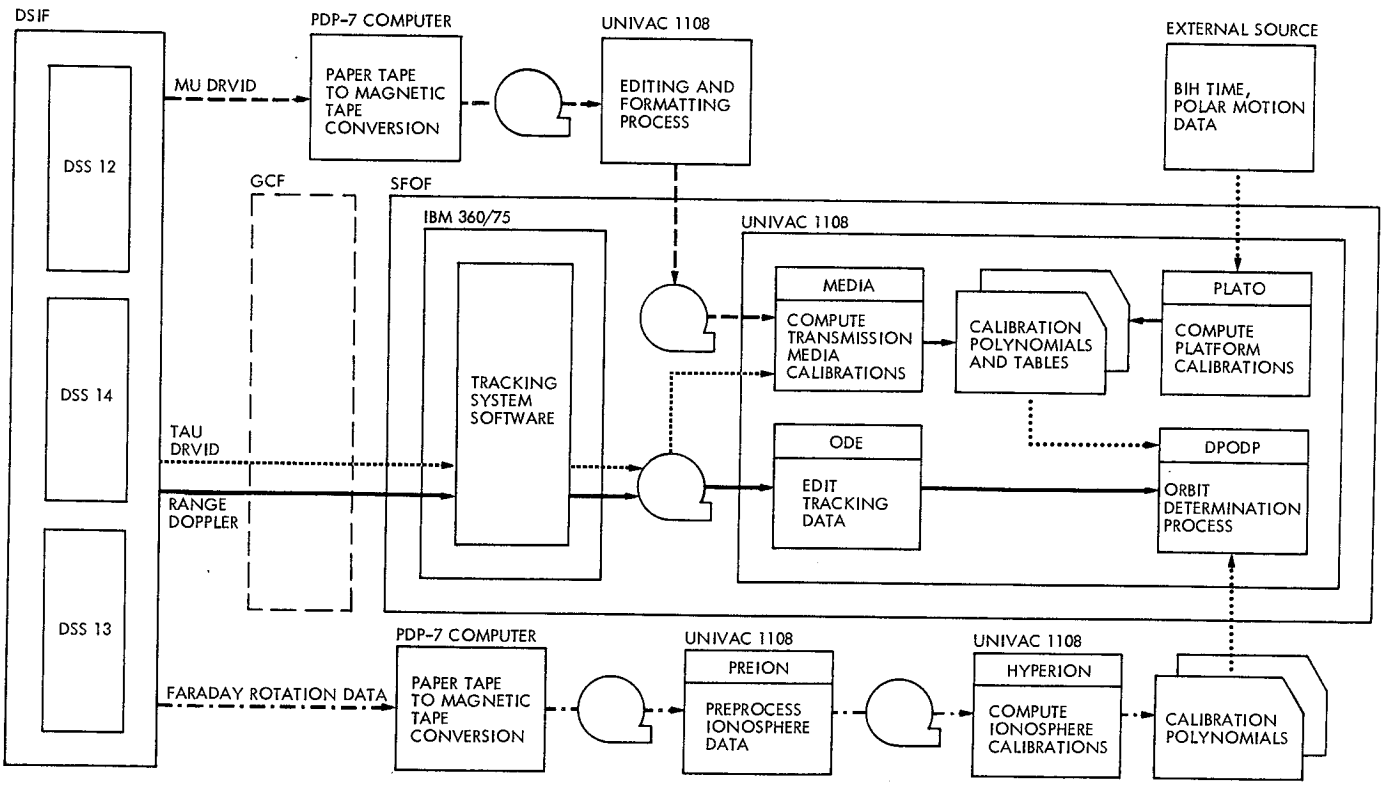

Fig. 3. Processing system and data flow, MM'71 TSAC support

technique (Ref. 1). The DRVID data provided an accurate measure of the rate of change of electrons in the signal ray path; this includes ionospheric particles as well as those associated with plasma effluents from the sun. Faraday rotation data, which measures the electrons in the ionosphere, were available from DSS 13, Stanford University, and Armidale, Australia,[3] utilizing the linearly polarized signal from the ATS-3 and INTELSAT 1 satellites. This type of data was very useful in filling gaps in the DRVID coverage.

The in-flight operational sequence for the charged particle calibrations began with the reception of range and doppler information from DSS 14, DRVID information from DSS 12, and Faraday rotation data from DSS 13. The DSS 14 data represented observations taken once per minute during passes averaging about 6 hours and transmitted from DSS 14 to the SFOF in standard tracking data format via teletype lines. The received data were processed by the SFOF tracking system software in the IBM 360/75, and a magnetic tape file called the tracking data file was prepared for input to the Orbit Data Editor (ODE) and thence to the Double Precision Orbit Determination Program (DPODP) in the Univac 1108. (MEDIA makes use of this file to compute a DRVID point for every concurrent range and doppler point.) These DRVID points were smoothed to produce a polynomial for each tracking pass; the polynomials were then provided to flight operations in the form of IBM cards for their use in calibrating the doppler observables over corresponding passes of data.

The DRVID calibrations produced from the data received from DSS 12 were treated by MEDIA in a similar manner, the important difference being in their mode of presentation to MEDIA. The data from DSS 12 were transmitted to the SFOF as nonstandard messages over a teletype line where it can be retrieved only in paper tape format. This paper tape was first converted to another format and edited to remove gross errors in the transmission. Only then was the DRVID data from DSS 12 ready for input to MEDIA.

Reduced UT1 and polar motion data were received from the BIH as a printed teletype message. This message was then keypunched into a specified format and submitted to the PLATO programs for processing. A set of interpolation tables incorporating the time and pole corrections was prepared in the form of cards and presented to the flight operations team for input to the Orbit Determination Program.

Faraday rotation data were received in batches of a week's collection of data on paper tapes. These were converted to magnetic tapes, edited, and preprocessed, and calibrations were computed using the program HYPERION. The time lag inherent in this process (typically 4 to 8 days) precluded its use in near-real-time situations.

[3]These data were made available by Professor Hubbard of the University of New England, Armidale, Australia, under a contract to the Deep Space Network.

References

1. Mulhall, B. D., et al., *Tracking System Analytic Calibration Activities for the Mariner Mars 1969 Mission*. Technical Report 32-1499, Jet Propulsion Laboratory, Pasadena, Calif., Nov. 15, 1970.
2. Fanselow, J. L., et al., "The Goldstone Interferometer for Earth Physics," in *The Deep Space Network Progress Report for January and February 1973*. Technical Report 32-1526, Vol. XIV, pp. 45–57. Jet Propulsion Laboratory, Pasadena, Calif., Apr. 15, 1973.
3. MacDoran, P. F., "A First-Principles Derivation of the Differenced Range Versus Integrated Doppler (DRVID) Charged-Particle Calibration Method," in *The Deep Space Network*, Space Programs Summary 37-62, Vol. II, pp. 28–33. Jet Propulsion Laboratory, Pasadena, Calif., Mar. 31, 1970.

Station Locations

N. A. Mottinger and J. W. Zielenbach

I. Introduction

The process of providing station location estimates for use by the orbit determination team extends beyond the responsibility of providing an acceptable set of locations at launch. This extended responsibility is required because some significant model parameters such as the final planetary ephemeris produced to support the encounter phase of a mission may not be available until several months after launch. As a result several station location sets may be required during the course of a mission. Section II of this article provides a history of the station location sets provided to MM'71 and Section III indicates the complexity of the analysis that preceded the determination of the final Location Set (LS).

II. Station Locations Supplied for Launch and Cruise Phases of Mariner 9

This section discusses the different station location sets provided for MM'71 navigation support. It briefly describes each set, gives the basis for its construction, and compares it with the final set, LS 35.

During the period from January 1 to October 20, 1971, three different station location sets were recommended for use by the MM'71 project. Each was an improvement over its predecessor, representing more a change in software and physical models than the amount of radio tracking used for the solutions. The project needed versions of these sets with and without charged particle calibrations, for reasons discussed below. Table 1 summarizes the different sets provided and also indicates which orbit determination program, ephemeris, source of Universal Time (UT1), polar motion, troposphere model, or ionosphere calibration was used.

A. Stepwise Progression of Solutions

The final set, LS 35, was the latest step in an evolutionary sequence that involved a series of intermediate station location solutions. New software was introduced several months before the Mariner 9 launch and, as the mission progressed, additional improvements became available that prompted new solutions. Changes in the models, including planetary ephemerides, parameters like UT1 and polar motion, which affect the orientation of the earth, and calibrations for neutral and charged particles

Table 1. Station location summary

Location set	Date delivered	Program	Ephemeris	UT1	Polar motion	Troposphere	Ionosphere calibration	Mariner missions used
LS 26	July 21, 1969	DPODP 5.1	DE 69	Richmond	BIH	Cain 2[a]	Yes	4, 5
LS 27	July 21, 1969	DPODP 5.1	DE 69	Richmond	BIH	Cain 2[a]	No	4, 5
LS 28	Dec. 29, 1970	DPODP 5.1	DE 69	Richmond	BIH	Cain 2[a]	Yes	4, 5
LS 32[b]	Oct. 12, 1971	SATODPC 1.0	DE 78	BIH	BIH	Chao	No	4, 5, 6
LS 33[b]	Oct. 12, 1971	SATODPC 1.0	DE 78	BIH	BIH	Chao	Yes	4, 5, 6
LS 35[c]	Oct. 20, 1971	SATODPC 1.0	DE 78	BIH	BIH	Chao	Yes	4, 5, 6
LS 36	Oct. 20, 1971	SATODPC 1.0	DE 78	BIH	BIH	Chao	No	6

[a]DPODP 5.1 used Cain 1, but the combined solution was augmented to represent the Cain 2 model.

[b]Mariners 4 and 5 longitudes were averaged, but the combination program of Ref. 2 was not used.

[c]Mariner 4 absolute longitude was off-weighted.

in the troposphere and ionosphere also required making new station location solutions.

In such an environment, it is important to be able to trace one's steps from one solution to another. First it is necessary to determine if the new software gives the same station location estimates as the previous software did when the same models are used. Although this does not guarantee correctness, it ensures that estimated station locations are software-independent, as indeed they must be. After this step, parameters are changed in the model, one at a time. For example, changing the ephemeris and holding all other model parameters fixed should produce a calculable effect on station locations. These checks have shown that to 3.6×10^{-3} arc seconds (0.13 m) and better the station location changes agree with the shifts of target bodies. Next, one might change another parameter like UT1. Such careful checking could not be done to all data packages in the time available, but it was done very thoroughly on Mariner 4 so that confidence was established in the new software and model parameters. The end result of this was a set of solutions from individual missions that were determined using: (1) the same program, (2) the same planetary ephemeris, Development Ephemeris (DE) 78 for this mission, and (3) the same sources for UT1, polar motion, and troposphere models as the navigation team was using to process the Mariner 9 tracking data.

B. LS 28

This was the first set derived for the MM'71 project. Delivered January 1, 1971 (Ref. 1), it was based on reduction of Mariners 4 and 5 data using the Double Precision Orbit Determination Program (DPODP) and ionosphere calibrations applied by program MODIFY. The ionosphere corrections were improved over those used for MM'69 in two regards: the doppler corrections were computed using an exact "four-leg" differenced range doppler algorithm instead of some earlier approximations, and actual measurements were used in places where they were previously missing and had been estimated from other available sources. A program described in Ref. 2 combined the solutions using their associated normal matrices, exactly as was done for LS 25 (Ref. 3). Since the DPODP used an old (Cain 1, Ref. 4, p. 69) troposphere model, the increments derived in July 1969 by V. J. Ondrasik and appearing in Table 11, p. 27 of Ref. 4, were used to create the spin-axis solutions of LS 28. Note that LS 28 contained charged particle calibrations.

C. Locations Used for Launch

Although it was planned to launch the mission with a set produced by the Satellite Orbit Determination Program (SATODP), the May 1 delivery date could not be met due to extra time required to check the new program and its models with the previous program. The Project desired a set of locations that could be used when no charged particle calibrations were available, and since no such set was available corresponding to LS 28, it used LS 27 from the LS 26–27 pair. These were solutions with and without ionosphere calibrations, derived by adding Ondrasik's increments to LS 25 and 24 respectively (the derivation of LS 24–25 is discussed on pp. 19–32 of Ref. 4).

Even though all these sets were based upon DE 69 and UT1 from the Richmond, Florida, substation of the United States Naval Observatory (USNO), they were deemed adequate for supporting the early phases of the MM'71 missions.

D. LS 32–33

After resolution of the differences between old and new software and models, reduction began in earnest for the final location set to support the encounter and orbiting phases of the mission. Until DE 78 became available on September 30, analysis was performed using its predecessor, DE 77. DE 78 was to be the final ephemeris for the remainder of the cruise and approach phases of this mission, and although a new ephemeris was eventually provided, it did not cause a noticeable change in station locations. Mariners 4, 5, and 6 data were reduced using DE 78, Bureau International de l'Heure (BIH) UT1 and polar motion, and the new Chao (Refs. 5 and 6) troposphere model. The results of this analysis are presented with more detail in Section III of this article; it will suffice to say here that after the ionosphere calibrations were applied, the spin-axis and relative longitude solutions were the most consistent ever obtained. However, the absolute longitudes differed by 16 m between Mariner 4 and the other Mariner missions.

LS 32 and LS 33 were produced on October 12 to provide the project some estimate of the station locations based upon DE 78, BIH time and pole, and the latest troposphere model, until a decision could be made for handling the Mariner 4 longitudes. The former was derived without ionosphere calibrations, the latter with them. It should be noted that these were the first sets developed using data from Mariner 6. Other pertinent facts about them are recorded in Table 1.

Due to preoccupation with the Mariner 4 problem, a very simple technique was used to combine the solutions for LS 32 and LS 33. The Mariners 4 and 5 encounter estimates for the longitude of DSS 12 were averaged. Then, by using all three Mariner missions, average relative longitudes were computed for the remaining stations and added to the DSS 12 longitude to obtain their absolute longitudes. Spin-axis solutions came from averaging the solutions available at each site. At the Goldstone and Madrid complexes, the adjacent station solutions were constrained to be consistent with the relative coordinates of the stations as determined from geodetic surveying. This technique was used first on the nonionosphere-calibrated location solutions to produce LS 32 and then on the calibrated ones to obtain LS 33.

E. LS 35

The technique of averaging the Mariners 4 and 5 longitudes was not completely adequate because the mean longitude thus obtained was still in disagreement with the remaining values by more than 3 m. A better means was needed to resolve the problem, and many different avenues were investigated.

If the Mariners 4 and 6 longitude solutions had agreed and Mariner 5 were 16 m different, one could blame the difference on a mean anomaly error for either the Martian or Venusian ephemerides, or both. However, Mariners 5 and 6 agreed and Mariner 4 was standing off. This is very difficult to attribute to an ephemeris error because the relative positions of Mars would have to be inconsistent by 1/2 arc second between 1965 and 1969. This is unlikely since the relative positions of Mars are some of the best determined quantities in the planetary ephemeris.

Extensive studies were performed using cruise and encounter data from the Mariners 5 and 6 missions to observe the general behavior of station location estimates as the data arc increased through cruise and into encounter. Such missions offered the advantage of having the encounter data to give a final longitude estimate. It was hoped that the in-flight Mariner 9 station location estimates might follow the pattern set by Mariner 6, another Mars mission in which solutions obtained during cruise were west of the ones using encounter data. The Mariner 9 solutions were in fact running about 6 m west of the existing Mariners 5 and 6 encounter longitudes, so on the assumption that the Mariner 6 experience would repeat, the Mariner 4 longitudes were labeled extraneous and were not used in the combination of estimates. Since relative longitudes and spin axes were not questionable, they were used as described in Section III of this article to form LS 35. This was delivered on October 20, 1971.

LS 35 was the combined estimate based on individual solutions whose data were calibrated for ionosphere effects. This set of solutions was used just prior to encounter. The project still desired a solution that could be used when no calibrations were available, as would be the case in real-time encounter support. The best way to obtain such an estimate is not to combine all the uncalibrated solutions, but rather to assess the amount of charged particles present during that season and time of

day in that hemisphere and apply an equivalent station location increment to the calibrated values. Because such equivalent station location corrections were not available at the time, the navigation team chose to use the non-ionosphere-calibrated locations from Mariner 6 that had been generated on DE 78 with BIH time and pole, and with the latest troposphere model. This set is called LS 36.

Tabulations of the major sets, LS 27, 32, 33, 35, and 36, are given in Tables 2 and 3. Table 4 contains the station-by-station differences in each coordinate and the rms value of such differences for all stations between LS 35 and the other sets.

III. Details in the Development of Location Set 35

The MM'71 orbit determination program (SATODP C 1.0) was used with DE 78 on the Mariners 4, 5, and 6 data to obtain new estimates of station locations for the DSN. The Hamilton–Melbourne (Ref. 7) expression for the information content in doppler data indicates that two geometries are especially useful for such work: (1) the zero declination case where one estimates distance off the spin axis (r_s) and relative longitude, and (2) the encounter phase where one obtains r_s and absolute longitude. Encounter data from each of the three missions provide estimates of absolute longitude and r_s. Mariner 5 offers two zero-declination passages, one during cruise prior to encounter and the other after encounter.

The SATODP was used to produce two sets of station locations: those with ionospheric calibrations, and those without. Comparison of these sets left no doubt that the new combined solution should involve the calibrated values. The resulting set, LS 35, was recommended for project use, and represents the new JPL "best" station locations. This section documents the formation of LS 35. It indicates all the pertinent input data and presents the solutions with and without calibrations.

A. Data Used

The data packages are basically the same as those used for the previous solution set, LS 25 (Ref. 3). Tables 5 and 6 present pertinent information for each package analyzed, including the number of points in the solutions made with and without ionosphere calibrations. The useful Mariner 6 data stopped at $E - 45$ min due to degradation by a gas-venting cooling operation. Some of the other packages lost considerable amounts of data (up to 48%) because of insufficient charged particle data, but in general, the loss of data did not appear to be detrimental to the solutions. The exception was the Mariner 5 encounter, where DSS 41 lost all but two passes involving 36 points with 10-min count times.

B. Timing and Polar Motion

For the first time in the station location work, both UT1 and polar motion were derived from BIH data. In LS 25, BIH pole positions were used, but the USNO Richmond substation provided the UT1 data. The software that produces the polynomial coefficients that represent this data also was improved (Ref. 8).

The new timing moved the longitude solutions for Mariner 4 by 4.7 m, for Mariner 5 by 2.0 m, and for Mariner 6 by 3.7 m, all eastward.

C. Troposphere

SATODP C1.0 provides for a more generalized troposphere model, including both wet and dry components of the refractivity. The wet and dry zenith range delays may be specified as polynomial functions of time for the various stations, and the functions for mapping from zenith to lower elevations can now be input as tables. The origin of the values in this new model is discussed in Refs. 5 and 6.

Although this model is more accurate at lower elevations than previous models, to be consistent with previous analysis, no data below 15 deg was used. For the Mariner 4 encounter case, the differences between station locations determined with the Cain 1 model (Ref. 4, p. 69) and the Chao model (Refs. 5 and 6) are shown in Table 7.

D. Ionosphere

The procedures for modeling the ionospheric effects also underwent change for MM'71. In the past, the programs (Ref. 4) that produced calibration polynomials would extrapolate outside the regions where charged particle measurements were available. Now no extrapolation is done and specially generated control inputs ("delete cards") ensure that no uncalibrated data enters the solutions. In addition, the SATODP itself computes the doppler effect from the range delay, which allows for greater accuracy, since the count time, light time, and ray path are usually known better there than in the program that generates the calibrations.

Table 2. Station locations

Location set	DSS	R, km[a]	ϕ, deg[b]	λ, deg[c]	r_s, km[d]	z, km[e]	x, km[e]	y, km[e]
27	11	6372.0088	35.208047	243.150637	5206.3386	3673.763	−2351.4240	−4645.0799
	12	6371.9931	35.118670	243.194568	5212.0502	3665.628	−2350.4374	−4651.9793
	14	6371.9920	35.244357	243.110523	5203.9957	3677.052	−2353.6159	−4641.3429
	41	6372.5568	−31.211431	136.887540	5450.1992	−3302.243	−3978.7199	3724.8435
	42	6371.7104	−35.219658	148.981304	5205.3502	−3674.646	−4460.9809	2682.4093
	51	6375.5254	−25.739297	27.685441	5742.9418	−2768.744	5085.4422	2668.2687
	61	6370.0240	40.238920	355.751018	4862.6050	4114.885	4849.2401	−360.2742
	62	6369.9648	40.263212	355.632211	4860.8148	4116.908	4846.6977	−370.1923
32	11	6372.0088	35.208046	243.150663	5206.3386	3673.763	−2351.4219	−4645.0810
	12	6371.9982	35.118669	243.194595	5212.0503	3665.628	−2350.4353	−4651.9805
	14	6371.9920	35.244357	243.110549	5203.9956	3677.052	−2353.6138	−4641.3439
	41	6372.5577	−31.211416	136.887578	5450.2002	−3302.243	−3978.7231	3724.8416
	42	6371.7107	−35.219656	148.981325	5205.3506	−3674.646	−4460.9822	2682.4080
	51	6375.5244	25.739301	27.685468	5742.9407	−2768.744	5085.4400	2668.2705
	61	6370.0249	40.238914	355.751057	4862.6061	4114.885	4849.2415	−360.2709
	62	6369.9657	40.263206	355.632250	4860.8159	4116.908	4846.6990	−370.1891
33	11	6372.0105	35.208036	243.150653	5206.3407	3673.763	−2351.4236	−4645.0824
	12	6371.9948	35.118659	243.194585	5212.0523	3665.628	−2350.4370	−4651.9819
	14	6371.9936	35.244346	243.110539	5203.9977	3677.052	−2353.6155	−4641.3453
	41	6372.5608	−31.211399	136.887572	5450.2039	−3302.243	−3978.7254	3724.8445
	42	6371.7109	−35.219656	148.981317	5205.3508	−3674.646	−4460.9820	2682.4087
	51	6375.5251	−25.739298	27.685451	5742.9415	−2768.744	5085.4415	2668.2694
	61	6370.0259	40.238905	355.751038	4862.6075	4114.885	4849.2428	−360.2727
	62	6369.9668	40.263197	355.632231	4860.8173	4116.908	4846.7003	−370.1908
35	11	6372.0106	35.208035	243.150578	5206.3408	3673.763	−2351.4298	−4645.0794
	12	6371.9949	35.118658	243.194509	5212.0524	3665.628	−2350.4432	−4651.9788
	14	6371.9937	35.244346	243.110463	5203.9977	3677.052	2353.6216	−4641.3422
	41	6372.5595	−31.211406	136.887488	5450.2023	−3302.243	−3978.7188	3724.8492
	42	6371.7112	−35.219654	148.981250	5205.3511	−3674.646	−4460.9792	2682.4140
	51	6375.5253	−25.739297	27.685392	5742.9417	−2768.744	5085.4445	2668.2642
	61	6370.0264	40.238902	355.750962	4862.6081	4114.885	4849.2429	−360.2791
	62	6369.9672	40.263194	355.632155	4860.8179	4116.908	4846.7004	−370.1972
36	11	6372.0073	35.208056	243.150588	5206.3368	3673.763	−2351.4271	−4645.0762
	12	6371.9916	35.118679	243.194520	5212.0484	3665.628	−2350.4405	−4651.9757
	14	6371.9899	35.244370	243.110480	5203.9931	3677.052	−2353.6182	−4641.3388
	41	6372.5583	−31.211413	136.887477	5450.2009	−3302.243	−3978.7171	3724.8490
	42	6371.7100	−35.219661	148.981239	5205.3497	−3674.646	−4460.9775	2682.4142
	51	6375.5237	−25.739304	27.685396	5742.9399	−2768.744	5085.4427	2668.2638
	61	6370.0241	40.238919	355.750978	4862.6051	4114.885	4849.2400	−360.2775
	62	6369.9649	40.263212	355.632171	4860.8149	4116.908	4846.6975	−370.1957

[a]Geocentric radius.

[b]Geocentric latitude.

[c]Geocentric longitude.

[d]Distance from the spin axis.

[e]Geocentric Cartesian coordinates with x directed to the prime meridian in the equatorial plane, z perpendicular to that plane, and y completing the right-handed system.

Table 3. Relative station locations

DSS	DSS	Δλ, deg	Δr_s, km	Δλ, deg	Δr_s, km	Δλ, deg	Δr_s, km	Δλ, deg	Δr_s, km
		LS 27		LS 32		LS 33		LS 35	
12	41	106.307028	−238.1490	106.307017	−238.1499	106.307013	−238.1516	106.307021	−238.1499
	42	94.213264	6.7000	94.213270	6.6997	94.213268	6.7016	94.213259	6.7013
	51	215.509127	−530.8916	215.509127	−530.8904	215.509133	−530.8891	215.509118	−530.8893
	61	−112.556450	349.4452	−112.556462	349.4442	−112.556453	349.4448	−112.556453	349.4442
41	42	−12.093764	244.8490	−12.093747	244.8496	−12.093745	244.8531	−12.093762	244.8512
	51	109.202099	−292.7426	109.202111	−292.7405	109.202120	−292.7376	109.202097	−292.7394
	61	−218.863478	587.5942	−218.863479	587.5941	−218.863466	587.5964	−218.863474	587.5942
42	51	121.295863	−537.5916	121.295857	−537.5901	121.295865	−537.5907	121.295858	−537.5906
	61	−206.769714	342.7452	−206.769733	342.7445	−206.769721	342.7432	−206.769713	342.7430
51	61	−328.065577	880.3368	−328.065590	880.3346	−328.06558	880.3339	−328.065571	880.3336

Geodetic survey relative locations

DSS	DSS	Δλ, deg	Δr_s, km	Δz, km
12	11	0.043931	5.7117	−8.1353
12	14	0.084046	8.0547	−11.42364
11	14	0.040114	2.3430	−3.288
61	62	0.118807	1.7902	−2.0232

Table 4. Station location comparisons[a]

DSS	LS 27 − LS 35			LS 32 − LS 35			LS 33 − LS 35		
	Δr_s	Δλ	Δδλ	Δr_s	Δλ	Δδλ	Δr_s	Δλ	Δδλ
11, 12, 14[b]	−2.2	5.9	—	−2.1	8.6	—	−0.1	7.6	—
41	−3.1	5.2	0.7	−2.1	9.0	−0.4	1.6	8.3	−0.8
42	−0.9	5.4	0.5	0.5	7.5	1.1	−0.3	6.7	0.9
51	0.1	4.9	0.9	−1.0	7.6	0.9	−0.2	6.0	1.6
61, 62[b]	−3.1	5.6	0.3	−2.0	9.5	1.0	−0.6	7.5	−0.2
rms[c]	2.2	5.4	0.7	1.7	8.5	0.9	0.8	7.3	1.0

DSS	LS 36 − LS 35		
	Δr_s	Δλ	Δδλ
11	−4.0	1.1	—
12	−4.0	1.1	—
14	−4.6	1.7	—
41	−1.4	−1.1	2.2
42	−1.4	−1.1	2.2
51	−1.8	0.4	0.7
61	−3.0	1.6	−0.5
62	−3.0	1.6	−0.5
rms[c]	3.1	1.3	1.5

[a] Δr_s is given in meters, Δλ and Δδλ are given in units of 10^{-5} degrees ≈ 1 meter, and Δδλ is computed with respect to DSS 12.

[b] DSSs 11, 12, 14, 61, and 62 are not compared separately because their relative locations have been constrained to the same value in all location sets.

[c] The "root mean sum" of squares of the tabulated values.

Table 5. Summary of data used to determine station locations[a]

Flight	No. data points doppler[b]	Doppler count time	Tracking span	Effective data wt, Hz[c]	Sun-earth-probe angle, deg	Declination, deg
Mariner 4 encounter	415 (361)	600 60	1965 7/10–7/21	0.05	77	−3
Mariner 5 cruise	1217 (751)	600	1967 7/28–9/16	0.05	35-20-35	−8 to +8
Mariner 5 encounter	947 (691)	600 60 10	1967 10/14–10/25	0.05	45	6
Mariner 5 postencounter	849 (479)	600	1967 10/28–11/21	0.05	43	+2 to −2
Mariner 6 encounter	620 (595)	600 60	1969 7/26–7/31[d]	0.08	117	−24

[a]all solutions were obtained from SATODP C 1.0 using DE 78 and LE 16.

[b]The first number is without ionosphere correction; the number in parentheses is with ionosphere correction.

[c]The effective data weight is for a 60-s doppler count-time point.

[d]Data stopped at $4^h\ 30^m$ on July 31, 45 min. before encounter.

The resulting station locations differ in two major respects from LS 25:

(1) Smaller average spin-axis corrections. In LS 25, ionosphere effects caused nearly a 4-m change in the Goldstone spin-axis solutions as opposed to the current value of ~2.75 m. This may be due to the no-extrapolation policy used in preparing the coefficients.

(2) Larger longitude corrections for Mariners 4 and 5. In LS 25, the ionosphere changed longitude estimates for Mariner 4 by 2.0 m and for Mariner 5 by −0.7 m at Goldstone. In LS 35, the change was 3.3 m for Mariner 4 and −5.5 m for Mariner 5. These ionospheric corrections played a significant role in increasing the spread between the Mariners 4 and 5 longitudes, but they also decreased the differences between Mariners 5 and 6 so that they agree to within 1.80 m. Values of the estimated station locations with and without the ionosphere calibrations appear in Tables 8 and 9, and the differences are presented graphically in Figs. 1, 2, and 8. The relative longitudes appear in Table 10. The longitude corrections vary significantly from mission to mission, whereas the spin-axis changes are somewhat systematic.

E. Formation of LS 35

LS 35 was derived by combining the ionosphere correction locations and their associated information matrices exactly as in LS 25. The relative locations at the Goldstone and Madrid complexes were constrained to the survey values shown in Table 9. Station z heights (i.e., the distance off the equatorial plane) are identical with those in LS 25, which came from Ref. 9. A complete listing of LS 35 appears in Table 11.

The solutions were combined using a program written by Mottinger. The program uses the techniques applied in the combined Ranger Block III physical constant and station location estimates (Ref. 2). These techniques were modified to deweight longitude information by introducing a constant uncertainty into the diagonal longitude terms in the covariance matrix.

Figures 3 through 7 show the spin-axis estimates used in LS 35, Figs. 8 through 12 show the absolute longitudes, and Figs. 13 through 16 show the relative longitudes. When examining Figs. 8 through 12, recall that one does not expect to obtain absolute longitude information other than from encounter cases, where there is a strong right ascension tie to the planet.

Table 6. Flight data summary SATODP lockfile input for timing and polar motion

Mission	Parameter[a]	Source	Calendar epoch (YYMMDD)	Seconds past 0[h], Jan. 1, 1950	Value[b,c]	Slope[c,d]
Mariner 4 encounter	A.1−UTC	BIH	650701	489024000.0	4.009248	150.E-10
	A.1 − UT1		650701	489024000.0	3.996946	202.7176E-10
		BIH	650801	491702400.0	4.046700	173.1515E-10
	Pole X		650701	489024000.0	−0.042	0.38559E-7
	Y		650701	489024000.0	0.4665	0.25172E-8
	X		651001	496972800.0	0.20433	0.91823E-8
	Pole Y	BIH	651001	496972800.0	0.28509	−0.34345E-7
Mariner 5 cruise and postencounter	A.1−UTC	USNO	660101	504921600.0	4.347712	300.E-10
	A.1−UT1		670701	552096000.0	5.714719	171.0324E-10
			670801	554774400.0	5.769218	215.5933E-10
			670901	557452800.0	5.8312	255.5094E-10
			671001	560044800.0	5.9018	285.9659E-10
			671101	562723200.0	5.982073	334.0150E-10
			671201	565315200.0	6.068862	273.8624E-10
	Pole X	BIH	670701	552096000.0	−0.01614	0.38867E-8
	Y		670701	552096000.0	0.21655	0.19198E-8
	X		671001	560044800.0	−0.008	−0.29045E-8
	Y		671001	560044800.0	0.204	0.24944E-8
	X		680101	567993600.0	−0.00044	0.13657E-7
	Pole Y	BIH	680101	567993600.0	0.27147	0.88316E-8
Mariner 5 encounter	A.1−UTC	BIH	660101	504921600.0	4.347712	300.E-10
	A.1−UT1		671001	560044800.0	5.900406	285.9659E-10
			671101	562723200.0	5.981260	334.0150E-10
	Pole X	BIH	671001	560044800.0	−0.008	−0.29045E-8
	Y		671001	560044800.0	0.206	0.24944E-8
	X		680101	567993600.0	−0.00044	0.13657E-7
	Pole Y	BIH	671001	567993600.0	0.27147	0.88316E-8
Mariner 6 encounter	A.1−UTC	BIH	681005	592012800.0	6.860448	300.E-10
	A.1−UT1		690705	615600000.0	7.565476	236.7619E-10
			690805	618278400.0	7.625141	225.9890E-10
	Pole X	BIH	690705	615600000.0	0.11908	0.74605E-8
	Y		690705	615600000.0	0.29119	−0.24042E-7
	X		691005	623548800.0	0.07098	−0.20425E-7
	Pole Y	BIH	691005	623548800.0	0.09840	

[a]X and Y are Cartesian coordinates of the pole; +X along Greenwich meridian, +Y along 90° west meridian.

[b]UTC and UT1 values are in seconds; pole position value is in arcseconds.

[c]Values entered are coefficients for Hermite polynomials.

[d]UTC and UT1 slopes are unitless; polar motion is in arcseconds per second.

Table 7. Effects of different troposphere models on Mariner 4

Troposphere model combination[a]	Δλ 11 (m)	Δr_s 11 (m)	Δλ 42 (m)	Δr_s 42 (m)	Δλ 51 (m)	Δr_s 51 (m)
Cain 1 − Chao	0.0	1.2	0.1	−0.2	0.1	0.4

[a]15-deg minimum elevation angle constraint.

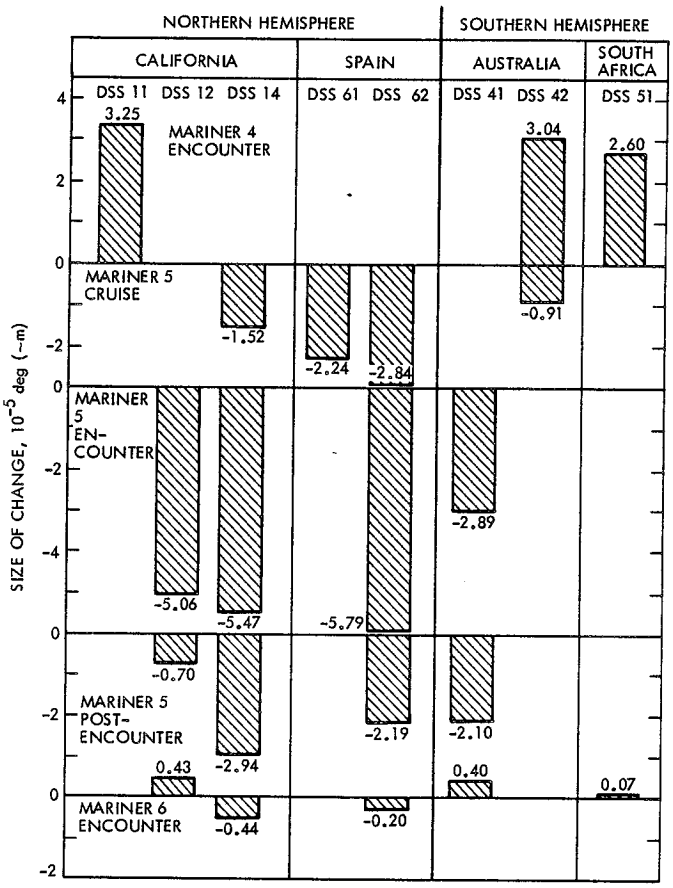

Fig. 1. Changes in longitude estimates due to ionospheric corrections

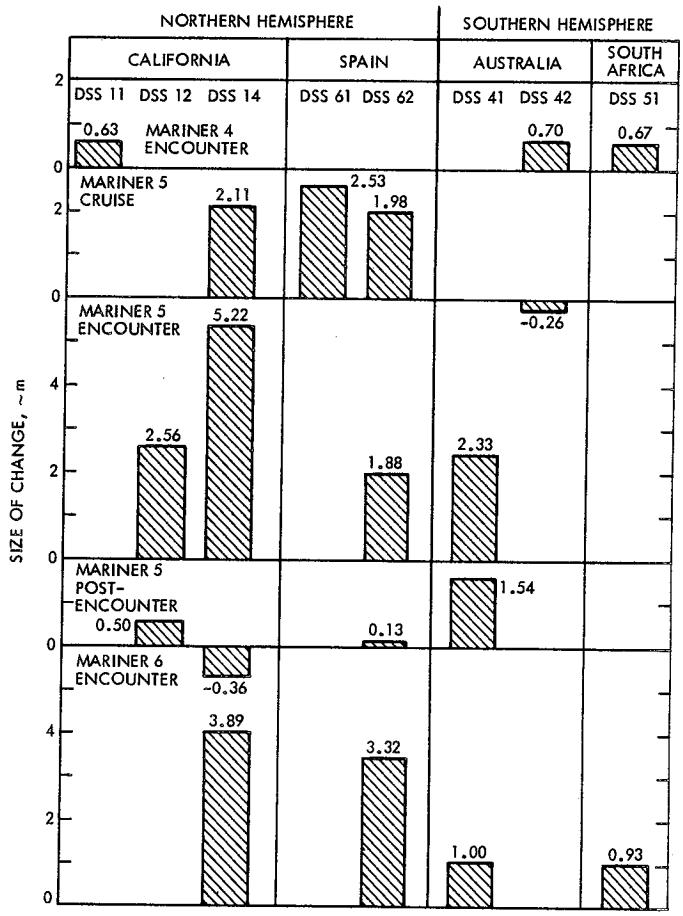

Fig. 2. Changes in spin axis estimates due to ionospheric corrections

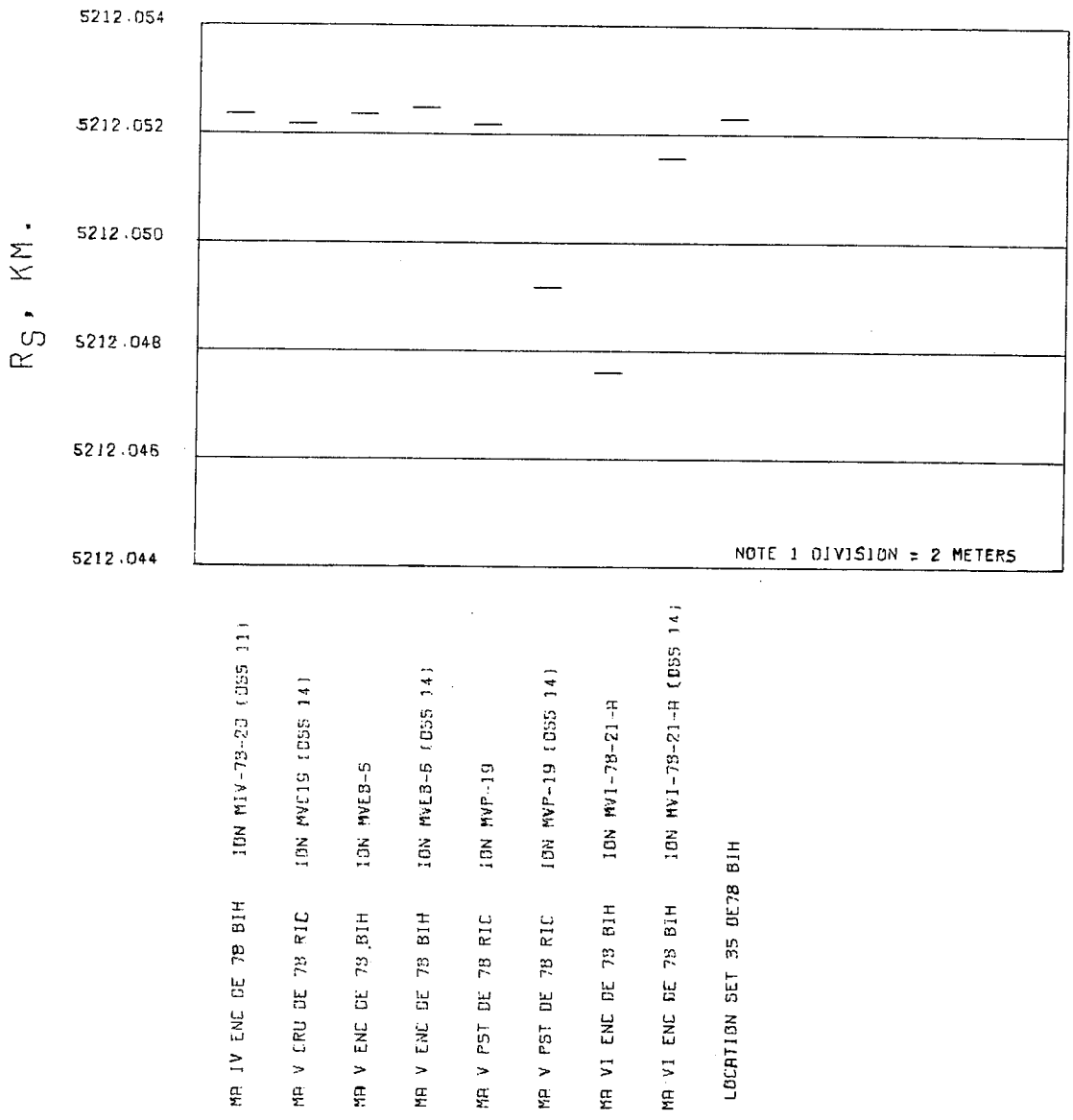

Fig. 3. Spin-axis estimates (1903.0 pole), DSS 12

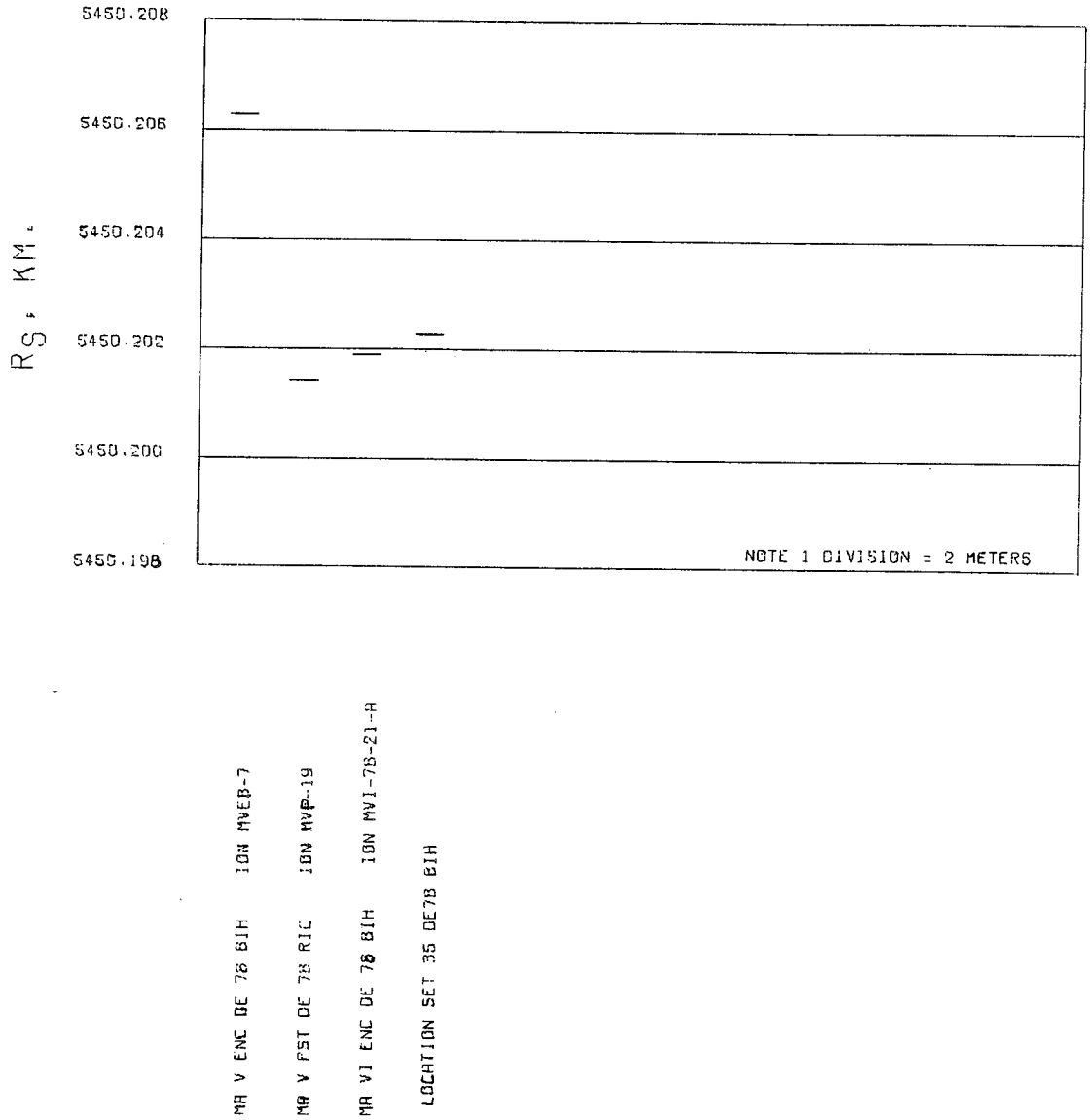

Fig. 4. Spin-axis estimates (1903.0 pole), DSS 41

Table 8. Absolute station locations with ionosphere calibrations

DSS	Data source	Distance off spin axis r_s, km[a]	Geocentric longitude λ, deg[b]	Distance from equator plane z, km[c]	Run identification[d,e]
12		5212.0xx x	243.194xx x	3673.763	
	Mariner 4 encounter	52.4	67.2		M IV–78–20 (DSS 11)
	Mariner 5 cruise	52.2	55.9		M V C 19 (DSS 14)
	Mariner 5 encounter	52.4	50.8		M V E 8–7
		52.5	50.6		M V E 8–7 (DSS 14)
	Mariner 5 postencounter	52.2	60.5		M V P–19
		49.2	59.2		M V P–19 (DSS 14)
	Mariner 6 encounter	47.6	52.3		M VI–78–21–A
		51.6	52.1		M VI–78–21–A (DSS 14)
	LS 35	52.4	50.9	3673.763	
41		5450.20x x	136.887xx x	−3302.243	
	Mariner 5 encounter	6.3	49.9		M V E 8–7
	Mariner 5 postencounter	1.4	58.5		M V P 19
	Mariner 6 encounter	1.9	48.0		M VI –78–21A
	LS 35	2.3	8.8	−3302.243	
42		5205.35x x	148.981xx x	−3674.646	
	Mariner 4 encounter	1.0	39.0		M IV–78–20
	Mariner 5 cruise	0.9	30.2		M V C–19
	LS 35	1.1	25.0	−3674.646	
51		5742.94x x	27.685xx x	−2768.744	
	Mariner 4 encounter	2.1	52.1		M IV–78–20
	Mariner 6 encounter	0.9	39.6		M VI–78–21A
	LS 35	1.7	39.2	−2768.744	
61		4862.60x x	355.75xxx x	4114.885	
	Mariner 5 cruise	8.5	100.3		M V C–19
		8.6	099.2		M V C–19 (DSS 62)
	Mariner 5 encounter	7.2	096.4		M V E 8–7 (DSS 62)
	Mariner 5 postencounter	7.1	106.4		M V P–19 (DSS 62)
	Mariner 6 encounter	8.4	097.3		M VI–78–21A
	LS 35	8.1	096.2	4114.885	

[a]The minor part is tabulated in meters.

[b]The minor part may be assumed to be tabulated in meters since the equivalent of 10^{-5} deg at DSSs 11, 12, and 14 is 0.91 m, at DSSs 61 and 62 is 0.85 m, at DSS 51 is 1.00 m, at DSS 41 is 0.95 m, and at DSS 42 is 0.91 m.

[c]Not estimated; included for completeness.

[d]Relative locations used at Goldstone and Madrid are given in Table 3.

[e]The result was transferred from the station in parentheses using survey deltas.

Table 9. Absolute station location solutions without ionosphere calibration[a]

DSS	Data source	Distance off spin axis r_s, km[a]	Geocentric longitude λ, deg [b]	Distance from equator plane z, km[c]	Run identification[d,e]
12		5212.0xx x	243.194xx x	3673.763	
	Mariner 4 encounter	51.6	64.5	↑	M IV 78–19 (DSS 11)
	Mariner 5 cruise	51.0	56.7		M V C–18 (DSS 11)
	Mariner 5 cruise	50.0	57.4		M V C–18 (DSS 14)
	Mariner 5 encounter	49.9	55.7		M V E 8–5
		47.2	56.1		M V E 8–5 (DSS 14)
	Mariner 5 postencounter	51.7	61.3		M V P 18
		49.6	62.0		M V P 18 (DSS 14)
	Mariner 6 encounter	48.3	51.9		M VI–8–20A
		47.7	52.5	3673.763 ↓	M VI–8–20A (DSS 14)
41		5450.xxx x	136.887xx x	−3302.243	
	Mariner 5 cruise	199.9	60.6	↕	M V C 18
	Mariner 5 encounter	200.5	52.9		M V E 8–5
	Mariner 6 encounter	200.9	47.6	−3302.243 ↓	M VI–8–20A
42		5205.35x x	148.981xx x	−3674.646	
	Mariner 4 encounter	0.3	36.3	−3674.646	M IV 78–19
	Mariner 5 cruise	1.2	31.2	−3674.646	M V C 18
51		5742.9xx x	27.685xx x	−2768.744	
	Mariner 4 encounter	41.6	51.0	−2768.744	M IV 78–19
	Mariner 6 encounter	39.9	39.5	−2768.744	M VI–8–20A
61		4862.60x x	355.75xxx x	4114.885	
	Mariner 5 cruise	6.0	102.6	↑	M V C 18
	Mariner 5 cruise	6.6	102.2		M V C 18 (DSS 62)
	Mariner 5 encounter	5.0	101.9		M V E 8–5 (DSS 62)
	Mariner 5 postencounter	7.0	108.7		M V P–18 (DSS 62)
	Mariner 6 encounter	5.1	097.7	4114.885 ↓	M VI–8–20A (DSS 62)

[a,b,c,d,e]See footnotes a, b, c, d, and e, respectively, Table 8.

Table 10. Relative longitude solutions

Data source run identification	Goldstone DSS 12 minus[a]			
	DSS 41	DSS 42	DSS 51	DSS 61
	Without ionosphere calibration			
M IV 78–19	106.3070x.x	94.2132x.x	215.5091x.x	−112.5564x.x
M V Cruise–18		8.2	3.6	
M V Encounter 8–5	2.9	5.5		6.0
M V P–18	0.6			6.3[b]
M VI–8–20A	4.2			7.5[b]
			2.4	5.8
	With ionosphere calibration			
M IV–78–20	106.3070x.x	94.2132x.x	215.5091x.x	−112.5564x.x
M V C–19		8.2	5.2	
M VE 8–7	0.9	5.6		4.6[b]
M V P–19	2.0			5.6[b]
M VI–78–21	4.3			6.0[b]
LS35	2.1		1.3	5.2[b]
		5.9	1.8	5.3

[a]See footnote b, Table 8.

[b]Survey deltas were used to transfer solution from another station at this complex.

Table 11. Location Set 35 using DE 78, BIH UT1, and pole; ionosphere corrections

DSS	R, km[a]	ϕ, deg[b]	λ, deg[c]	r_s, km[d]	z, km[e]	x, km[e]	y, km[e]
11	6372.0106	35.208035	243.150578	5206.3408	3673.763	−2351.4298	−4645.0794
12	6371.9949	35.118658	243.194509	5212.0524	3665.628	−2350.4432	−4651.9788
14	6371.9937	35.244346	243.110463	5203.9977	3677.052	−2353.6216	−4641.3422
41	6372.5595	−31.211406	136.887488	5450.2023	−3302.243	−3978.7188	3724.8492
42	6371.7112	−35.219654	148.981250	5205.3511	−3674.646	−4460.9792	2682.4140
51	6375.5253	−25.739297	27.685392	5742.9417	−2768.744	5085.4445	2668.2642
61	6370.0264	40.238902	355.750962	4862.6081	4114.885	4849.2429	−360.2790
62	6369.9672	40.263194	355.632155	4860.8179	4116.908	4846.7004	−370.1972

[a,b,c,d,e]See footnotes a, b, c, d, and e, respectively, Table 2.

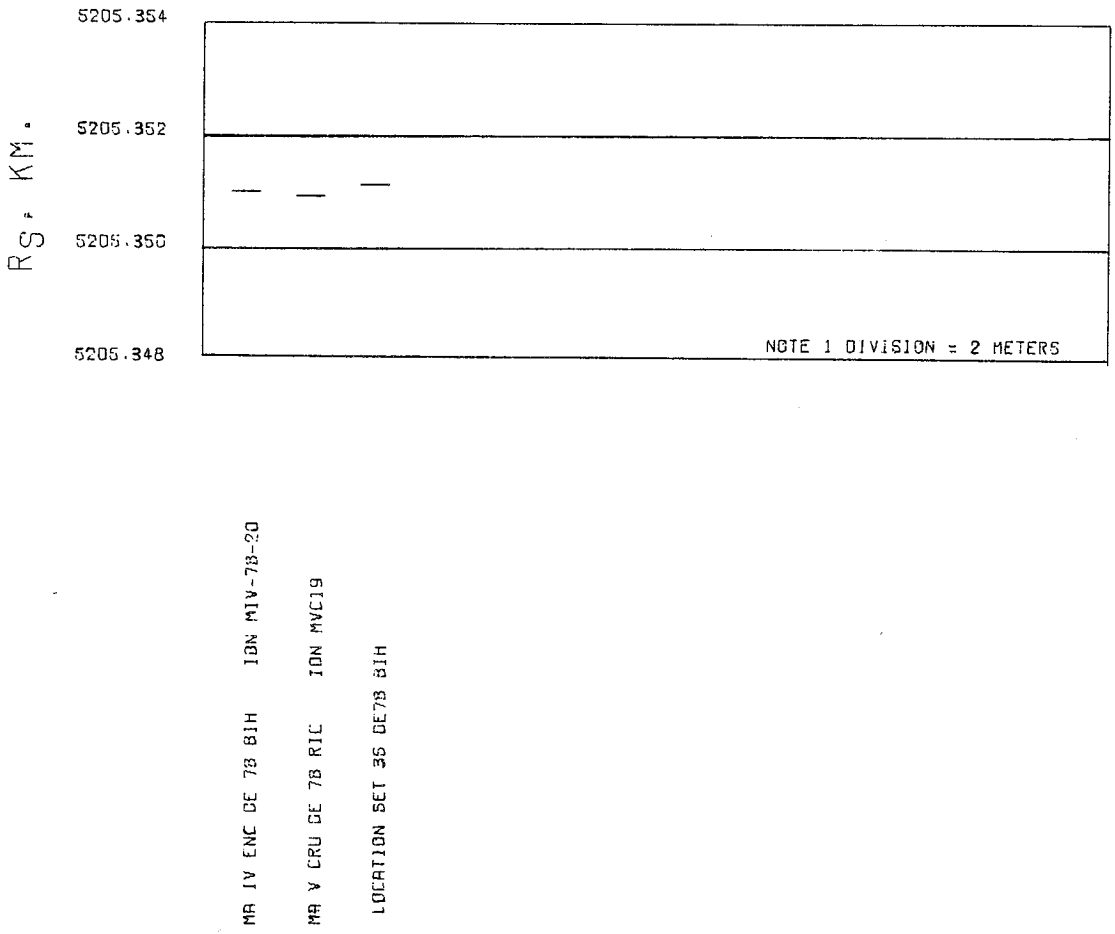

Fig. 5. Spin-axis estimates (1903.0 pole), DSS 42

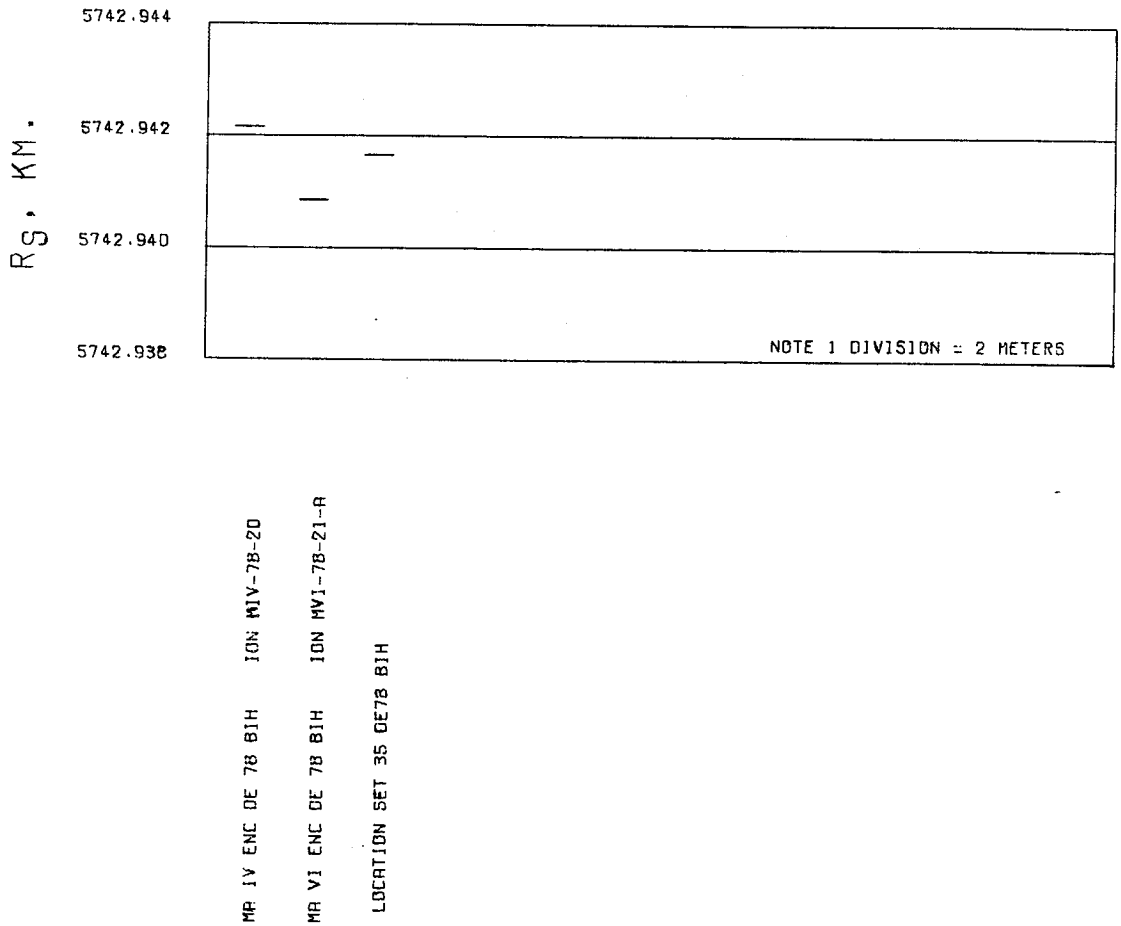

Fig. 6. Spin-axis estimates (1903.0 pole), DSS 51

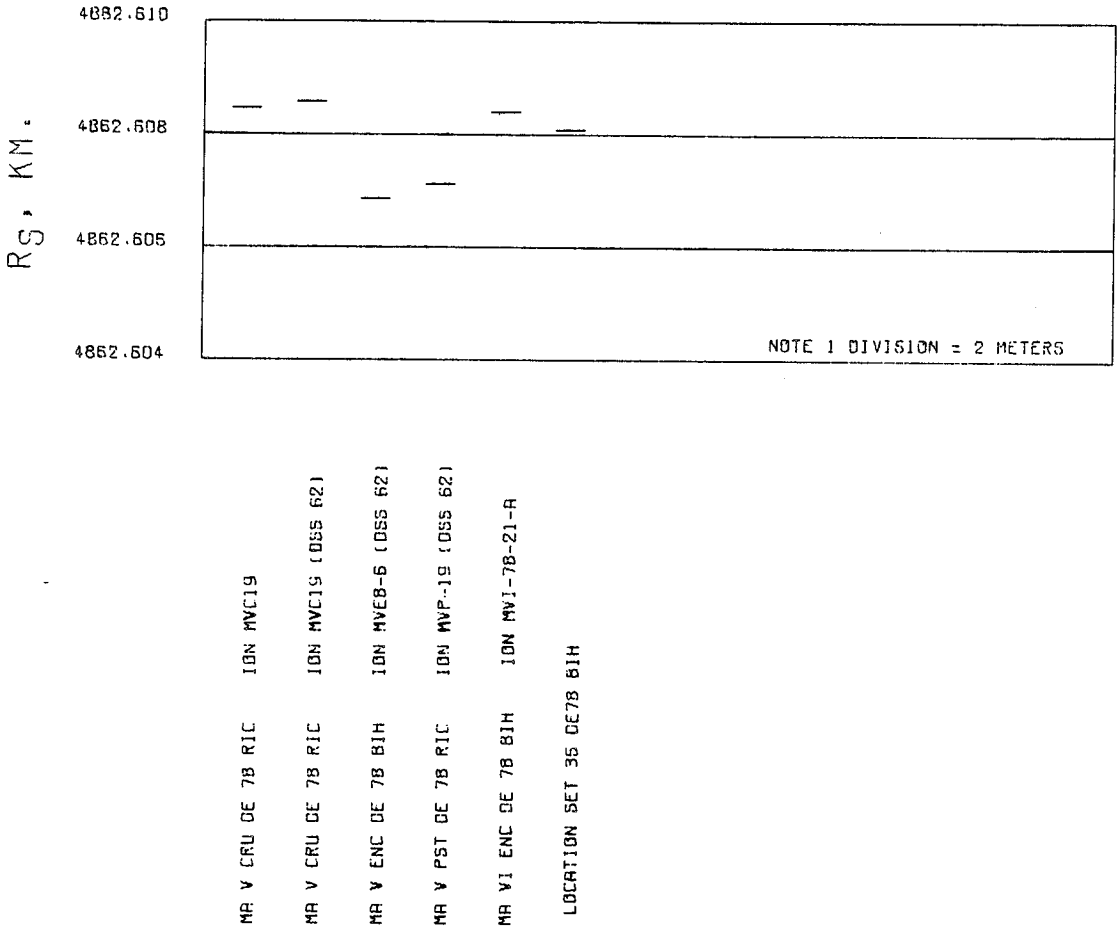

Fig. 7. Spin-axis estimates (1903.0 pole), DSS 61

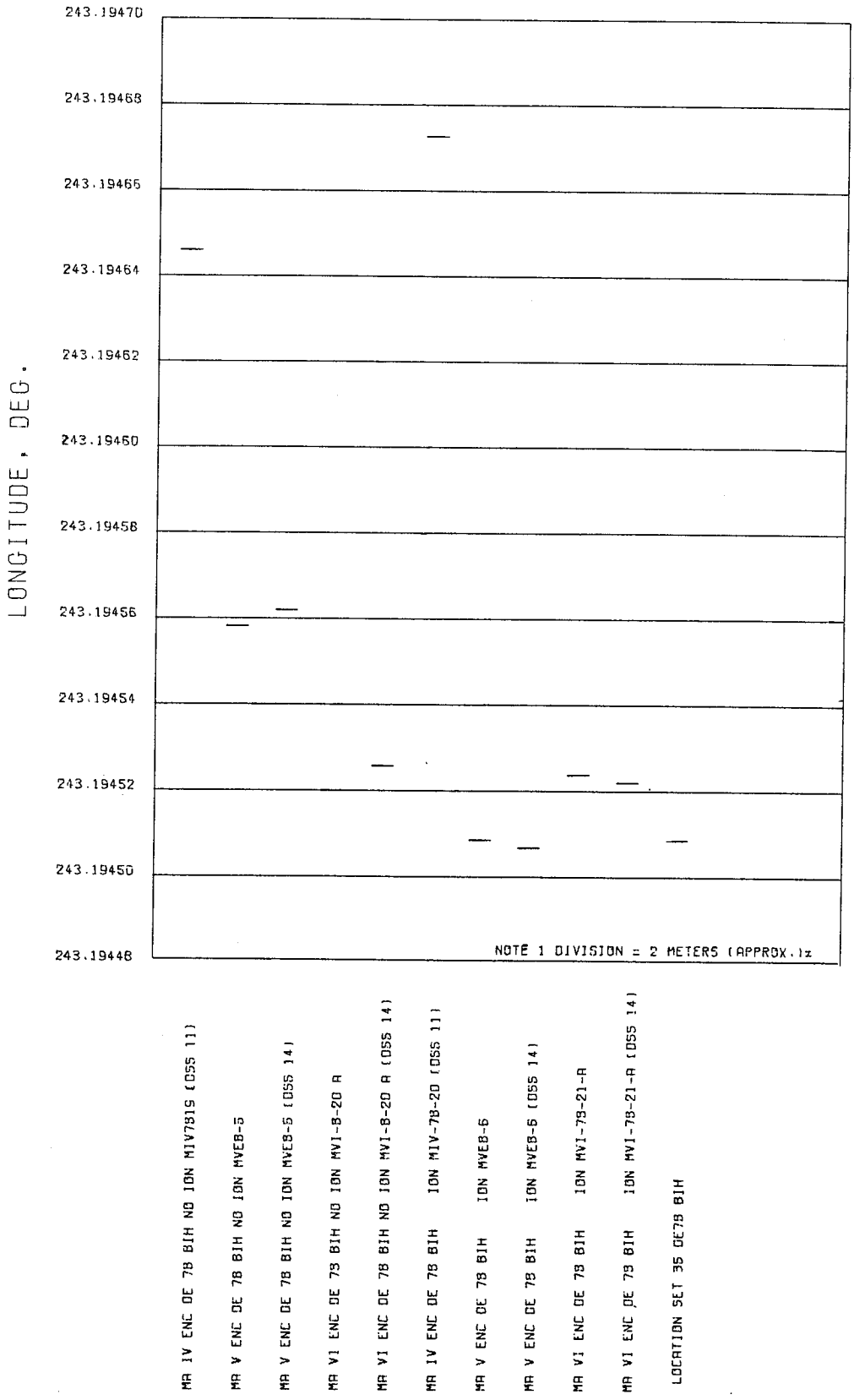

Fig. 8. Longitude estimates (1903.0 pole), DSS 12

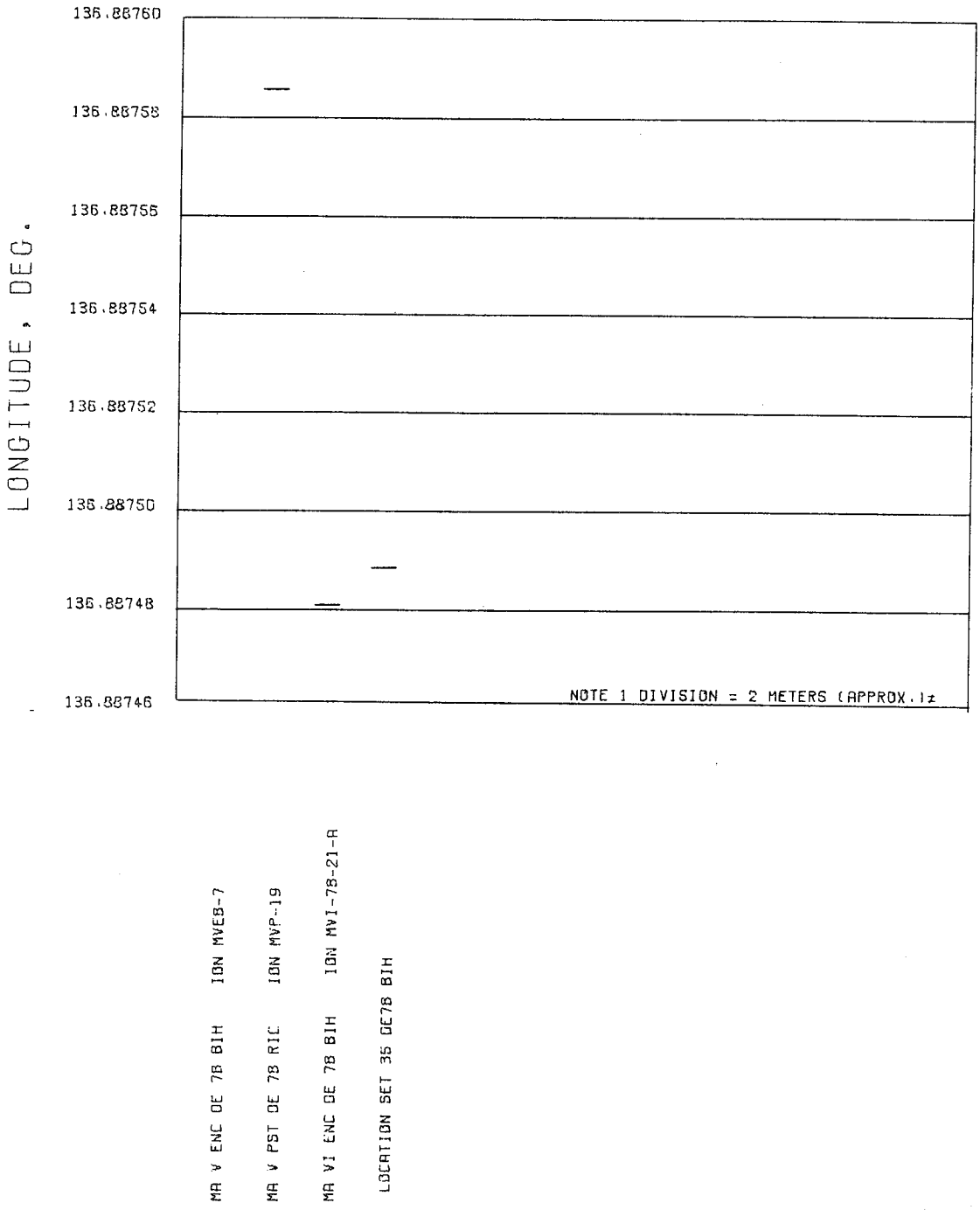

Fig. 9. Longitude estimates (1903.0 pole), DSS 41

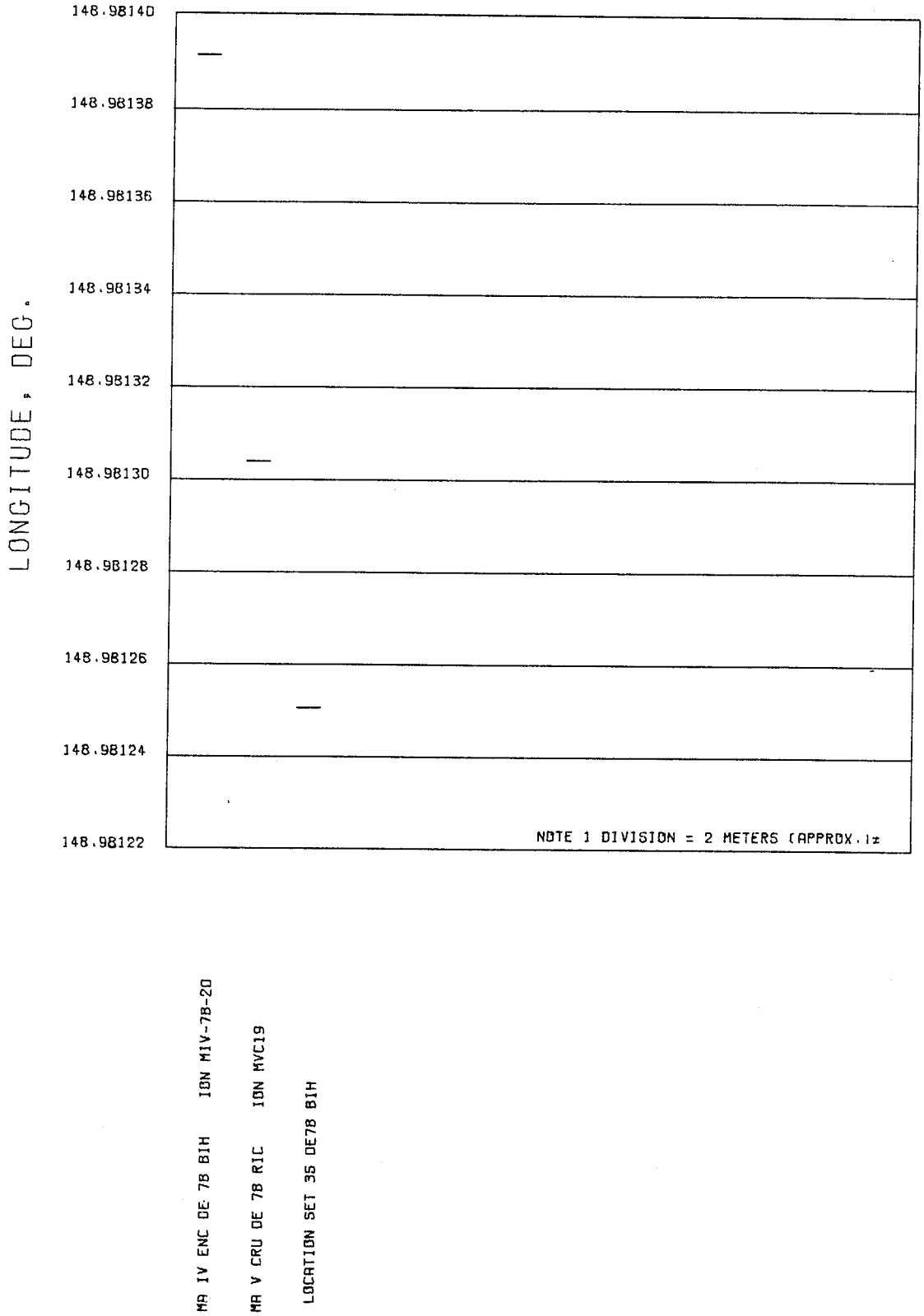

Fig. 10. Longitude estimates (1903.0 pole), DSS 42

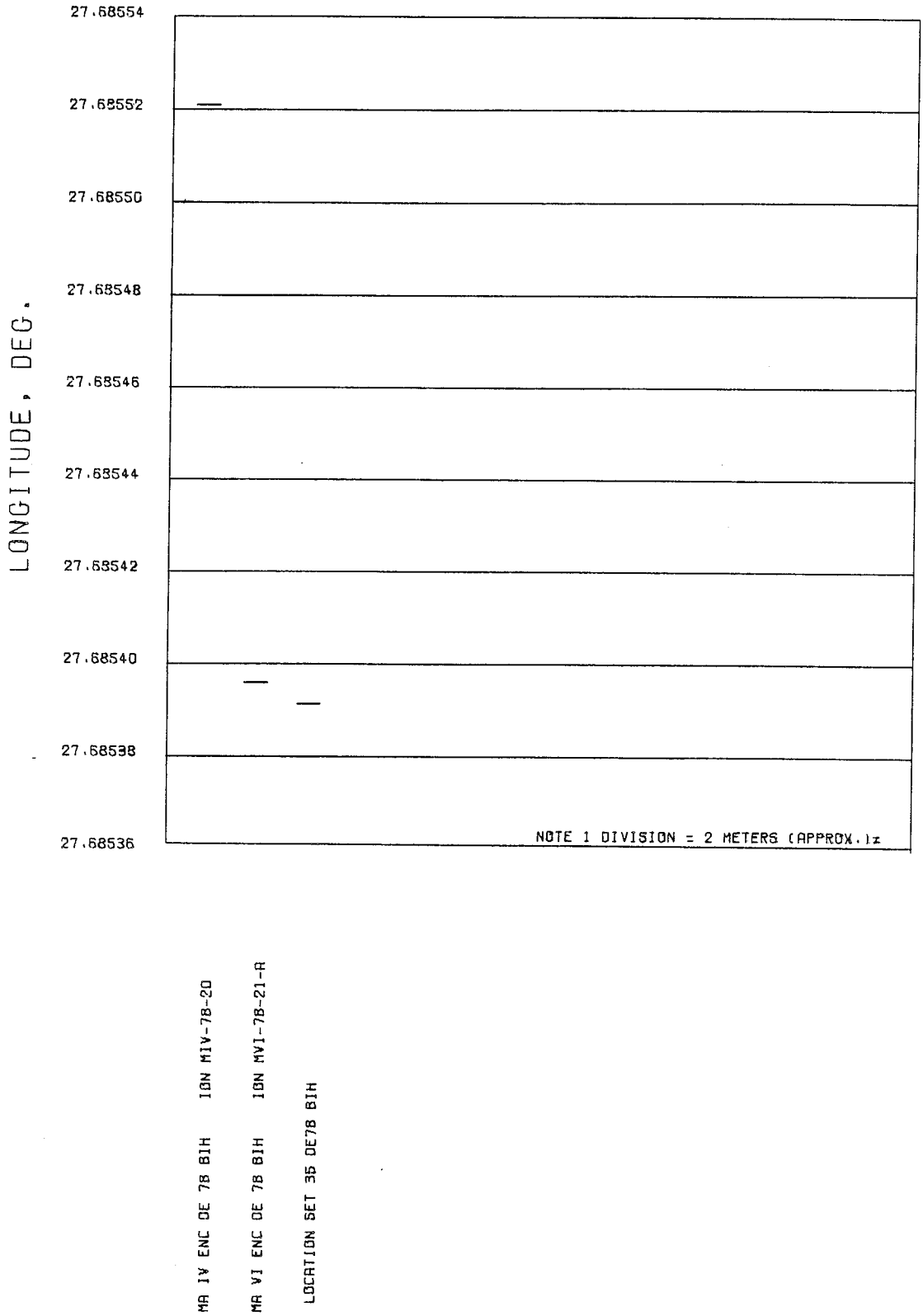

Fig. 11. Longitude estimates (1903.0 pole), DSS 51

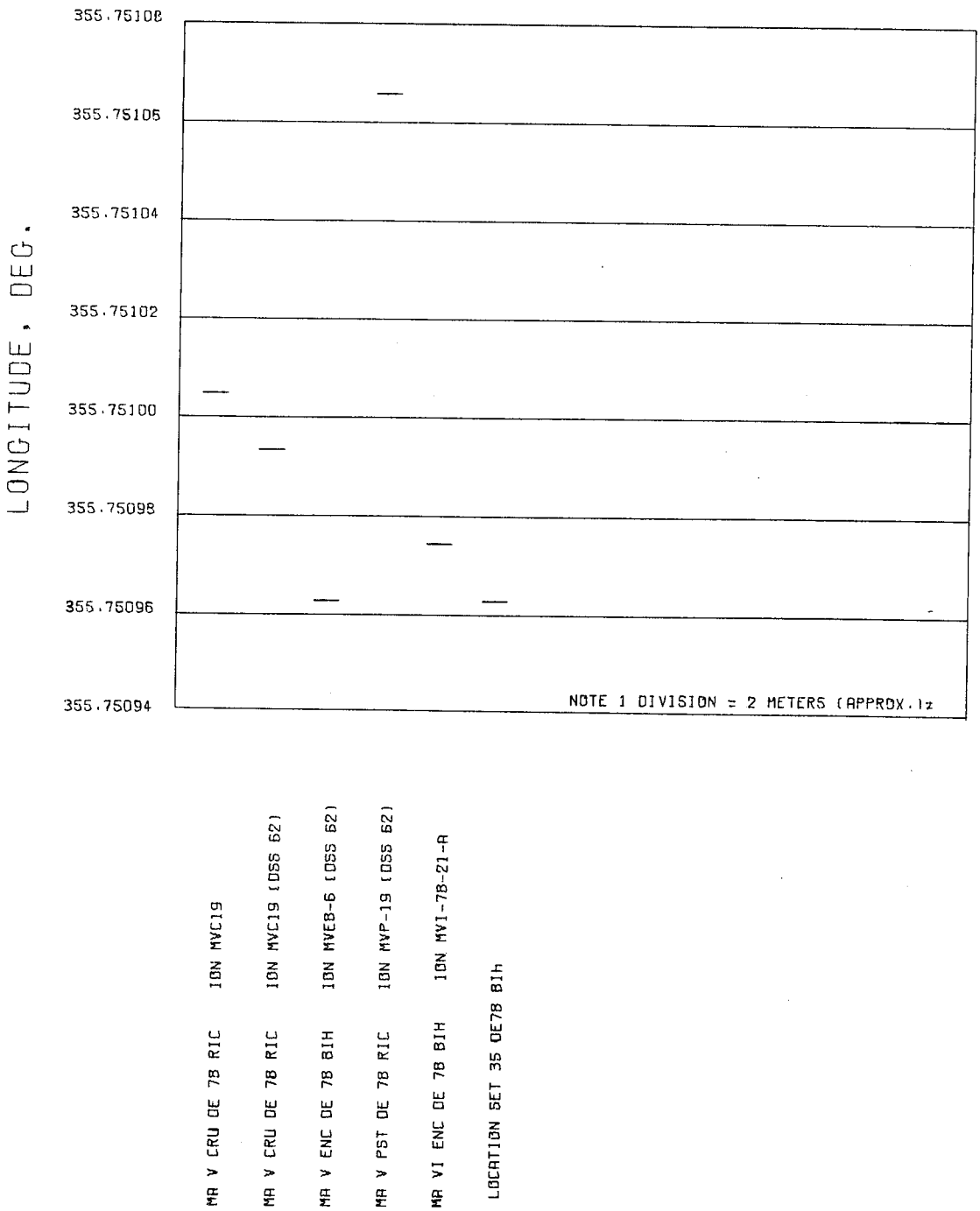

Fig. 12. Longitude estimates (1903.0 pole), DSS 61

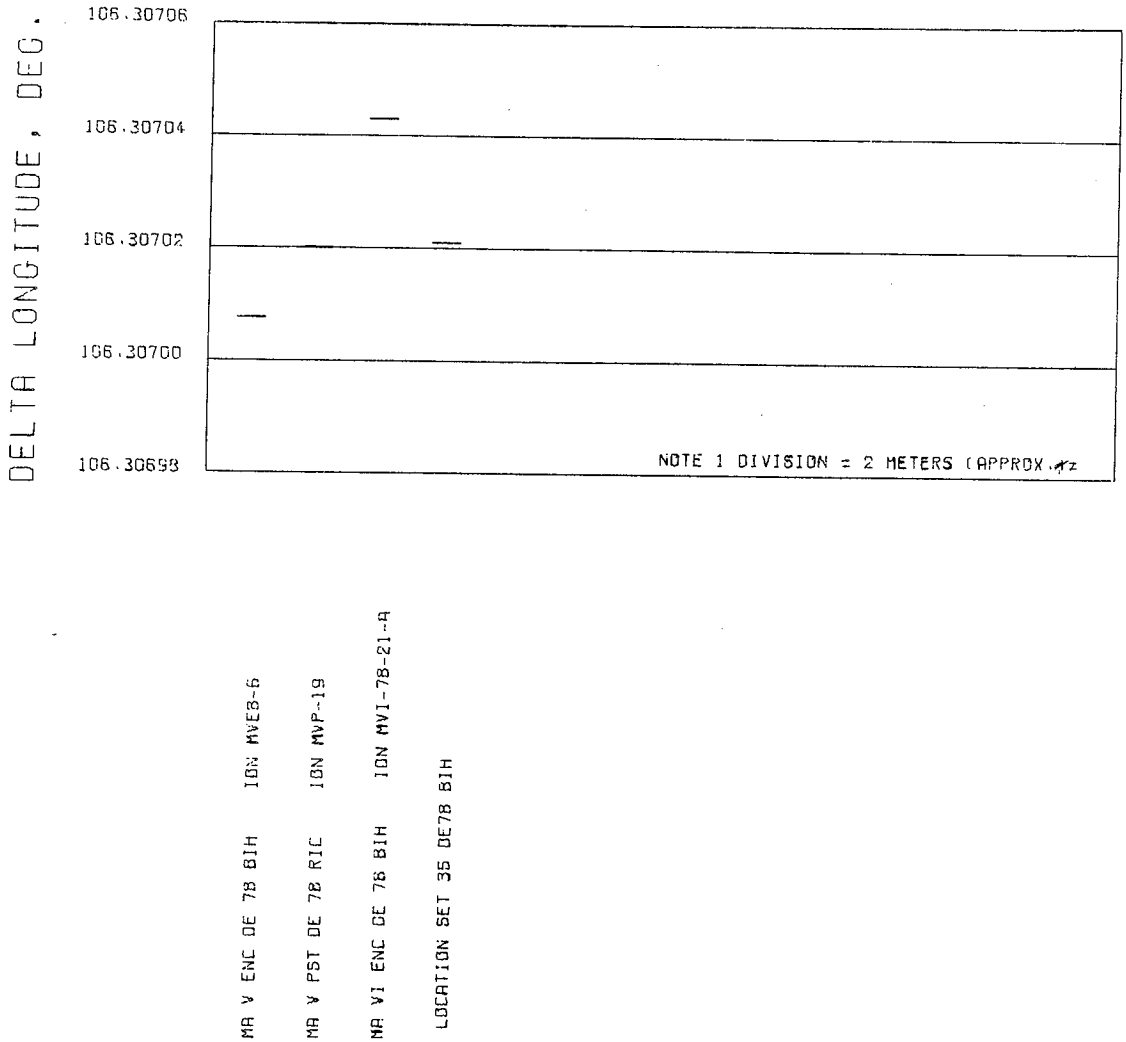

Fig. 13. Relative longitudes (1903.0 pole), DSS 12 – DSS 41

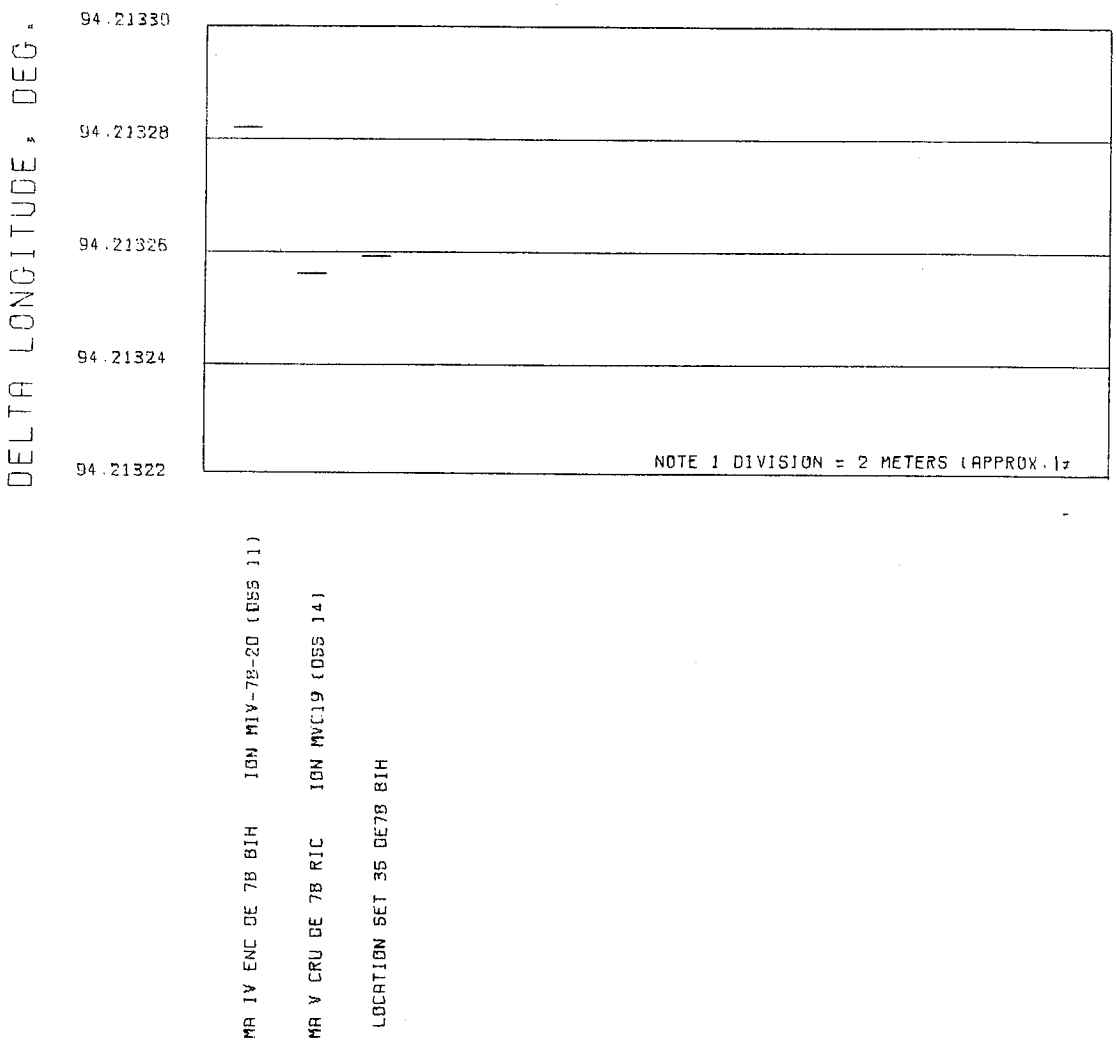

Fig. 14. Relative longitudes (1903.0 pole), DSS 12–DSS 42

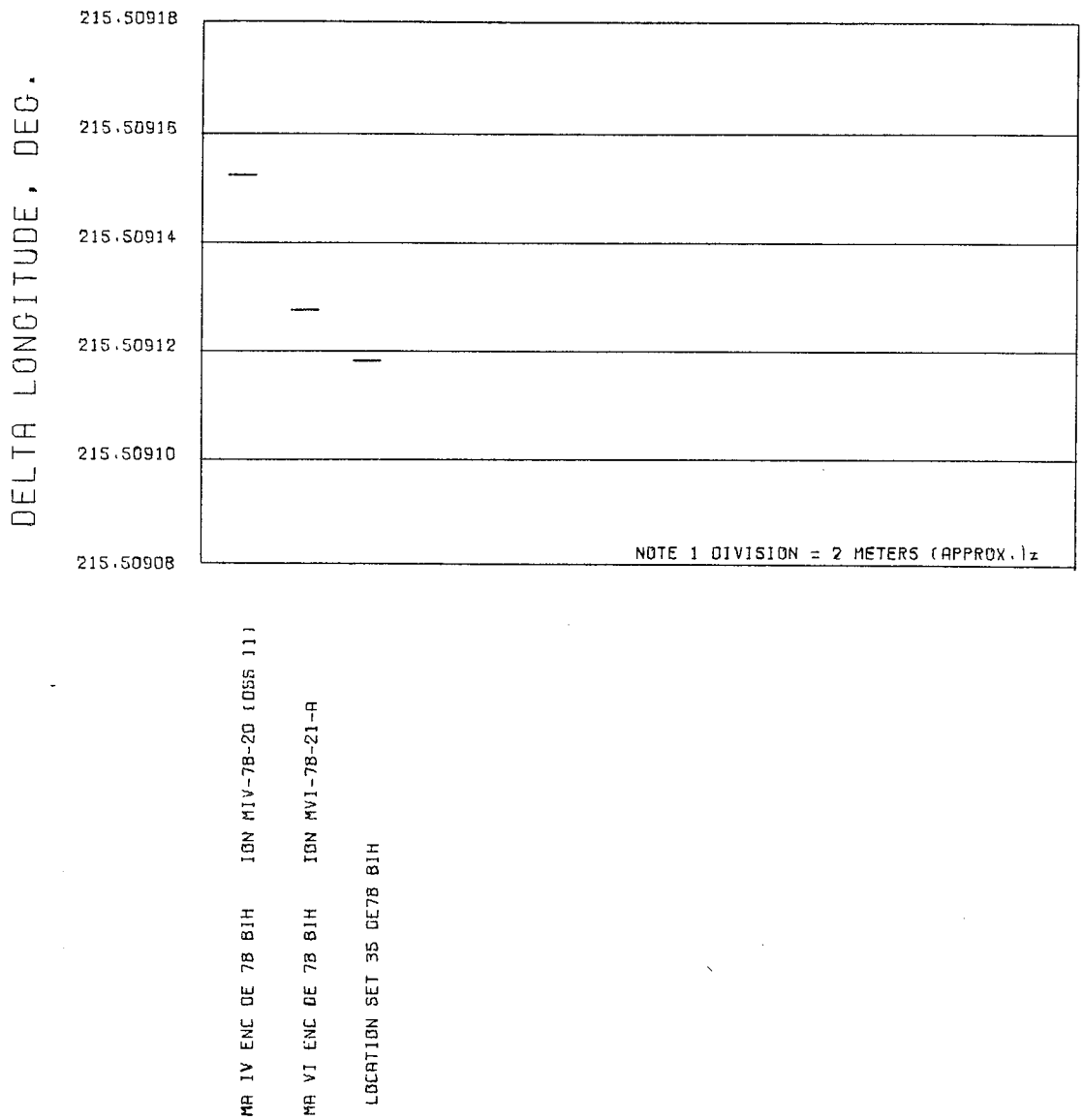

Fig. 15. Relative longitudes (1903.0 pole), DSS 12−DSS 51

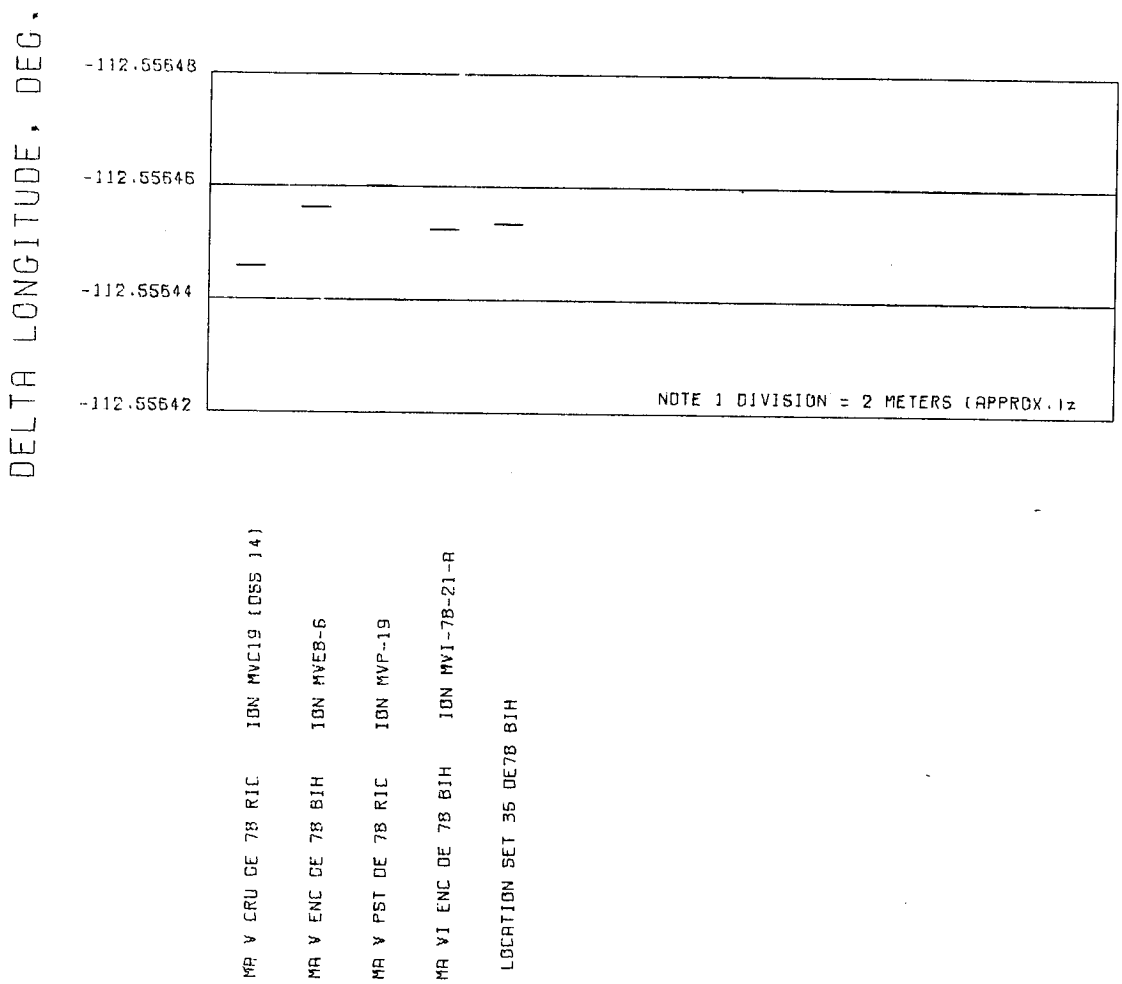

Fig. 16. Relative longitudes (1903.0 pole), DSS 12–DSS 61

F. Discussion of Results

Solutions are shown only for DSSs 12, 41, 42, 51, and 61. In actuality, there were tracking data solutions for eight DSN stations, but to simplify comparison these have been referred to one station at each complex by using the geodetic surveys between the antennas. The run identification (ID) indicates such a reference by giving the actual solved-for station in parentheses.

From Figs. 3 through 16, one can see that except for the Mariner 5 encounter solution for DSS 41 (which is presumably a result of the paucity of data mentioned earlier), the agreement in spin-axis solutions ranges from 0.05 m at DSS 42 to 1.75 m at DSS 61. For relative longitudes, the agreement is under 3.5 m. If one ignores Mariner 4 encounter data, the other two absolute longitudes agree to within 2.0 m. Formal statistics in the combination itself range from 1.0 to 2.6 m in r_s and from 3.8 to 4.3 m in longitude.

Based upon the scatter, the formal statistics, and the initial estimates obtained from Mariner 9, the true uncertainty is believed to range from 1.5 to 2 m in r_s and 3 to 4 m in longitude.

There is a known error in DE 78 that affected the derived station locations. Mars radar bounce data taken during the 1971 opposition were erroneously time-tagged due to an on-site operations problem. The data were correct, but of course the incorrect time tag resulted in fallacious ephemeris corrections when processed by the Solar System Data Processing System (SSDPS) (Ref. 10). Correcting this error resulted in the production of DE 79. Comparison with DE 78 indicates that the Mariner 5 longitude estimate will move within tenths of meters of the Mariner 6 estimate, but the Mariner 4 longitudes will not be significantly changed.

A certain amount of engineering judgment was used in producing LS 35. The spin-axis solutions at Goldstone show a large scatter even after ionosphere calibrations are applied. Some data packages show high consistency between the solutions obtained directly from DSS 12 and via the survey from DSS 14 when both stations were tracking during the interval (see Fig. 3). The Mariner 5 encounter results, for example, agree to 0.1 m. The Mariner 5 post-encounter results are not this consistent, perhaps due to extremely limited amounts of ionosphere data for certain DSS 14 passes. Moreover, there was extremely high space plasma activity during this period, which could have varied enough in a short interval to prevent both stations from seeing similar charged particle effects. For these reasons, the Mariner 5 post-encounter spin-axis solutions were given special treatment. The aberrant spin axes were constrained, using survey data, to the spin-axis value obtained from the Goldstone station whose value was more consistent with the other missions, and then combined. A similar procedure was followed for the Mariner 6 encounter where the DSS 12 spin axis was 3 m different from the equivalent one derived from DSS 14. These anomalies are under continuing study, and the combination procedures used here will be discussed later.

The Mariner 4 absolute longitudes were 16 m east of the combined estimate based on Mariners 5 and 6 encounter data. This discrepancy was studied in minute detail because the individual solutions comprising LS 25 were not so disparate. By having the SATODP reproduce the models that produced the Mariner 4 solution used in LS 25, it was possible to obtain better than 1-m agreement with those results, indicating that the difference between LS 25 and LS 35 was due to the changed models. Table 12 shows the individual model effects. Since the old models were known to be less accurate than the newer ones, one had no choice but to accept the new solutions. Here again, it was arbitrarily decided to deweight the absolute longitude information from Mariner 4, retaining the spin-axis information and the correlations that gave relative longitudes.

Based on previous experience, studies are underway to develop procedures that will allow a more thorough statistical analysis of the station location problem. The first step is generation of more realistic covariances for the individual solutions by rigorously "considering" those parameters whose errors are known to affect the solution. These could then be combined using the existing combination program. The second step is to form a combined estimate using all the data and with simultaneous "consideration" of all solution-affecting parameters. This would allow computation of the correlations between ephemerides of the planets and station locations.

G. Mariner 9 Preliminary Solution

The validity of the strategy chosen in LS 35 can be tested by solutions using Mariner 9 encounter and orbital data. To date, only limited success has been obtained in processing orbital data for station location estimates. The best indication, because of the insufficiently known Martian gravitation harmonics, comes from an approach phase run made a few days after Mars Orbit Insertion.

Table 12. Effect of model changes on station location solutions

Model changes	Δλ, m[a]	
	Mariner 4	Mariner 5
BIH vs Richmond UT1[b]	4.7	2.0
Chao vs Cain 1 troposphere	0.1	Not available
DE 78 vs DE 69	0.9	0.0
Total ionosphere calibration correction	3.3	−5.5
Improved polar motion	0.5	Not available
Improved Mars pole direction[c]	0.8	Not applicable
Corrected L/S band weighting	0.8	Not applicable
Total	11.3	−3.5

[a]Obtained using Orbit Determination Programs SATODP C 1.0 and DPODP 5.0.

[b]This also includes a 0.5-m change due to a readjustment in A1-UTC.

[c]Affects orientation of Mars' gravity field.

Table 13. Station location comparisons: Mariner 9 preliminary (no ionosphere calibrations) minus LS 35

DSN	Δr_s, m	Δλ, m	Δδλ, m
12	−3.0	−1.7	
14	−3.7	0.3	−2.0
41	1.8	−3.2	1.6
61	−0.8	−0.9	−0.7
rms	2.6	1.9	1.5

This solution is compared with LS 35 in Table 13. The Mariner 9 solution did not include ionosphere effects. A preliminary estimate of these effects based on seasonal ionospheric information suggests a 4-m increase for northern hemisphere r_s solutions and a 2-m increase for all longitude solutions. The resulting rms of the differences between Mariner 9 and LS 35 are 1.9 and 1.4 m for r_s and longitude respectively.

The solution made at this time was chosen for initial comparison since it was made under conditions analogous to the real-time mission environment; that is, no postflight information was available for updating UT1 and polar motion or the Martian ephemeris. Comparisons will certainly be made later when these final data are available.

IV. Summary

The station locations provided for Mariner 9 encounter are based on solutions that show excellent consistency in spin axis and relative longitude. The solutions that make up LS 35 all involve ionosphere calibrations, and display at each DSS site a scatter that ranges from 0.05 to 1.75 m in distance off the spin axis and from 0.25 to 1.75 m in relative longitude.

Although previous analysis using the Single Precision Orbit Determination Program (SPODP) and the DPODP for Mariner Mars 1969 project support had produced consistent absolute longitudes for Mariners 4 and 5, the latest analysis has terminated with the Mariner 4 absolute longitudes lying some 16 m from the Mariners 5 and 6 solutions. These latter two agree to within 0.75 m. A concerted effort is being made to explain this discrepancy.

V. Acknowledgments

The authors express sincere appreciation to B. D. Mulhall, K. L. Thuleen, G. A. Madrid, F. B. Winn, and D. W. Trask of the JPL Tracking and Orbit Determination Section who played a very active part in the Mariner 9 station location support.

The Mariner Mars 1971 Project and its navigation team were very helpful in providing computer support during the approach phase, when numerous data sets were being studied. T. W. Thornton, W. J. O'Neil, C. J. Vegos, S. K. Wong, S. J. Reinbold, and A. Lubeley deserve special mention in this regard.

References

1. Mottinger, N. A., "Preliminary MM'71 Station Locations," Interoffice Memorandum 391.3-234, Jet Propulsion Laboratory, Pasadena, Calif., Dec. 29, 1970 (JPL internal document).

2. Muller, P. M., Anderson, J. D., and Vegos, C. J., "Equations and Program for the Combination of Statistical Estimates," in *The Deep Space Network*, Space Programs Summary 37-47, Vol. II, pp. 41–44. Jet Propulsion Laboratory, Pasadena, Calif., Dec. 30, 1967.

3. Mottinger, N. A., "Status of DSS Location Solutions for Deep Space Probe Missions: Third Generation Orbit Determination Program Solutions for Mariner Mars 1969 Mission," in *The Deep Space Network*, Space Programs Summary 37-60, Vol. II, pp. 71–89. Jet Propulsion Laboratory, Pasadena, Calif., Nov. 30, 1969.

4. Mulhall, B. D., et al., *Tracking System Analytic Calibration for Mariner Mars 1969*, Technical Report 32-1499. Jet Propulsion Laboratory, Pasadena, Calif., Nov. 15, 1970.

5. Chao, C. C., "New Tropospheric Range Corrections with Signal Adjustment," in *The Deep Space Network Progress Report for September and October 1971.* Technical Report 32-1526, Vol. VI, pp. 67–82. Jet Propulsion Laboratory, Pasadena, Calif., Dec. 15, 1971.

6. Winn, F. B., Chao, C. C., and Leavitt, R. K., "TSAC Tropospheric Refraction Calibration Polynomials, Revised," Interoffice Memorandum 391.3-462, Jet Propulsion Laboratory, Pasadena, Calif., Sept. 22, 1971 (JPL internal document).

7. Hamilton, T. W., and Melbourne, W. G., "Information Content of a Single Pass of Doppler Data from a Distant Spacecraft," in *The Deep Space Network*, Space Programs Summary 37-39, Vol. III, pp. 18–23. Jet Propulsion Laboratory, Pasadena, Calif., May 31, 1966.

8. Fliegel, H. F., "A World-Wide Organization to Secure Earth Related Parameters for Deep Space Missions," in *The Deep Space Network Progress Report for July and August 1971.* Technical Report 32-1526, Vol. V, pp. 66–73. Jet Propulsion Laboratory, Pasadena, Calif., Oct. 15, 1971.

9. Lambeck, K., "Comparisons and Combinations of Geodetic Parameters Estimated from Dynamic and Geometric Satellite Solutions and from Mariner Flights," paper presented at the XII Plenary Meeting of COSPAR, Prague, Czeckoslovakia, May 11–24, 1969, sponsored by the Smithsonian Institute Astrophysical Observatory, Cambridge, Mass.

10. Lieske, J. H., et al., "Simultaneous Solution for the Masses of the Principal Planets from Analysis of Optical Radar and Radio Tracking Data," *Celestial Mechanics*, Vol. 4, 1971.

Charged Particles

G. A. Madrid

I. Introduction

Calibrations compensating for the effects of charged particles in the ionosphere and in the interplanetary medium were applied to the doppler tracking data acquired during Mariner 9 missions on a demonstration basis. The combined effects of the space plasma and the ionosphere were measured by a comparison of the range and doppler observables (Differenced Range Versus Integrated Doppler (DRVID), MacDoran, Ref. 1). Independent measurements of the ionospheric effects were obtained from polarimeter devices located at the Goldstone, California, tracking complex.

The following is a summary of the analysis of the calibration technique and the demonstration results:

(1) Calibration quantity and quality.

(a) DRVID and Faraday rotation calibrations taken during the period from July 7 to September 26 were applied to a corresponding arc of doppler data from DSSs 12 and 14.

(b) Only 41% of the Mu DRVID (DSS 12) data and 14% of the Tau DRVID (DSS 14) data were of acceptable quality.[1]

(c) Main reasons for the degradation of DRVID quality were:

(i) Segmented passes (discontinuities).

(ii) Lack of signal strength (this appears as an increase in the phase jitter and was observed on data from DSS 12 only; probable cause appears to be the use of a 26-m antenna instead of the 64-m antenna).

(d) All other specifications met.

(2) Recommendations.

(a) The minimum received ranging signal strength must not be less than −194 dBmW. A maximum integration time of 15 min must be used

[1]Gaps due to degradation or lack of DRVID were filled with Faraday rotation calibrations where possible.

in order to detect signatures with periods of 1 h.

(b) Continuous range and doppler passes of 8 h or longer should be taken whenever high-quality DRVID calibrations are desired.

(c) At least one pass per week should be taken throughout a mission to permit sufficient coverage for long arc solutions. Preliminary estimates of short arc effects indicate that extensive coverage just before and after a maneuver should be a requirement.

(d) Drift and jitter specifications should be allotted to both the ground station and the transponder.

II. Characteristic Effects of the Charged-Particle Environment on Mariner 9 Radio Metric Data

The two major sources of charged particles which affected radio metric data between the earth and the Mariner 9 spacecraft were those particles emanating from the sun in what is called the solar plasma and those particles in the ionized upper layers of the earth's atmosphere. The first-order effect of these particles on a radio signal is a retardation of the group velocity and an advancement of the phase velocity. These effects, when left uncalibrated, distorted the information content of range and doppler and increased the error in estimates of the probe state.

The Mariner Mars 1971 mission required only that its prime observable, two-way doppler, be calibrated. Since DRVID measures only the rate of change of charged particles in the ray path, it is a suitable calibration for this observable.

A. Solar Plasma Effects

Charged-particle phenomena due to solar activity have been hypothesized to occur in one of three main forms:

(1) A steady-state solar wind that propagates as the inverse square of distance from the sun.

(2) Particles which are ejected by solar flares and which disseminate outward as spiral streamers.

(3) Magnetically enhanced sectors which also take on a spiral appearance.

These phenomena can distort a doppler signal when the particles of which these effluents consist traverse the transmission path of the radio signal.

The steady-state effects are discernible in the doppler data, due to the motion of the earth and spacecraft relative to the sun, and appear as a systematic type of error. Efron and Lisowski (Ref. 2) provide a basic insight into the effects of the solar wind and the parameters that determine the degree of influence. The basic parameters are:

(1) The sun–earth–probe angle and its time rate of change.

(2) The geocentric distance of the probe and its rate of change.

The structure of the solar wind on a time scale of a few hours is not known and is likely to be highly variable. Solar flares are the major source of random solar effects. Some recurrent components, such as magnetic enhancement sectors, have periods of 27–28 days and may present a problem since they will not average out. For these phenomena, an additional set of parameters are involved. The parameters are:

(1) The velocity of the plasma cloud or sector.

(2) The dimensions and density distribution of the plasma cloud or sector.

(3) The angle of traversal.

All of the solar phenomena are highly dependent on the phase of the solar activity cycle during which these effects are being observed. For the period during which calibrations were taken during the MM'71 mission, the level of solar activity can be clearly established. Figure 1 (Ref 3) illustrates the solar activity cycle in terms of radio flux detected at 2800 MHz during the years 1947 to 1969. The activity level during the mission is reflected by the flux measurements[2] plotted in Fig. 2. By comparison, it can be seen that the solar activity during the MM'71 mission was on the decrease, with the level of activity being in mid-range between the typical maximum and the typical minimum.

The geometric location of the ray path with respect to the sun is also an important parameter in determining plasma effects. In general, the smaller the sun–earth–probe (SEP) angle, the greater the effect. The sun–earth–probe

[2]Unofficial flux measurements reported in the weekly ESSA publication, "Preliminary Report and Forecast of Solar Geophysical Data," SCSC-PRF 056, December 1, 1971.

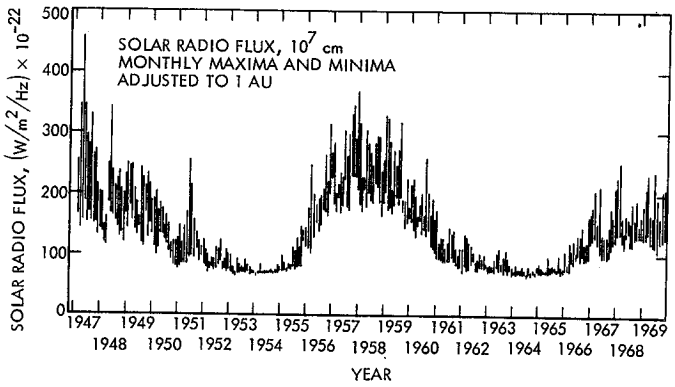

Fig. 1. Solar activity cycle based on solar flux readings (ESSA, Solar-Geophysical Data, Number 306, Supplement, p. 7)

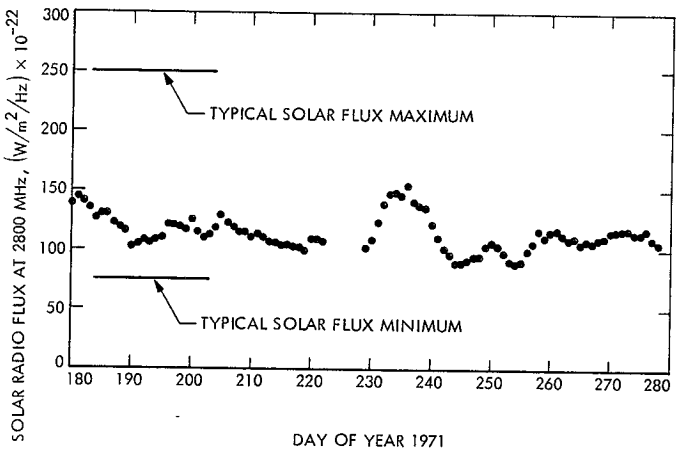

Fig. 2. Solar activity as measured by Ottowa solar flux adjusted to 1 AU

angle for MM'71 at the period of interest is typically 120 deg (see Fig. 3). The earth–spacecraft distance and the distance of the ray path normal to the sun are approximately 0.8 and 1 AU, respectively. Estimates based on this geometry indicate that the steady-state effects will introduce uncertainties of 1 and 2 m in spin axis and longitude for single-pass doppler fits (Efron and Lisowski, Ref. 2). Random effects will be approximately 2 to 3 m in magnitude for the same parameters (Mulhall, Ref. 4).

B. Ionospheric Effect

The ionospheric doppler effect will vary with the local time of observation, the local hour angle, the topocentric elevation angle of the observations, and the solar activity cycle. Typically, the nighttime ionosphere is relatively quiet and stationary; the daytime ionosphere, however, is 2 to 6 times more active and has a time-varying structure.

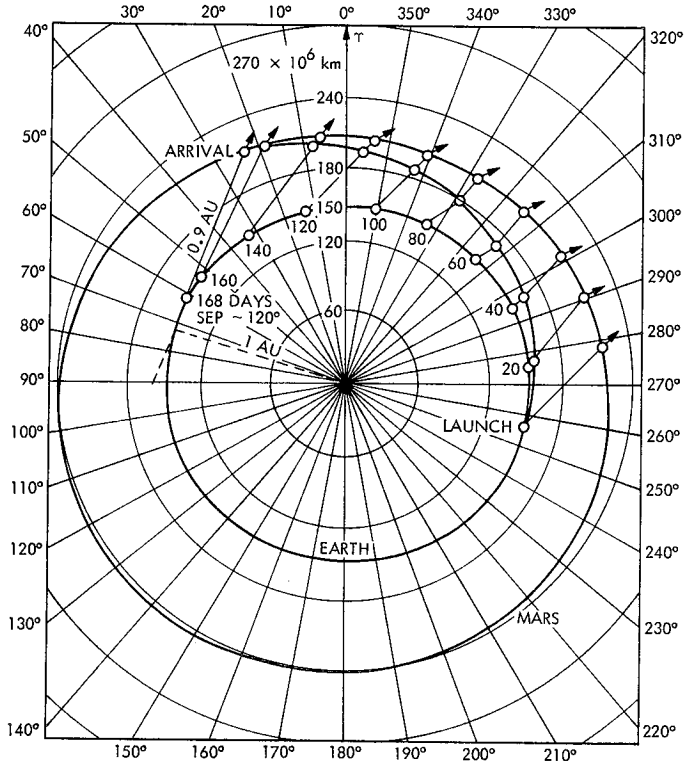

Fig. 3. MM'71 geometry

Figure 4 represents the typical zenith columnar electron count over Goldstone for any 24-h period of the summer and fall of 1971. In particular, note that stations in the Goldstone Deep Space Communications Complex viewed Mariner 9 at night during the month of June; thus the S-band radio signals did not penetrate any active regions of the earth's ionosphere. This situation changed little during most of July; however, by August 1, the rising of Mariner 9 as viewed from Goldstone had moved into early evening (~19:00) and the ionosphere at the observer's meridian was undergoing its maximum decrease. At the time of Mariner 9's encounter with Mars (16:00 local time), the earth's ionosphere at the local meridian was near maximum activity. Thus, it is shown that the portion of the earth's ionosphere traversed by the S-band radio signals of Mariner 9 assumed radically different characteristics as the MM'71 mission progressed.

Figure 5b demonstrates the range and doppler charged-particle effects when mapped to the spacecraft line of sight. The resulting signature is a function of elevation angle, local time, and geomagnetic factors. The total zenith content is also plotted in Fig. 5a. Case I (Fig. 5) considers the situation where the spacecraft view period

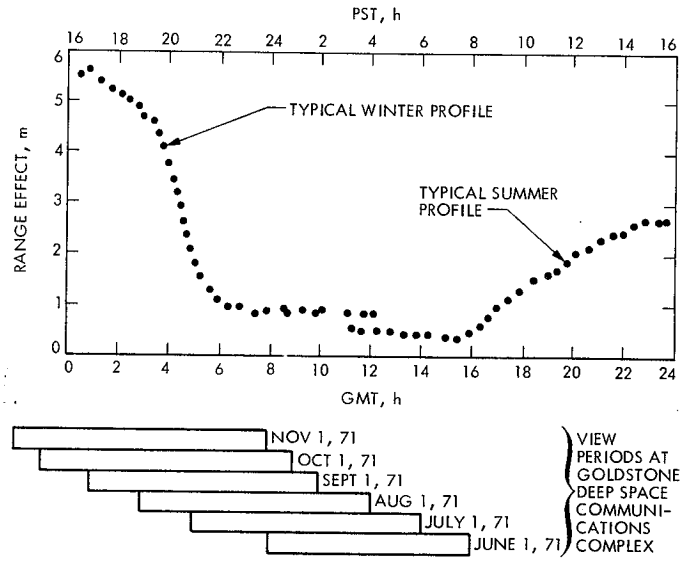

Fig. 4. Typical effects of charged particles on range observables at zenith

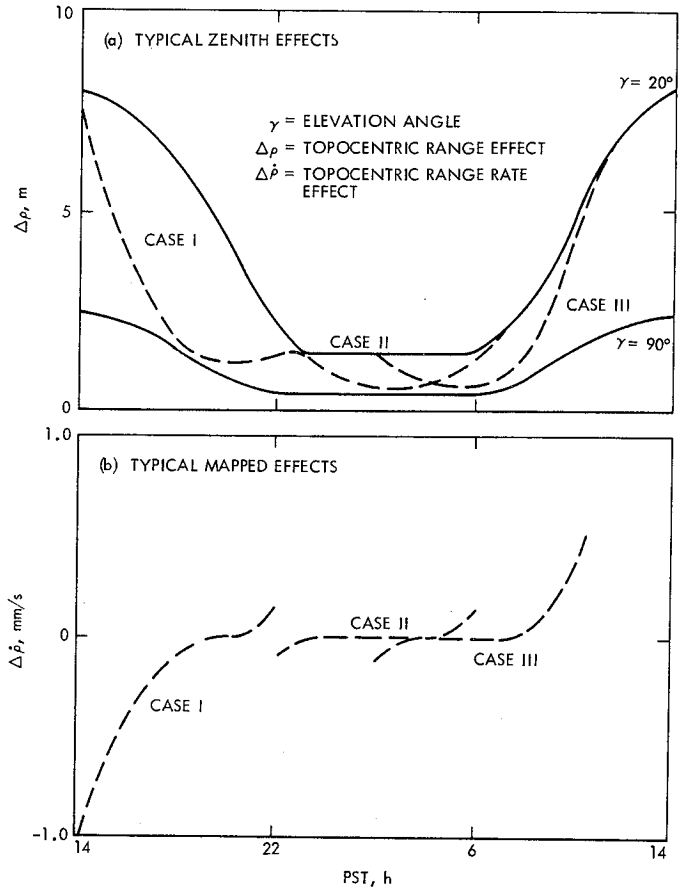

Fig. 5. Mapping af zenith charged-particle effects to various elevations

starts at the most active region of the ionosphere and sets at the least active region. Case II considers the view period remaining entirely within the quiet nighttime ionosphere and sets at the least active region. Case III shows a view period beginning during the quiet ionosphere and ending at the time of greatest change in ionospheric activity.

In general, the summer zenith electron content effects recorded varied from a low of 0.5 m during the nighttime period to peaks of 2–3 m during the daytime. These measurements were taken during periods when doppler information was being received. When mapped to the spacecraft line of sight, these values agree quite closely with the typical plots shown in Fig. 5.

The winter zenith effects vary from nighttime lows of 0.9 m to peaks ranging from 5–6 m. The MM'71 encounter occurred during this type of period. The data arcs calibrated for this study were all taken during the summer (see Section III-A for a description of coverage) and thus were affected by the more benign summer conditions.

C. Credibility of Single-Pass Fit Predictions Relative to Actual MM'71 Experience

It is interesting to compare MM'71 prognostications with our actual experience during the mission. Figure 6 shows the estimated equivalent effects[3] on station position

[3]These effects were computed using the Hamilton–Melbourne relationship for the effects over a single pass of data (Ref. 5) with a technique similar to that reported by Mulhall (Ref. 6).

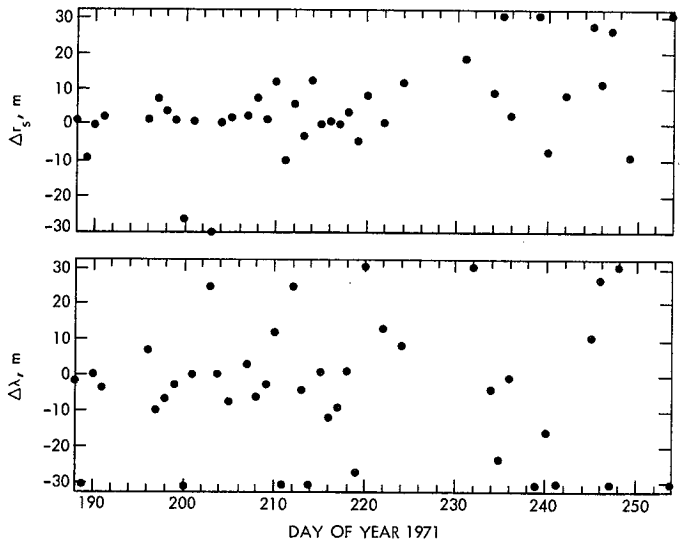

Fig. 6. Equivalent spin axis and longitude effects due to charged particles during MM'71 mission

of the DRVID calibration polynomials when the DRVID data were of sufficient quality to be useful. The spin axis effects have a negative bias with a 1-σ uncertainty of about 5 m. The longitude effects have a negative trend with a 1-σ uncertainty of about 8 m. Since these numbers include both the ionosphere and space plasma effects, they must be compared to the root-sum-square of the predicted effects for those two media. Table 1 compares the predicted and actual values of the equivalent station location errors (ESLE).

Table 1. Predicted vs estimated equivalent station location changes due to charged-particle effects over 60 passes

MM'71 values	σ_{r_s}, m	σ_λ, m
Predicted	~2.5	~4
Result	~5	~8

Most of the resulting discrepancy can be attributed to the fact that the predicted performance was based on high-quality continuously calibrated passes, a condition which was not achieved during most of the MM'71 mission; as a result, Faraday rotation data were used for the major portion of the passes.

Comparisons of the Faraday and DRVID polynomials revealed drifts with excursions on the order of 1 m for the majority of the days being considered. On occasional days, the maximum excursion reached 2.5–3.0 m. These days have been singled out for special attention to determine if these differences were due to any significant solar activity. The 1-m drifts conform with the estimate of the steady-state solar wind effects for MM'71. The random events of 2.5 to 3.0 m agree with Mulhall's conclusions (Ref. 4) on sporadic solar effects on radio metric data.

III. Measurement of the Charged-Particle Effects

During the Mariner Mars 1971 mission there were two means available to estimate the effect of charged particles on the radio signal:

(1) By means of radio polarimeters to detect Faraday rotation effects in the ionosphere.

(2) By comparing the range and doppler signals (DRVID) to obtain a measure of the rate of change of charged particles in the ray path.

Coverage from these two methods was quite distinct, as was the quality of the data received. Subsequent paragraphs address themselves to this topic so as to provide a clear understanding of the data resources available and the constraints affecting their use.

A. Coverage Obtained and Amount Utilized

The presence of two ranging machines at two of the Goldstone stations permitted DRVID to be obtained on 103 out of the 167 days between May 21, and November 13, 1971. However, of this number only 37 days were used to calibrate the doppler radio metric data over the span selected for analysis (July 7, to September 26, 1971).

The Tau ranging machine was located at DSS 14 (64-m antenna) and provided DRVID at 1-min integration times (2-min sample rate) from May 31 to November 8 at periods of about once per week. The Mu ranging machine was located at DSS 12 (26-m antenna) and provided supplementary coverage on the average of four times per week. Integration times were 1 min until October 10, when 2-min integration times were begun. Faraday data were available from July 7 and ending on October 12. Exact days for which coverage was provided are shown in Fig. 7. Also shown is the scatter of the noise about the fit (see Section III-C for description) plotted on a day-by-day basis. The 1-m requirement is indicated by a broken line.

The orbit determination effects to be analyzed in a subsequent section used only the calibrations for day 188 through day 268, as indicated by the "combined DRVID and Faraday" bars at the bottom of Fig. 7. Calibrations prior to day 188 were not utilized because of their sparsity and a lack of Faraday data, which were to be used for comparison. Continuous coverage was accomplished by using the overlapping coverage afforded by DSS 14 DRVID, DSS 12 DRVID, and Faraday rotation polarimeters located at DSS 13. The study was begun on September 27 (day 270); data taken after this date were not utilized in this study.

Not all of the DRVID data obtained were suitable for use in calibrating tracking data. For instance, DRVID data from the Mu ranging system at DSS 12 became unsuitable when the noise level went above 50 ns (see Section III-C). It became evident that, at this level, the least-squares fit to the data could not accurately distinguish between trends due to charged-particle phenomena and high-frequency noise. Some passes of DRVID from both DSSs 12 and 14 also had to be discarded

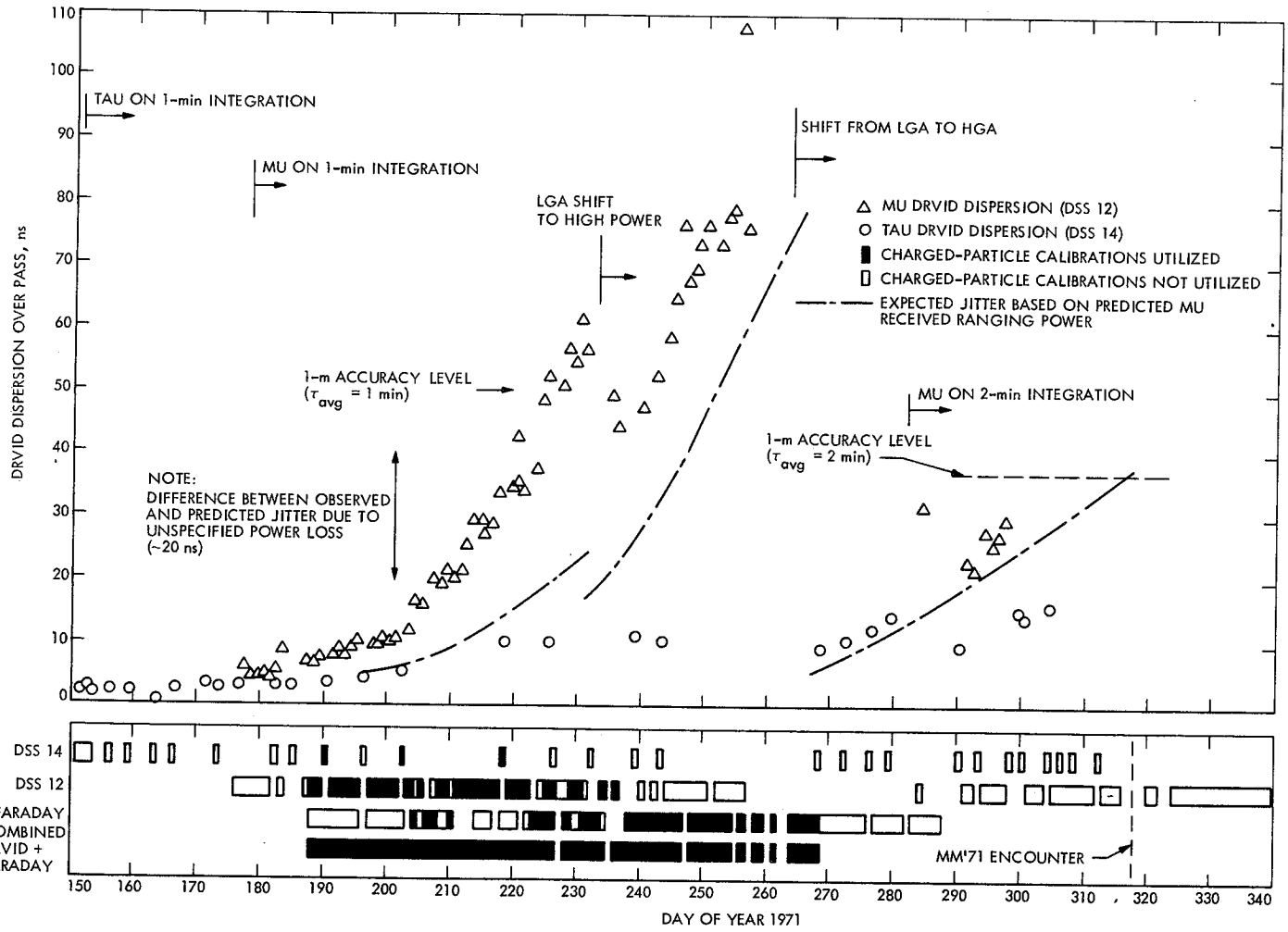

Fig. 7. Charged-particle calibration coverage and DRVID dispersion for MM'71 cruise phase

because of multiple ranging acquisitions taken during the pass. In some cases, as many as 14 acquisitions took place, resulting in 10-min segments of contiguous DRVID separated by light time gaps of 10 min or more. The phenomena effects were completely lost because each segment had to be fitted individually.

As a result of these operational difficulties, only 14% of the DSS 14 DRVID and 41% of the DSS 12 DRVID were of a quality suitable for use as a calibration measurement over the study interval (see Section III-C). Discarded or missing DRVID passes were filled with Faraday rotation data as indicated in Fig. 7.

Table 2 summarizes the amount of DRVID and Faraday calibration data utilized in the period from July 7 to September 26, 1971.

B. Faraday Rotation

During the MM'71 mission, measurements were taken by observing the Faraday rotation effect on a signal from a stationary satellite (ATS-3) and then mapping these effects to the Mariner 9 spacecraft line of sight. Faraday polarization measurements can provide an absolute measure of the electron count along a given ray path through the ionosphere by relating it to the nighttime electron content at zenith (approximately 0.9 of a meter for the period being considered).

During periods of low solar activity, Faraday measurements can be used in combination with DRVID measurements to provide a continuous set of calibrations for a given period. Faraday rotation data are characteristically smooth and lend themselves well to representation by

Table 2. Assessment of DRVID and Faraday utilization

Calibration type	Doppler points[a]			Passes		
	Total	Number calibrated	Percentage calibrated	Total	Number calibrated	Percentage calibrated
Tau (DSS 14)	188	51	27	7	3	43
Mu (DSS 12)	1168	473	40	55	37	67
Faraday	1262	908	74	81	61	75
Faraday/Tau/Mu[b]	1272	864	68	81	74	91

[a]Doppler points were compressed to 600 s for orbit determination use.

[b]The number of doppler points calibrated is smaller because DRVID passes were in general shorter than the Faraday passes they replaced in the combined calibrations.

polynomials (Fig. 8). A polynomial is obtained for every day processed and these are then made available for use in the orbit determination program (Mulhall et al., Ref. 7).

Faraday rotation measurements have been compared to ionosonde measurements (Mulhall and Wimberly, Ref. 8) and to other Faraday measurements made at various locations (Miller and Mulhall, Ref. 9). Von Roos and Mulhall (Ref. 10) have estimated that for this technique the range error accumulating over a pass will be on the order of 1.5 m in summer and 0.5 m in fall, winter, and spring.

JPL currently has two experimental polarimeters located in the vicinity of DSS 13, which have, in the past, been used to support research on the effect of ionospheric charged particles on radio metric data.[4] Since there are no plans to make these instruments operational, they are not committable for mission support. Their use during the MM'71 mission was on a "best efforts" basis and involved a minimum use of operational personnel.

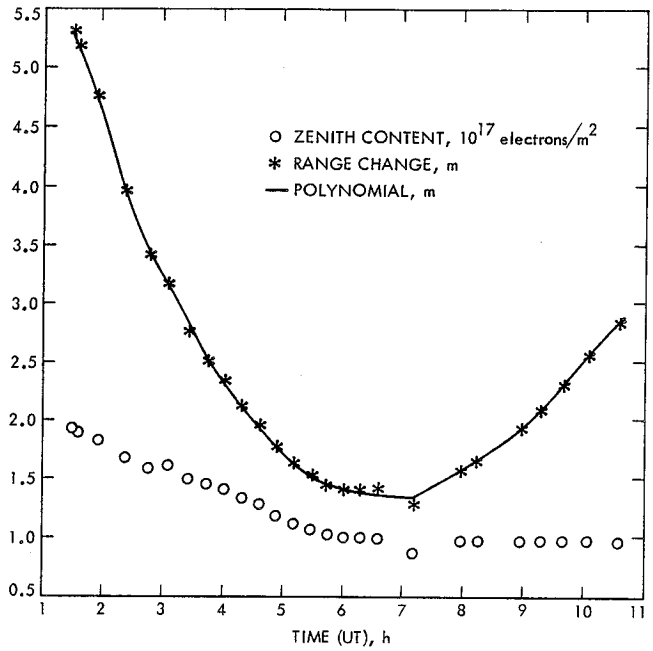

Fig. 8. Typical fit to mapped electron content obtained by Faraday polarimeter

C. DRVID

The concept of extracting the charged-particle effects on a radio signal by comparing Differenced Range Versus Integrated Doppler (DRVID) has been extant for a decade. The feasibility of the method was not established, however, until the extended mission of MM'69 (MacDoran and Martin, Ref. 11). MacDoran (Ref. 1) provides a clear understanding of the physics involved in this method.

It will be sufficient here to define DRVID as

$$\text{DRVID} \approx 2\,\Delta\rho_\varepsilon = (\rho_2 - \rho_1) - \int_{t_1}^{t_2} \dot{\rho}\, dt$$

where

$\Delta\rho_\varepsilon$ = two-way change in range due to effects of electrons in media

ρ_i = topocentric range of probe at time t_i $(i = 1,2)$

$\dot{\rho}$ = instantaneous radial velocity of probe relative to observer

[4]Stanford University has provided data from their polarimeter as part of these investigations.

The reason that the definition above is not equivalent to zero is that, at S-band, the disagreement between differenced range and integrated doppler will equal approximately twice the change in charged particles along the round-trip ray path, since the effect of the charged particles is essentially equal and opposite (Ref. 1). This method has the advantage of directly measuring the effect of the charged particles on the radio metric tracking data. Since the DRVID values reflect the noise on the range (doppler system noise is negligible), a polynomial least-squares fit to the DRVID data was used as a smoothing procedure prior to its use in the orbit determination program during the MM'71 mission.

There is no question that DRVID is a measure of the change in the charged-particle content along the round-trip path of an electromagnetic signal. This has been adequately documented by MacDoran (Ref. 1), MacDoran and Martin (Ref. 11), and other authors and can be easily demonstrated by comparing DRVID with Faraday rotation during days of negligible solar activity. Figure 9 demonstrates this empirical equivalence by showing the DRVID observed alongside the mapped Faraday values (top panel) and the flat distribution of their differences (bottom panel). This comparison is for day 190 (July 9) when the spacecraft was 0.1 AU from earth and the solar radio flux (Fig. 2) was at one of its lowest points during the mission. The scatter of the differences had a standard deviation of 0.4 m, which is well within the 1.0-m goal proposed for DRVID.

The accuracy of the DRVID calibrations depends on two components:

(1) The accuracy of the process producing the polynomials.

(2) The accuracy with which DRVID measures the charged-particle effects.

The design of the fitting procedure is the subject of the article by R. K. Leavitt in this report. It will suffice to say that the accuracy of the fitter with respect to its selection criteria has been verified by comparing the variance of the fit to the variance of the Gaussian noise used to produce the simulated data for testing. The effectiveness of this fitter is demonstrated by the realistically smooth derivatives produced from the fitted polynomial. Figure 10 provides an example of a typical fit to DRVID data with a polynomial and its associated derivative.

Of greater interest for this discussion is the study of the effect of system noise on the fitting accuracy, the

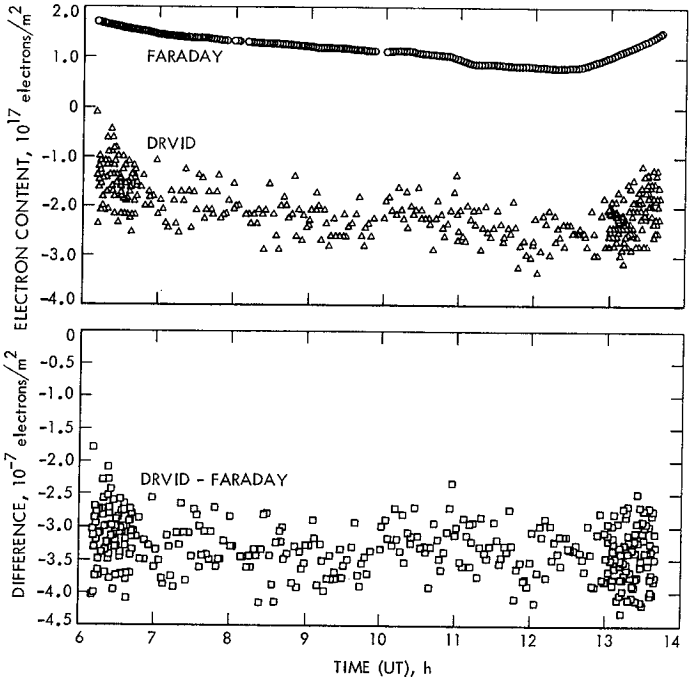

Fig. 9. Comparison of mapped electron content to DRVID on day with low solar activity

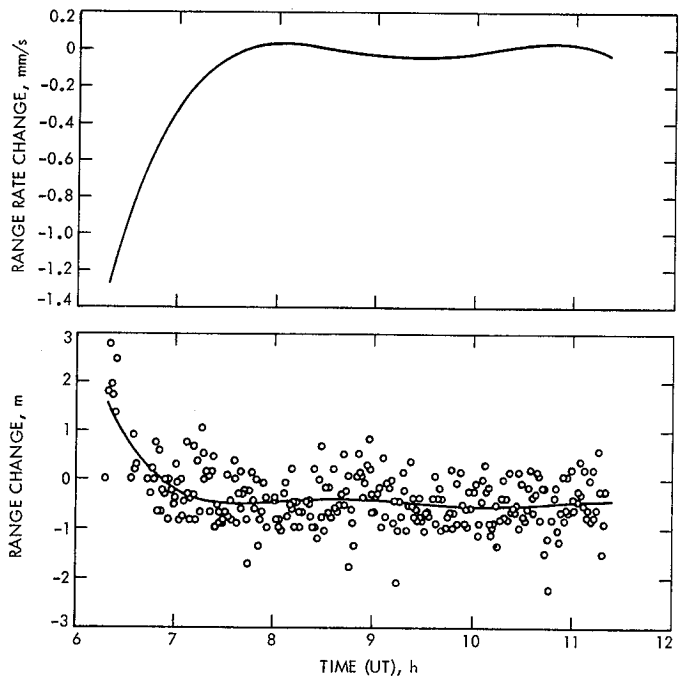

Fig. 10. Typical polynomial fit to DRVID and associated range rate signature

Table 3. DRVID drift and jitter requirements

Noise type	Requirements for 1-m calibration tolerance
Long-term (12-h) drift (3-σ)	24 ns (ground station) 33 ns (spacecraft)
Short-term (15-min) ranging jitter (3-σ)	81 ns

system noise in question here being those time-varying effects of instabilities in the ground station transmitter–receiver and in the spacecraft transponder.

System noise exhibits itself in DRVID as short-term jitter and long-term drift. Long-term drift is due to instabilities in both the ground station tracking system and in the spacecraft transponder. Short-term ranging jitter is ascribed mainly to the signal-to-noise ratio of the signal. Table 3, taken from MacDoran (Ref. 12), provides a guide to the tolerance that must be kept in order to be able to discern the charged-particle effects to within 1 m.

MacDoran (Ref. 12) determined the characteristics required of DRVID by simulating a signal varying the jitter effects and then attempting to recover the original signal. Figure 11 is a summary of his results.

Drift does not adversely affect the quality of the polynomial fit, but high-frequency noise does, particularly when short segments of data are involved. The results, of course, depend on the length of the segments. Figure 12 maps the 27-ns requirement with respect to segment length and averaging time. Two-hour lengths were found to be the minimum at which diurnal trends could be detected. Fifty nanoseconds is the 1-m accuracy level corresponding to this segment length for 1-min integration times.

Table 4 classifies the various levels of error that can affect polynomial quality while Fig. 13 illustrates the major factors affecting DRVID quality.

The MM'71 calibrations further showed that segmented passes in general could not be completely utilized regardless of the accuracy of the corresponding segments. The reason for this is that, since each segment must be fitted individually relative to different initial conditions, the resulting polynomials and their derivatives are nearly always disjointed and/or discontinuous at their juncture points.[5]

[5]Techniques to overcome this problem are planned for use in calibration processing for future missions.

Table 4. Classification of segmentation and noise on MM'71 calibrations at one-minute averaging time

Pass characteristics	High noise level (>50 ns)	Low noise level (<50 ns)
No segments, long passes	Type III (unacceptable)	Type I (acceptable)
Some segments, long/short passes	Type IV (unacceptable)	Type II (partially acceptable)

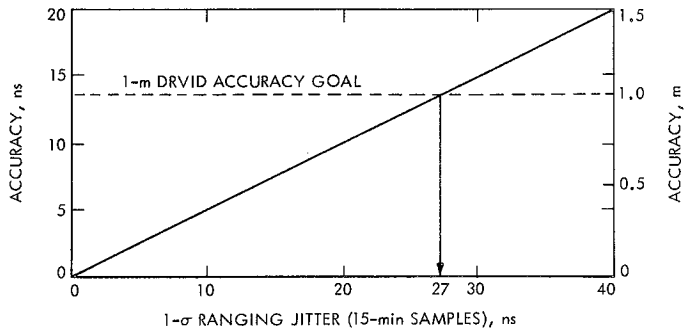

Fig. 11. Ranging jitter design parameter based on simulation results by MacDoran (Ref. 12)

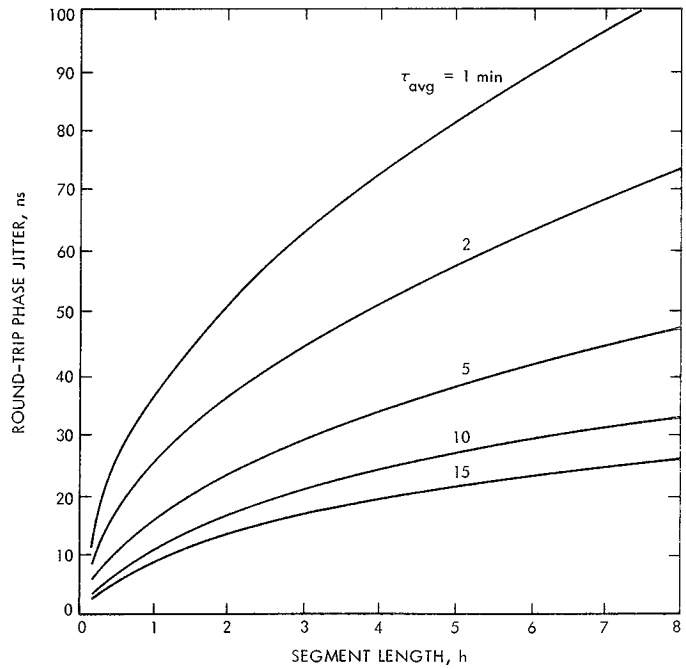

Fig. 12. Pass segment planning chart showing relationship of pass segment length to phase jitter over constant integration times

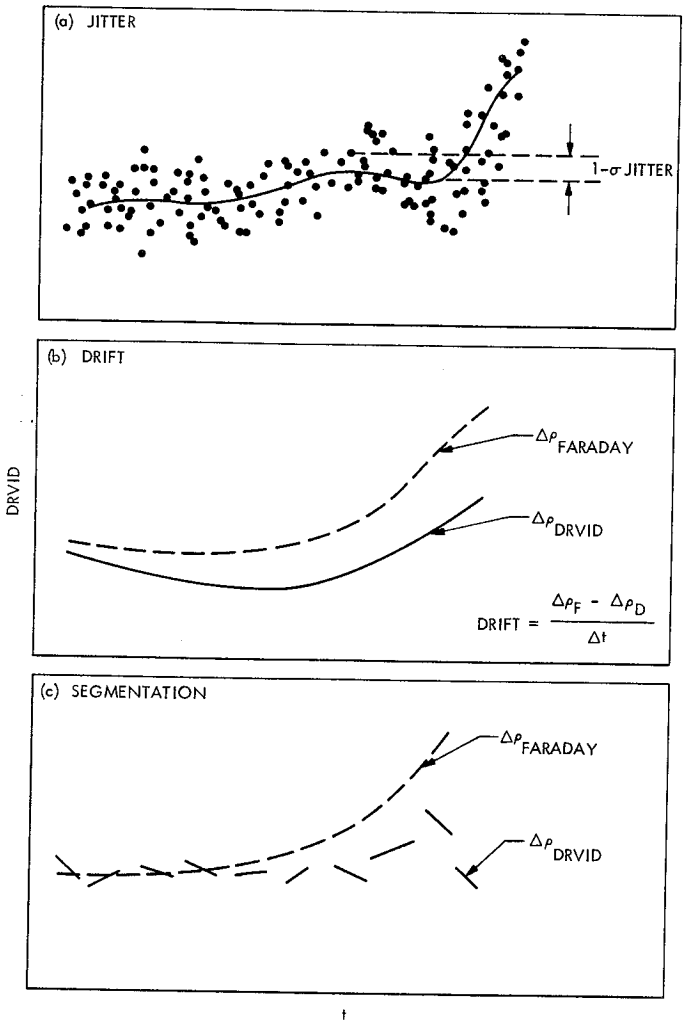

Fig. 13. Typical plots of major factors affecting DRVID quality

Figure 14 is typical of this type of situation. In such a case, only the longer segment should be used in calibrating the data if it is of a low noise level. Cases with a low noise level that are not segmented are acceptable with a probability of 1.

Table 5 is an assessment of the proportion of the DRVID calibrations available between day 188 and day 268, classified by type.

It has been demonstrated that the Faraday rotation data taken at the Goldstone complex provides a suitable standard for evaluating DRVID accuracy whenever solar activity is low enough to have negligible effects on a doppler signal. The period over which the calibrations were taken is concurrent with a phase of medium solar

Table 5. Assessment of DRVID calibration fits between day 188 and 268 types[a]

Data	Type I, %	Type II, %	Type III, %	Type IV, %
Mu DRVID (Total 55 days)	41	25	9	24
Tau DRVID (Total 7 days)	14	86	0	0

[a]Type I: Low noise (<50 ns), no segments.
Type II: Low noise, some segments.
Type III: High noise (>50 ns), no segments.
Type IV: High noise, some segments.

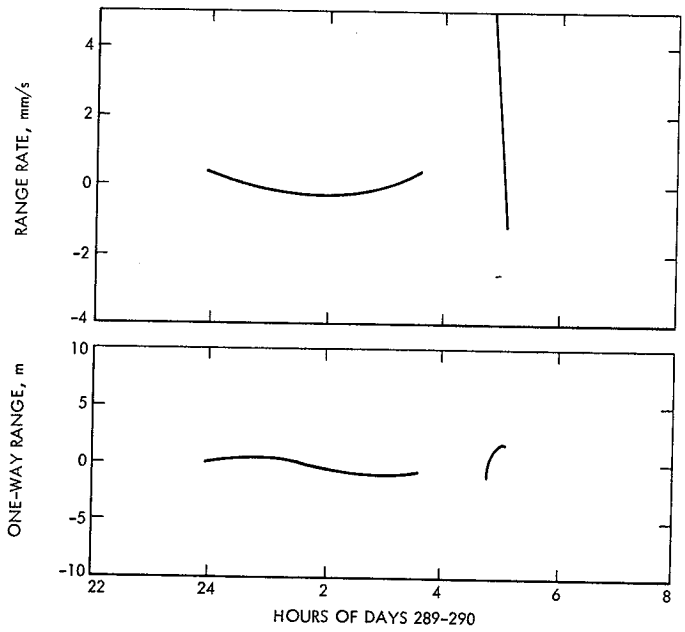

Fig. 14. Disjoint fit to segmented DRVID

activity (Fig. 2). The particular geometry of the Mariner 9 mission (Fig. 3) placed the probe 0.8 AU from earth at a sun–earth–probe angle of approximately 120 deg. If we follow Efron and Lisowski (Ref. 2), this would mean that the solar plasma effects would be only about 1.0 m in range change over a pass that is negligible compared to the expected 5- to 6-m effects of the ionosphere at encounter.

Errors in mapping the Faraday rotation data from the ATS-3 line of sight to the Mariner spacecraft line of sight are not expected to exceed more than 0.1 m (Ref. 9).

Short-term differences between the Faraday and DRVID data are expected, due to localized effects of the ionosphere relative to the spacecraft line of sight. These, again, are not expected to have amplitudes of more than 0.1 m.

Since many of the measurements taken during the MM'71 missions occurred during the quiet portion of the ionosphere and during periods of relatively quiet solar activity, DRVID measurements compared very closely to the Faraday rotation measurements. Comparisons of the two methods were made by differencing the polynomials obtained by each method. Figure 15 illustrates the typical comparison of the range correction as computed using the DRVID and Faraday polynomials. It should be noted that the comparison for the range change effect should be made on the basis of the shape of the two curves, the bias between them being purely a matter of the original reference point used for DRVID. The differences of their derivatives are perhaps of more interest, since it was only the doppler observables that were being calibrated. Figure 16 plots the derivatives and their difference for the same day as Fig. 15. It is evident that, at least for the data shown, DRVID and Faraday data appear to be measuring the same phenomenon.

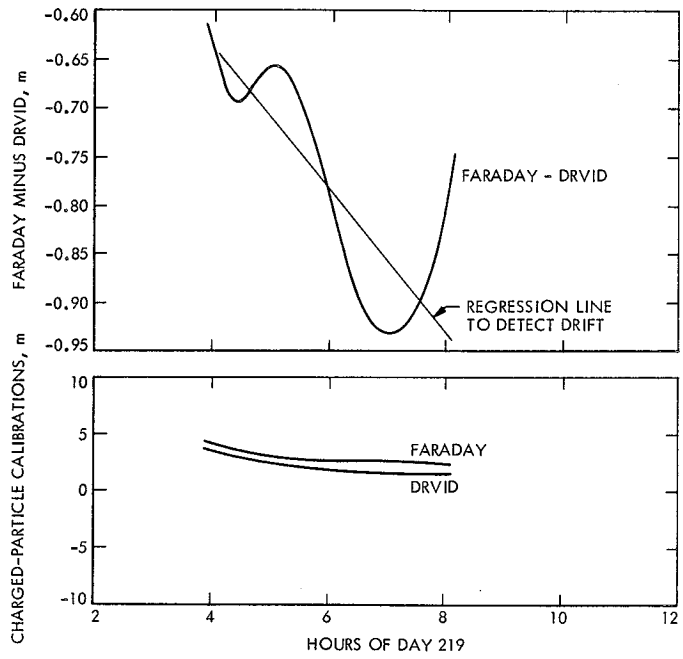

Fig. 15. Comparison of Faraday and DRVID calibration polynomials for day of low solar activity

Figures 17 and 18 plot the means and standard deviations of the differences and show that, in the early portion of the mission (up to 0.2 AU) where solar plasma effects are negligible, DRVID compares very well with Faraday rotation, as expected. After this point, the comparison becomes suspect, and anomalous behavior may be due to solar activity, high jitter, or too short a segment of DRVID. For the sake of illustration, only those days of DRVID which had segments over 2 h long and had sufficiently low noise quality were included in the plots for Figs. 17 and 18.

Assuming the Faraday data can be utilized as a standard for the majority of days, we can now use the standard deviation of the differences between the Faraday and DRVID data as a measure of the DRVID system accuracy in the presence of jitter during days of low solar activity. The drift error is provided by the slope of a linear fit to the range differences (Fig. 15, top panel). Plotting the drift and jitter error day by day through the time span under consideration, we can construct two graphs which illustrate the actual performance of DRVID.

The first graph, Fig. 19a, compares the jitter error directly to the expected 1-m accuracy level for 1-min integration time. The second graph, Fig. 19b, compares

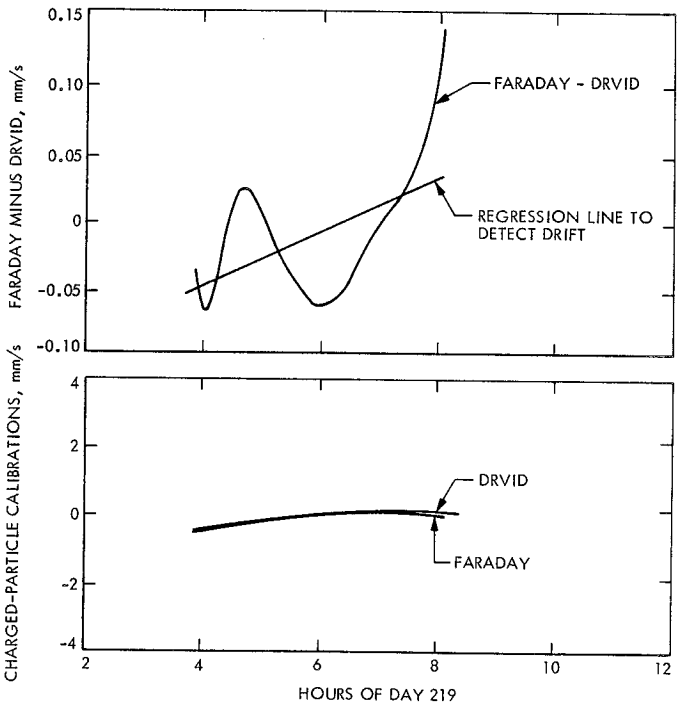

Fig. 16. Comparison of Faraday and DRVID range rate effects on day of low solar activity

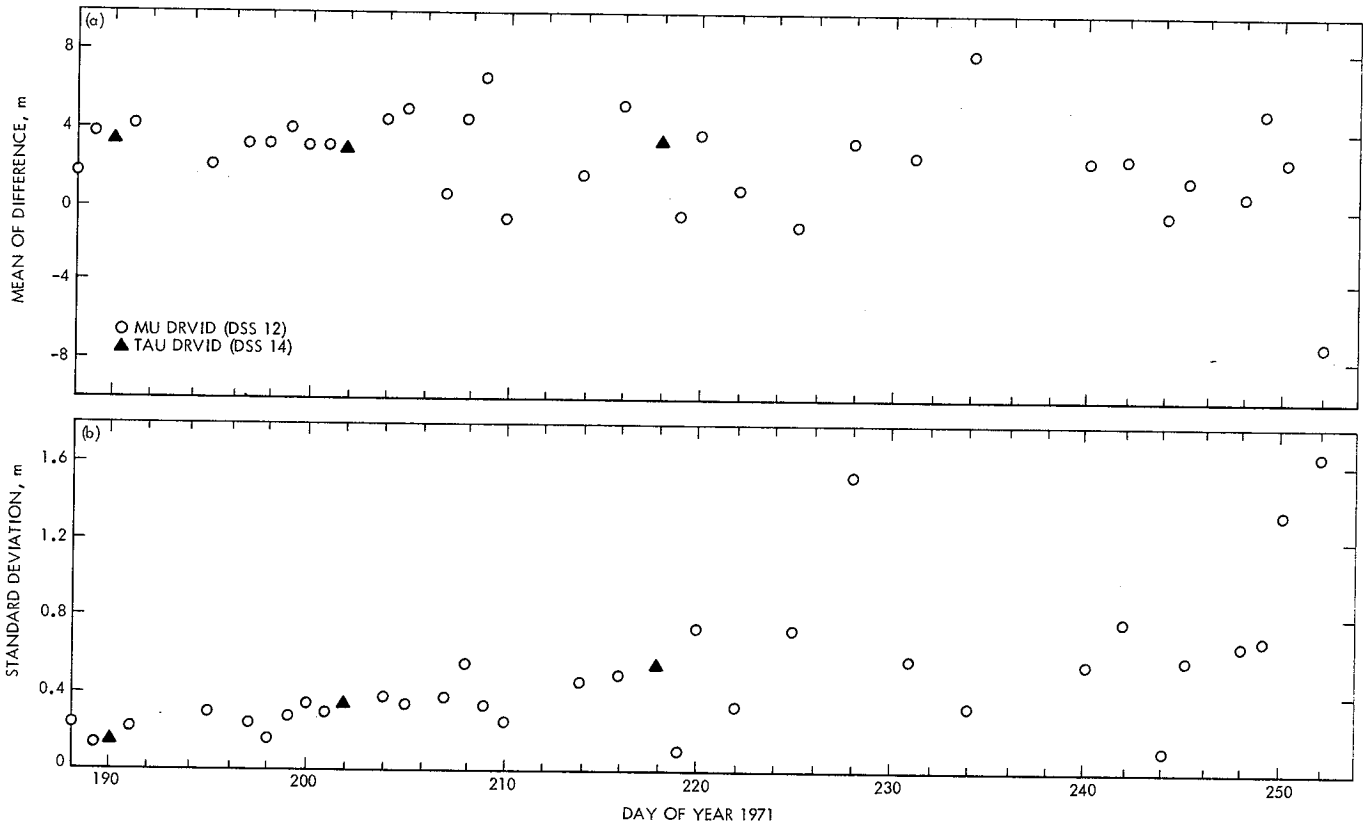

Fig. 17. Mean and standard deviation of differences between DRVID and Faraday range correction for DRVID passes exceeding 120 min

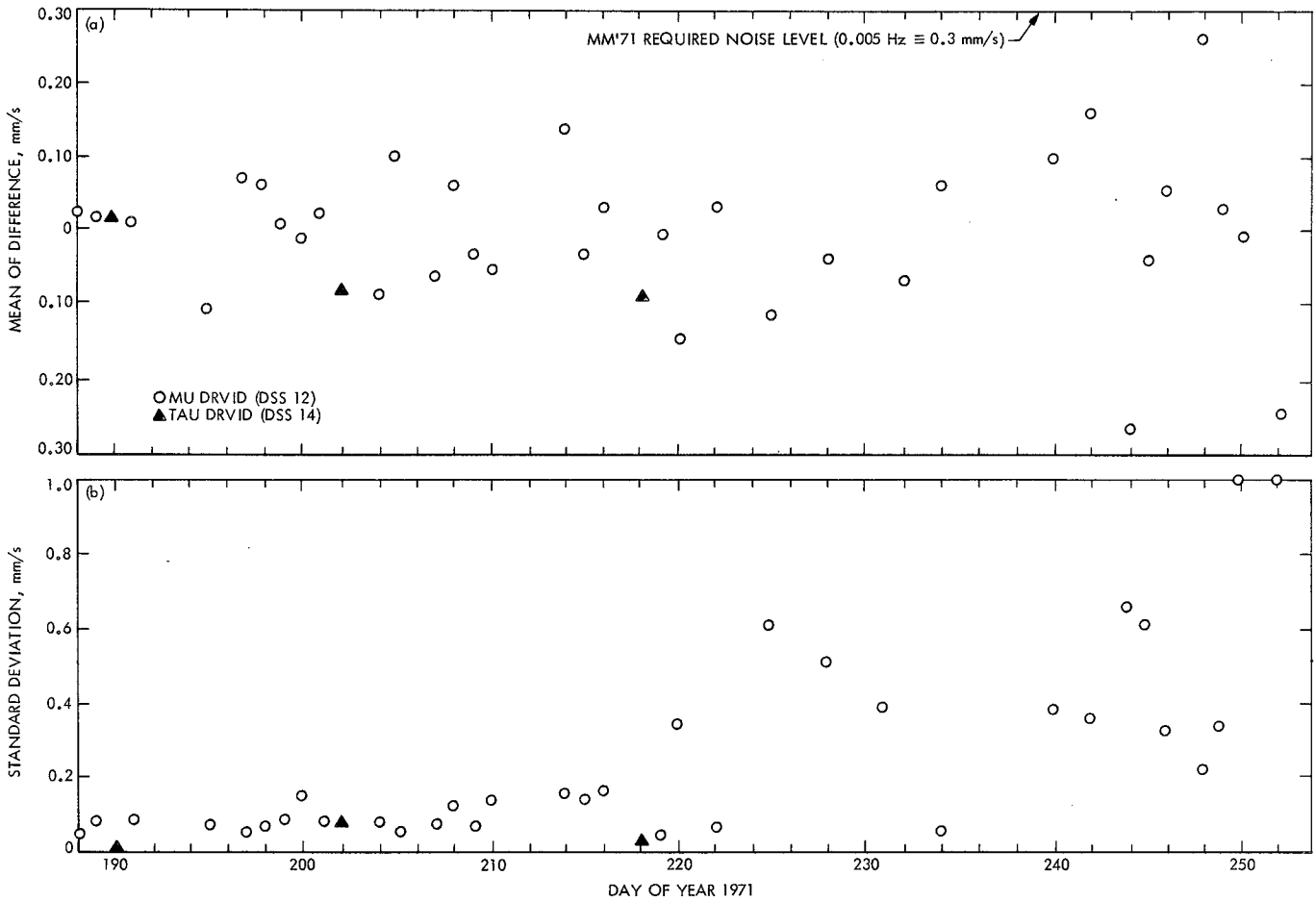

Fig. 18. Mean and standard deviation of differences between DRVID and Faraday range rate correction for DRVID passes exceeding 120 min

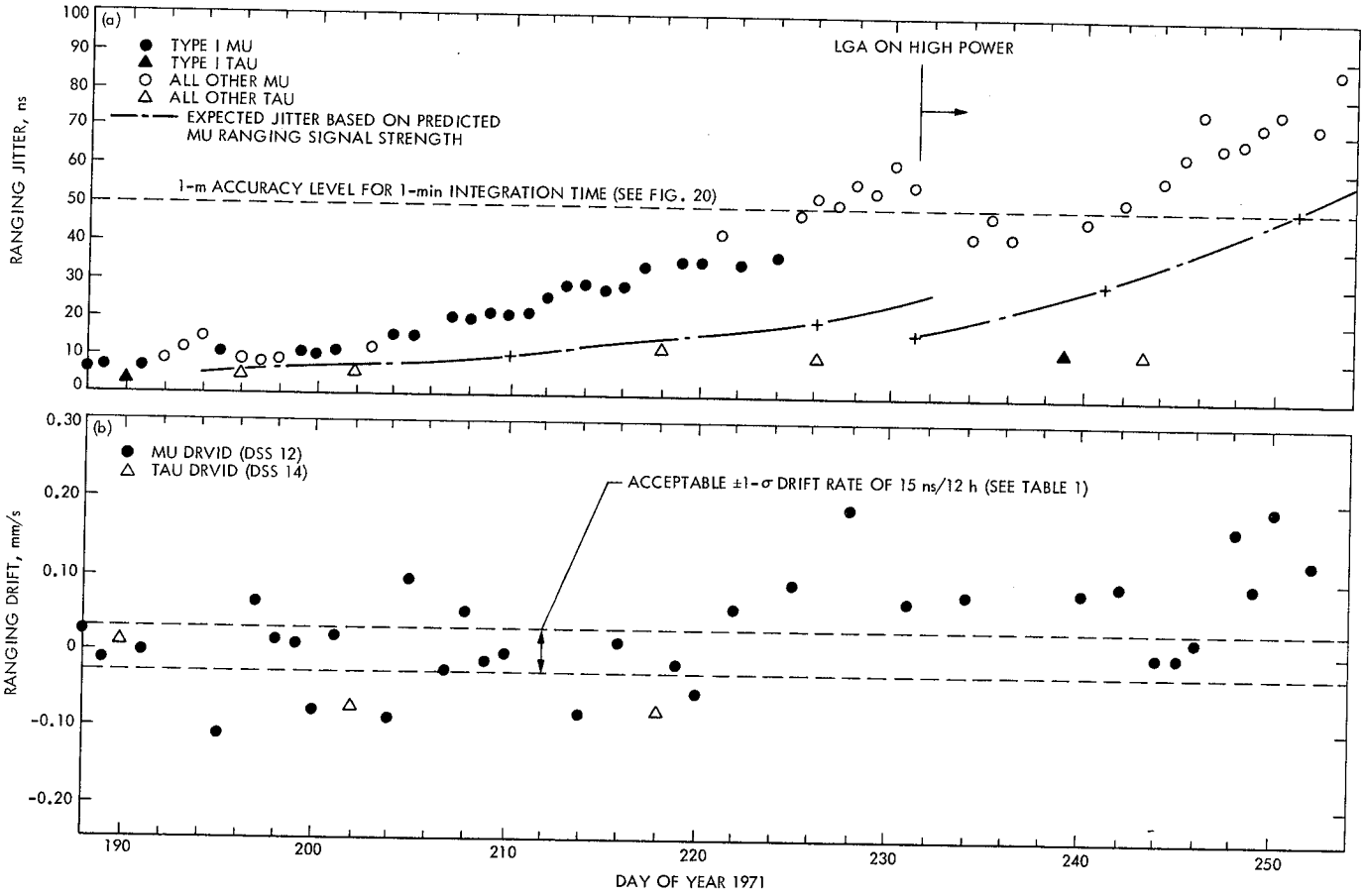

Fig. 19. Estimated ranging jitter and drift observed

the drift error[6] against the 15-ns/pass standard implied in Table 3. Figure 19a indicates that all Mu DRVID data until day 224 can be utilized for calibrations even though their accuracy has been degraded considerably. This evaluation of its acceptability is based on the comparison between the Faraday and DRVID calibration polynomials as shown in Figs. 17a and 18a. These two plots indicate that the uncertainty in the calibrations increases by a factor of 2 after day 224.

A comparison with the expected jitter based on the predicted ranging signal power (Figs. 7 and 19a) indicates that in general the jitter was a factor of 2 greater than that expected. The reason for this loss of performance may be due to some malfunction in the spacecraft transponder.[7] A detailed analysis of this problem has been undertaken by appropriate personnel cognizant of the ground system and spacecraft equipment.

Aside from the assumed transponder problems, it should be remembered that the DRVID from DSS 14 was obtained using the 64-m antenna at that site and therefore had a greater received power (−175 dBmW) than the 26-m antenna at DSS 12 (−195 dBmW).

In order to illustrate this concept more dramatically, a DRVID performance chart has been drawn up (Fig. 20) which indicates the interrelationship between high-frequency noise (jitter), integration time, and received ranging power. This chart can be used in complement with Fig. 12 to determine the received power and integration time parameters required to meet a 1-m accuracy requirement. The actual performance levels of the DRVID provided by the Tau and Mu ranging systems are

[6]The author did not have, at the time of this writing, a means for independently measuring equipment drifts. As a result, the overall drift level is presented here merely to orient the reader as to the general trend in the drifts. An evaluation of these effects is the subject of future study.

[7]Warren Martin, private communication, January 26, 1971.

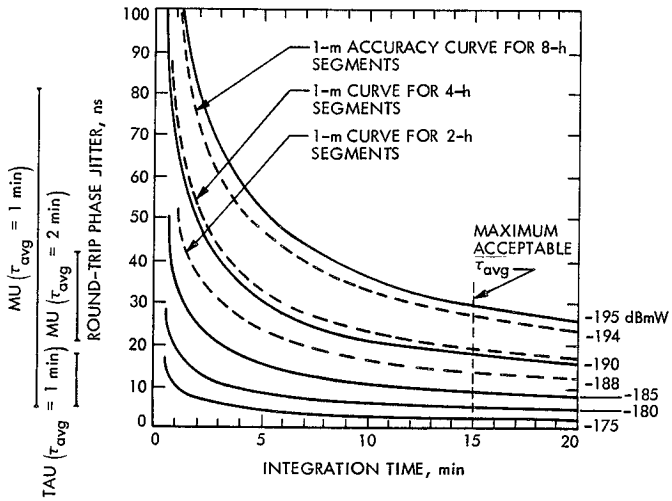

Fig. 20. DRVID performance chart showing relationship of jitter to integration times over contours of constant received ranging power in dBmW

shown alongside to facilitate their evaluation. The contours of constant received ranging power are from preliminary design charts produced by Warren Martin[8] to gauge the Mu system performance.

As an example of how this chart may be used, note that the Mu system was operating at the 80-ns level at 1-min integration time and is slightly over the 1-m constraint for 4-h segments (on the average). By referring to the chart, we can determine that had we required an increase in the segment length, we could have continued operating at an acceptable level, as far as jitter is concerned. It is also evident that we could have maintained an acceptable quality of DRVID all the way to −194 dBmW of received ranging power merely by increasing our segment lengths to a full 8 h.

Because of this, it is recommended that future missions maintain an accuracy of 1 m with a power loss less than or equal to −194 dBmW by requiring that the appropriate minimum segment length be provided by the tracking network.

The drift performance cannot be evaluated as easily. The difference between the drift specification and the observed mean values shown in Fig. 19b cannot be interpreted as reflecting on the system performance, since the solar plasma effects have not been verified. This type of analysis will be performed as the postflight analysis of the calibration data progresses. In the meantime, it would not be presumptuous to conclude that, until about day 224 (Fig. 19b), the equipment drift was within the expected range of values. Table 6 lists the average drift and jitter for both systems as a summary of the results.

[8]Warren Martin, private communication, January 26, 1971.

Table 6. DRVID accuracy results

Ranging system	Type	Average jitter, ns	Average drift rate	
			mm/s	ns/12 h
Mu	I	21	0.01	5.8
	II	37	0.005	2.9
	III	70	−0.05	−28.8
	IV	56	0.025	14.4
Tau	I	11	0.005	2.9
	II	8	0.003	1.8
	III			
	IV			

IV. Conclusions

For the MM'71 mission, the DSN committed to provide DRVID data accurate to within the limits of error introduced by the ground system, i.e., 0.75 m. It was understood that the transponder component of the error would be held to 0.75 m so as to complete the total error requirement of 1.0 m desired by the Project. MacDoran's (Ref. 12) statement on the requirements for DRVID applies as much to the MM'71 DRVID as to that proposed for future missions. This statement (see Table 3) left no doubt as to the levels of short-term noise (jitter) and long-term noise (drift) that would have to be achieved if the system was to produce DRVID data of sufficient quality to be of scientific value (1-σ jitter = 27 ns, 1-σ drift = 15 ns).

In Section III-C, we established that, although plasma effects must be investigated further, it was not felt that drift was a problem in either the Tau or the Mu ranging system. The jitter requirements were not met by the Mu system because the data segments were not full passes in length and because the system operating on the 26-m antenna (−195-dB received ranging signal power) was more sensitive to an unexplained power loss (probably the spacecraft transponder) that caused the jitter to be a factor of 2 greater than predicted. (There were no plans

to operate from DSS 12 prior to the beginning of the mission.) Figure 20 indicates that had the received ranging power been that of the 64-m antenna (−175 dB) the jitter would have been on the order of 10 ns, well within the jitter requirements even for short segments (2 h or less).

It is worthwhile at this point to summarize the conclusions on the results of the DRVID demonstration:

(1) The Mu system was well capable of achieving the noise requirements if it had operated on the 64-m antenna and if passes had not been segmented to obtain multiple acquisitions.

(2) The Tau system achieved the requirements when it was not hampered by multiple ranging acquisitions.

(3) The segmentation of DRVID passes in obtaining multiple acquisitions utterly destroyed the value of the calibration information during those passes.

(4) Increased jitter from the Mu ranging was due mainly to some unspecified problem (possibly in the spacecraft transponder) that caused a decrease in signal strength.

(5) When adequate operating conditions were met, DRVID provided accuracy to within 1 m over a pass.

Future missions can ensure themselves of obtaining DRVID of sufficient quality by requiring the following:

(1) The received ranging signal strength must be greater than −194 dBmW and passes must be a full 8 h in length. Integration time should not exceed 15 min in order to permit the detection of trends with periods of 1 h. Figures 12 and 20 should be referred to for other integration times, power levels, and segment lengths.

(2) The drift and jitter requirements specified by MacDoran (Ref. 12) and stated in Table 3 should be allotted to both spacecraft and ground systems.

References

1. MacDoran, P. F., "A First-Principles Derivation of the Differenced Range Versus Integrated Doppler (DRVID) Charged-Particle Calibration Method, in *The Deep Space Network*, Space Programs Summary 37-62, Vol. II, pp. 28–34. Jet Propulsion Laboratory, Pasadena, Calif., Mar. 31, 1970.

2. Efron, L., and Lisowski, R. J., "Charged Particle Effects to Radio Ranging and Doppler Tracking Signals in a Radially Outflowing Solar Wind," in *The Deep Space Network*, Space Programs Summary 37-56, Vol. II, pp. 61–69. Jet Propulsion Laboratory, Pasadena, Calif., Mar. 31, 1969.

3. *Solar-Geophysical Data*, No. 306 ESSA Research Laboratories, Boulder, Colo., Feb. 1970.

4. Mulhall, B. D., *White Paper–Charged Particle Transmission Media for MM71*, IOM 391.3-131, Apr. 28, 1970 (JPL internal document).

5. Hamilton, T. W., and Melbourne, W. G., "Information Content of a Single Pass of Doppler Data from a Distant Spacecraft," in *The Deep Space Network*, Space Programs Summary 37-39, Vol. III, pp. 18–23. Jet Propulsion Laboratory, Pasadena, Calif., May 31, 1966.

6. Mulhall, B. D., "Evaluation of the Charged Particle Calibration to Doppler Data by the Hamilton–Melbourne Filter," in *The Deep Space Network*, Space Programs Summary 37-57, Vol. II, pp. 24–29. Jet Propulsion Laboratory, Pasadena, Calif., May 31, 1969.

7. Mulhall, B. D., Ondrasik, V. J., and Thuleen, K. L., "The Ionosphere," in *Tracking System Analytic Calibration Activities for the Mariner Mars 1969 Mission*, Technical Report 32-1499, pp. 45–68. Jet Propulsion Laboratory, Pasadena, Calif., Nov. 15, 1970.

8. Mulhall, B. D., and Wimberly, R. N., "Comparison of Ionospheric Measurements for Evaluation of Techniques Used in Charged Particle Calibration of Radio Tracking Data, Preliminary Results," in *The Deep Space Network*, Space Programs Summary 37-56, Vol. II, pp. 58–61. Jet Propulsion Laboratory, Pasadena, Calif., Mar. 31, 1969.

9. Miller, L. F., and Mulhall, B. D., "Comparison of Faraday Rotation Measurements of the Ionosphere," in *The Deep Space Network Progress Report*, Technical Report 32-1526, Vol. V, pp. 58–65. Jet Propulsion Laboratory, Pasadena, Calif., Oct. 15, 1971.

10. von Roos, O. H., and Mulhall, B. D., *An Evaluation of Charged Particle Calibration by a Two-Way Dual Frequency Technique and Alternatives to this Technique*, TM 391-271, Jan. 13, 1972 (JPL internal document).

11. MacDoran, P. F., and Martin, W. L., "DRVID Charged-Particle Measurement With a Binary-Coded Sequential Acquisition Ranging System," in *The Deep Space Network*, Space Programs Summary 37-62, Vol. II, pp. 34–41. Jet Propulsion Laboratory, Pasadena, Calif., Mar. 31, 1970.

12. MacDoran, P. F., *DRVID Requirements and Their Rationale for the Viking Mission*, IOM 391.3-385, June 1971 (JPL internal document).

The Tropospheric Calibration Model for Mariner Mars 1971

C. C. Chao

I. Tropospheric Effect on Radio Signals

When a radio wave is propagating through the troposphere (neutral atmosphere), it experiences velocity retardation as well as an angular deflection. The distance traversed by a radio signal in the troposphere is given by the integral

$$\int_{\text{path}} n\, ds$$

where n is the refractive index of the troposphere and is defined as the ratio of the speed of propagation in a medium over the speed of light in vacuum. For a spherically symmetric atmosphere, n is a function of altitude alone.

The delay in the arrival time of a radio signal passing through the troposphere directly affects the range and range rate measurements from a spacecraft. This will result in a range increase varying from 2 m at zenith to approximately 100 m at the horizon. In order to meet the MM'71 mission objectives for tropospheric calibration below the meter level, an accurate tropospheric calibration model, which includes seasonal variation effects, was developed.

A summary of typical tropospheric effects on the tracking observables at various elevations and apparent location changes in the tracking station is given in Table 1. A comparison was made of the effects before and after calibration. Without calibration, a 16-m change in the distance off the spin axis, r_s, is induced for a 10-deg minimum elevation symmetrical pass. Even after calibration with the old model, the error in r_s is still greater than 1 m (see Table 1).

The estimated uncertainties of the new model at various elevation angles are also shown in Table 1. It has met the required accuracy of the MM'71 mission. Areas for future improvement of this model are indicated in Fig. 1. Shown are cursory estimates of the relative contributions from various error sources to the uncertainty of the calibration.

Table 1. Errors due to tropospheric refraction before and after calibrations

Minimum elevation angle, deg	Calibration model	Range residuals, m	Range rate residuals ($\delta = 0°$), mm/s	Errors in station spin axis distance,[a] m
5	No model	23	15.1	30
	Old model	3.3	2.5	4.5
	New model	0.55	0.5	1.0
10	No model	12.5	4.7	16
	Old model	1.6	0.7	2.4
	New model	0.25	0.13	0.5
20	No model	6.0	1.2	7.4
	Old model	0.9	0.18	1.0
	New model	0.15	0.04	0.2

[a]Symmetrical pass over Goldstone station for $\delta = -10$ deg.

II. Seasonal Fluctuations in the Troposphere

In the past, tropospheric refraction was calibrated with a model which was independent of time. This neglected the possible temporal fluctuations in the refractivity of the troposphere. A recent study of one year's radiosonde balloon data by Ondrasik and Thuleen (Ref. 1) indicated that the tropospheric zenith range effect has a variation of about $\pm 5\%$ of its yearly average. According to Ref. 2, the 5% uncertainty in zenith range effect can increase to between 6 and 8% uncertainty at low elevation angles due to possible variations in the refractivity profile. An 8% uncertainty in range effect corresponds to more than 1 m in the overall uncertainty in range correction over the whole pass, which exceeds the requirement of the MM'71 mission ($\sigma\Delta\rho$/pass = 1 m, minimum elevation = 6 deg). When the two-station tracking or very long baseline interferometry (VLBI) techniques are employed, the low elevation angle data will become more important, since these long baselines generally result in data being obtained at low elevation angles (Ref. 3). The required uncertainty in range correction over one pass by VLBI is below 1 m, an objective which cannot be met unless the calibrations include corrections for seasonal fluctuations in refractivity of the troposphere.

In order to meet these needs, a new model of tropospheric calibration was developed as a result of the following investigations:

(1) Examination of the seasonal variations in the refractivity profiles based on 2 years' radiosonde balloon measurement taken at six weather stations near five of the DSN stations.

(2) Comparison of the exponential model that has long been used with the measured profile of refractivity, and the derivation of an analytic expression which can more closely represent the actual dry refractivity profile than the exponential function does.

(3) Estimation of uncertainties of range effect due to the seasonal fluctuations in refractivity profiles found in (1). Examination of the improvement that can be obtained by using the monthly mean profiles.

The refractivity of the troposphere at a given altitude is commonly determined from the following equation (Ref. 4):

$$N = \frac{77.6}{T}\left(P + \frac{4810e}{T}\right) \tag{1}$$

where

P = pressure, mbar (1 mbar = 10^2 N/m^2)

T = temperature, K

e = vapor pressure, mbar

and

$$e = 6.1\,(RH/100)\,\exp_{10}\,[7.4475T_c/(234.7 + T_c)]$$

where

RH = relative humidity, %

T_c = temperature, °C

$\exp_{10} y = 10^y$

The particular constants in Eq. (1) given by Smith and Weintraub (Ref. 5) are considered to be good to 0.5% in

Table 3. Radiosonde balloon site parameters

Radiosonde station	Elevation, m	Distance from nearest DSS, km	Nearest DSS	DSS elevation, m
Edwards AFB	724	100	Goldstone DSCC	1032
Yucca Flats	1190	200	Goldstone DSCC	1032
Madrid	606	70	Madrid DSCC	789
Wagga	214	140	Tidbinbilla DSCC	656
Woomera	165	12	Woomera	151
Pretoria	1330	50	Johannesburg	1398

1. Dry refractivity profiles. About 90% of the total refractivity N is due to the dry component in the first 7 km (23,000 ft). From there upward, the wet component diminishes and the dry part becomes the total refractivity. From Eq. (1), we can express the dry component refractivity as

$$N_D = 77.6 \frac{P}{T} \tag{2}$$

The variations in N_D that resulted from the fluctuations in pressure P and temperature T in the troposphere were investigated using the radiosonde balloon measurements taken at six weather stations. The standard deviations of the dry refractivity, σ_{dry}, from the monthly mean at Edwards Air Force Base, California, were calculated and tabulated in Table 4. The results indicate that N_D has greater deviations at low altitudes. For altitudes above 10 km, most of the deviations of N_D are less than 2 N-units. For altitudes below 10 km, the change in N_D is around 5 N-units or 2–3% of the total refractivity N. Thus the shape of the dry refractivity profile remains fairly unchanged. The variations of the monthly mean of N_D at various altitudes are also shown in Table 4. The fluctuation in N_D below 7 km (23,000 ft) is caused by the daily and

Table 4. Monthly mean and standard deviation of dry refractivity at various altitudes above Edwards Air Force Base

Month	Dry refractivity, mean (1 σ)								
	Surface 0.72 km (2375 ft)	3.66 km (12,000 ft)	6.70 km (22,000 ft)	9.75 km (32,000 ft)	12.8 km (42,000 ft)	15.8 km (52,000 ft)	18.9 km (62,000 ft)	25.0 km (82,000 ft)	31.1 km (102,000 ft)
Jan	262.4 (6.18)	187.9 (2.83)	136.9 (1.20)	97.3 (1.41)	63.6 (2.56)	40.1 (1.77)	24.4 (0.98)	8.8 (0.18)	3.2 (0.15)
Feb	260.4 (3.86)	188.4 (1.85)	136.8 (0.81)	96.9 (1.96)	62.3 (1.78)	39.5 (1.03)	24.2 (0.38)	8.8 (0.08)	3.2 (0.05)
Mar	255.8 (5.52)	187.2 (1.70)	136.1 (0.96)	96.9 (1.42)	62.7 (1.98)	39.4 (0.92)	24.0 (0.42)	8.6 (1.65)	3.3 (0.69)
Apr	254.6 (4.57)	186.5 (1.63)	135.8 (1.26)	96.3 (1.65)	63.4 (1.86)	39.6 (0.83)	24.3 (0.42)	8.9 (0.07)	3.1 (0.79)
May	249.7 (7.37)	185.3 (3.90)	135.5 (2.42)	96.7 (2.06)	64.0 (2.42)	39.8 (1.24)	24.4 (0.79)	9.0 (0.24)	3.5 (0.09)
June	246.1 (2.87)	183.9 (1.90)	135.2 (1.27)	96.2 (2.15)	65.3 (1.71)	42.1 (1.39)	25.0 (0.82)	9.3 (0.30)	3.6 (0.16)
July	243.2 (1.97)	182.2 (0.92)	134.3 (0.60)	95.5 (4.65)	67.3 (2.18)	44.6 (2.47)	26.2 (3.20)	9.6 (1.06)	3.7 (0.38)
Aug	241.1 (3.78)	182.3 (0.84)	134.5 (0.56)	93.4 (0.78)	64.8 (1.21)	40.6 (0.95)	22.0 (0.64)	7.7 (1.37)	2.8 (0.66)
Sept	246.7 (2.43)	184.3 (1.26)	133.9 (0.69)	96.6 (0.55)	65.9 (1.39)	42.7 (0.68)	25.4 (0.15)	8.7 (2.58)	3.4 (0.78)
Oct	252.5 (5.50)	184.6 (1.68)	135.1 (1.16)	97.2 (0.57)	65.3 (1.17)	41.1 (0.75)	24.7 (0.31)	8.7 (1.85)	3.2 (0.90)
Nov	255.0 (5.98)	184.4 (3.38)	134.9 (1.08)	96.9 (1.82)	65.9 (1.91)	41.2 (1.05)	24.6 (0.33)	8.9 (0.09)	3.1 (0.90)
Dec	261.0 (4.56)	187.9 (1.84)	136.4 (0.98)	96.5 (1.39)	63.7 (1.97)	39.6 (0.70)	24.1 (0.32)	8.8 (0.06)	3.3 (0.04)

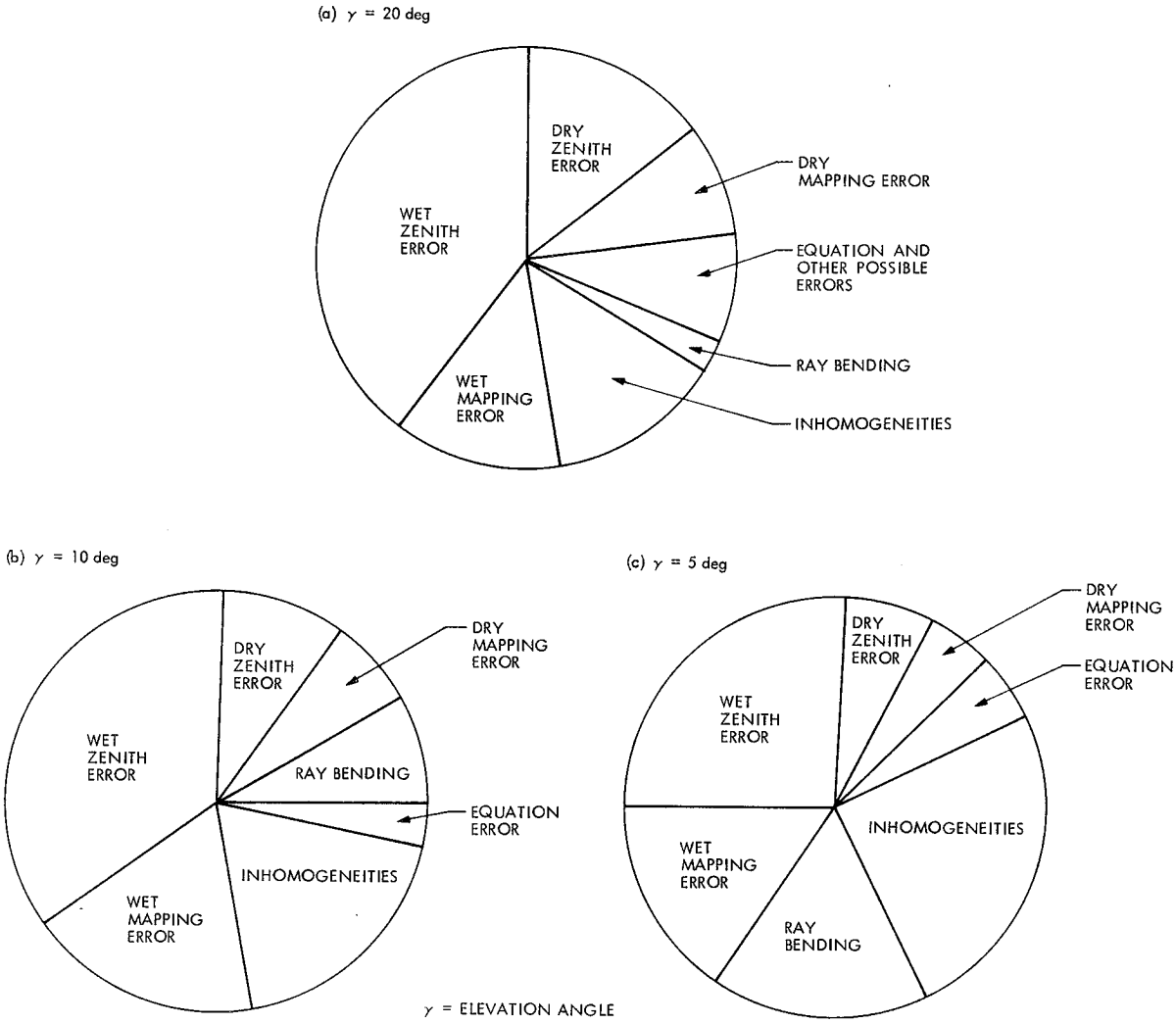

Fig. 1. Estimated relative contributions from various error sources to the uncertainty of the new calibration model

N for frequencies up to 30,000 MHz and normally encountered ranges of pressure, temperature, and humidity.

The values of P, T, and RH are measured data at a given altitude from the radiosonde balloon. An approximation to the errors in N resulting from the use of Eq. (1) due both to the errors in the equation itself and to errors in the meteorological measurements is given by Bean and Dutton (Ref. 4) as shown in Table 2.

The first and second terms of Eq. (1) will be referred to as the dry and wet refractivity, N_D and N_W, respectively.

Because of the seasonal or daily variations of the parameters in Eq. (1), P, T, and RH, the values of N above a station also exhibit seasonal variations. The values of dry and wet refractivity, N_D and N_W, were calculated from the radiosonde balloon measurements taken at the six stations (Table 3). A separate examination of the dry and wet refractivity profiles was conducted.

Table 2. Errors in refractivity N

Error Sources	Ratio of rms error in refractivity to refractivity[a]	
Equation (1)	0.5%	(1.6)[b]
Surface observations (± 1 mbar, ± 0.1°C, $\pm 1\%$ RH)	0.2%	(0.65)
Radiosonde observations (± 2 mbar, ± 1°C, $\pm 5\%$ RH)	1.3%	(4.2)

[a] P = 1013 mbar, T_c = 15°C, RH = 60% (1 mbar = 10^2 N/m^2).
[b] Terms in parentheses are ΔN.

$$N_D = \frac{77.6}{T_m} P_m \exp\left[-\frac{g}{RT_m}(h - h_m)\right]$$

$$= N_{D_m} \exp\left[-\frac{g}{RT_m}(h - h_m)\right] \qquad (10)$$

where

N_{D_0} = dry surface refractivity

N_{D_m} = dry refractivity at r_m

The profile in the first 10 km follows a polynomial of power $a - 1$, while that in the next 20 km decays exponentially under an approximately isothermal condition. The average value of $a - 1$, based on the mean temperature profiles shown in Fig. 2, is about 4. This explains why a quartic profile, as suggested by Hopfield (Ref. 6), has closer agreement with the data than a simple exponential profile does in the first 12.2 km (40,000 ft) (Fig. 3). The quartic model deviates by an appreciable amount when it is higher than 15.2 km (50,000 ft), whereas a second-stage exponential model works nicely, as shown in Fig. 4.

2. Wet refractivity profiles. As indicated in Ref. 1, the dominant error source in the zenith range tropospheric correction computed from radiosonde data comes from the variations in the wet component of refractivity N_W, the equation for which can be rewritten in the following way:

$$N_W = 3.733 \times 10^5 \frac{e}{T^2} \qquad (11)$$

or

$$N_W = 2.277 \times 10^4 \frac{RH}{T^2} \exp_{10}\left[\frac{7.4475T_e}{234.7 + T_e}\right] \qquad (12)$$

According to the balloon data, the wet refractivity profiles are confined within the first 6.1 to 7.6 km (20,000 to 25,000 ft) of altitude where most of the water vapor in the atmosphere is contained. The temperature and relative humidity for a particular area are known to have both daily and seasonal variations; thus the wet refractivity N_W computed from Eq. (12) should also have two types of variations, as discussed below.

a. Short-term (daily) fluctuations. The actual daily fluctuations in the wet component N_W can be found from the computed data from radiosonde balloon measurements.

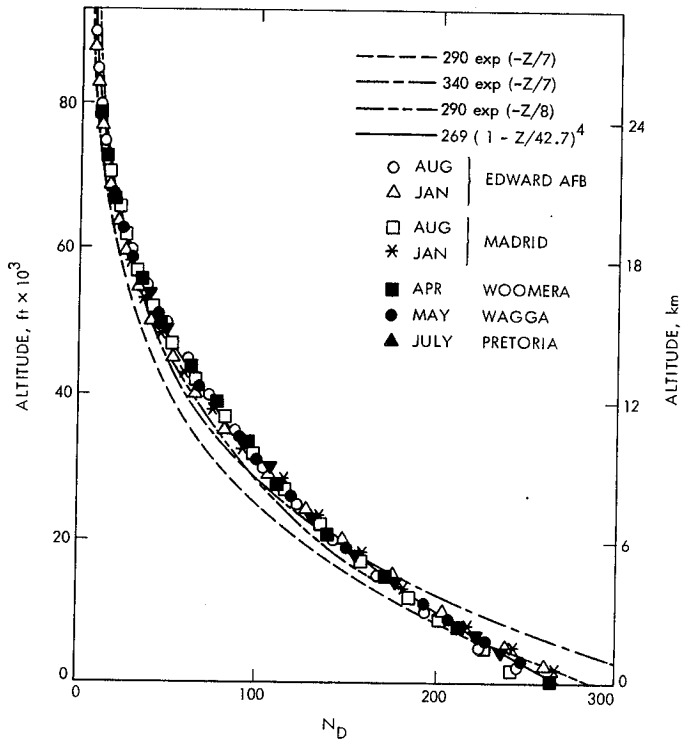

Fig. 3. Dry refractivity profiles

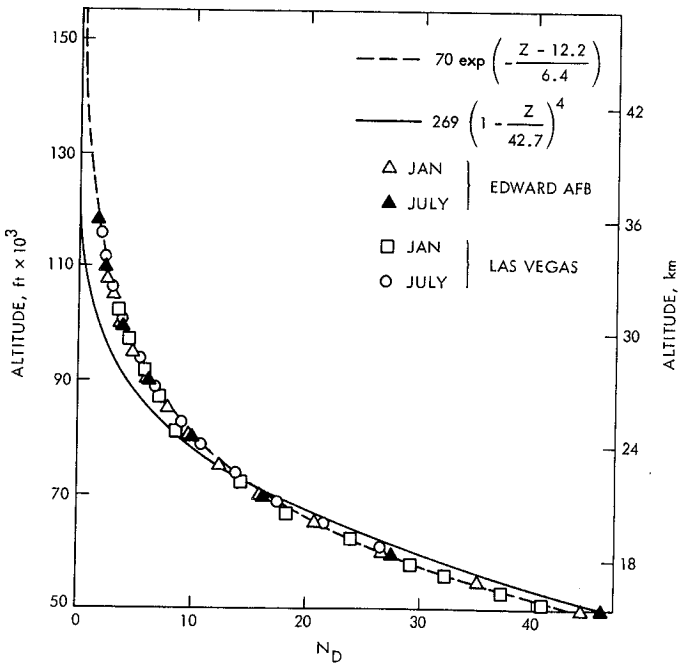

Fig. 4. Dry refractivity profiles for altitudes higher than 15.3 km (50,000 ft)

seasonal variations in pressure and temperature resulting from local weather changes. As will be shown later, the magnitude of these low-altitude fluctuations is less than the magnitude of the fluctuations of the wet component. Since the shape of the profile of the dry component is relatively steady in most portions of the troposphere, an analytic expression for mapping the range effect down to lower elevation angles may be derived.

If we assume the atmosphere is in static equilibrium, is spherically symmetrical, and obeys the perfect gas law, then we can write the governing equations for the dry part as

$$-\rho g = \frac{dP}{dr} \tag{3}$$

$$P = \rho RT \tag{4}$$

where P, ρ, and T are functions of r only, and where

ρ = density of air

P = pressure

T = absolute temperature

r = geocentric distance

R = gas content

g = gravitational acceleration

The temperature profile $T(r)$ in the atmosphere depends on the thermal property of the atmosphere and the heat balance of the earth. According to the measured data from the U.S. Standard Atmosphere Supplements (1966), the temperature profiles in the troposphere can be classified as linearly decreasing up to about 10 km and then remaining fairly constant up to 30 km (Fig. 2):

$$T \cong T_0 - \gamma(r - r_0), \qquad r_0 < r < r_m \tag{5}$$

$$T \cong T_m, \qquad r_m < r < r_{\text{tropo}} \tag{6}$$

where

γ = temperature lapse rate

r_0 = surface altitude

r_m = altitude where temperature becomes constant with altitude

r_{tropo} = outer edge of troposphere (about 40 km)

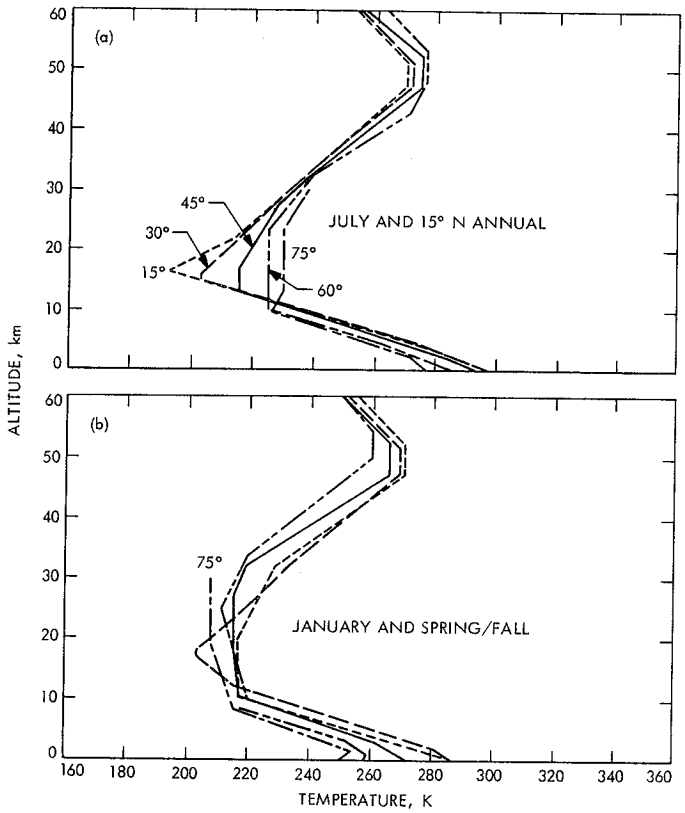

Fig. 2. Temperature–altitude profiles of the 30, 45, 60, and 75 deg N (a) July and 15 deg N mean annual Supplementary Atmospheres, (b) January and midlatitude spring/fall Supplementary Atmospheres (from the U.S. Standard Atmosphere Supplements, 1966)

If we assume that these conditions exist, then we can combine Eqs. (3), (4), (5), and (6) and integrate to get

$$P = P_0\left(1 - \frac{\gamma h}{T_0}\right)^a \tag{7}$$

$$P = P_m \exp\left[-\frac{g}{RT_m}(h - h_m)\right] \tag{8}$$

where $a = g/\gamma R$; $h = r - r_0$; P_m, T_m are the values of P and T at r_m; and P_0, T_0 are conditions at r_0. Substituting Eqs. (7) and (8) into the dry part of Eq. (1), we obtain the expression for dry refractivity profile:

$$N_D = \frac{77.6}{T}P = 77.6\frac{P_0\left(1 - \frac{\gamma h}{T_0}\right)^a}{T_0\left(1 - \frac{\gamma h}{T_0}\right)}$$

$$= N_{D0}\left(1 = \frac{\gamma h}{T_0}\right)^{a-1} \tag{9}$$

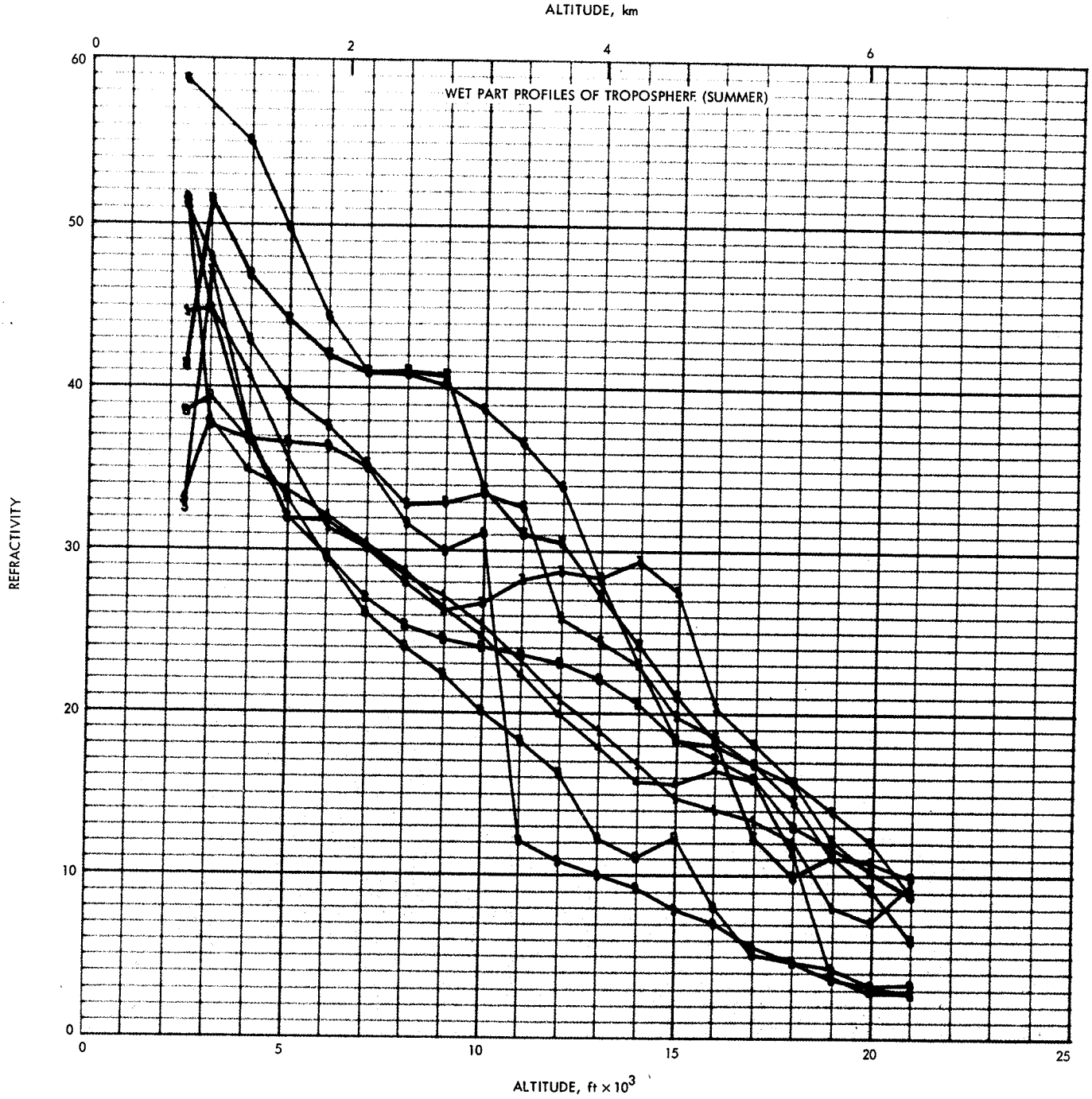

Fig. 6. Wet refractivity profiles for Edwards AFB in July 1967

b. Long-term (seasonal) fluctuations. The monthly mean of the wet refractivity profiles for stations at Edwards Air Force Base and Madrid is plotted in Figs. 7 and 8. The seasonal variations can be easily seen from those monthly mean profiles. The summer-type profiles are consistently the highest of the year, while the winter-type profiles are the lowest. The magnitude of the total variation in a year and the shape of the average profiles vary from station to station due to the particular local weather variation. For instance, the magnitude of variations at Edwards Air Force Base is greater than that at Madrid, and the former has a peculiar type of profile in

Figures 5 and 6 show the profiles of N_W above a meteorological station for the first 6.1 km (20,000 ft), where N_W is significant. Due to the limitation of space, only the summer and winter types of profiles are shown in these figures.

The three stations in the northern hemisphere, Edwards Air Force Base in California, Yucca Flats in Nevada, and Madrid in Spain, have very different types of profiles between summer and winter. About 10 days' data in January, plotted in Fig. 5, reveals the average low profiles and lesser daily fluctuations in winter, while the corresponding plot (Fig. 6) shows that the summer weather makes the wet component of refractivity very active and fluctuating. The profiles in the rest of the year fall between these two types of profiles, and they will be seen on the monthly mean profiles later.

The other three stations, in the southern hemisphere (Woomera and Wagga in Australia and Pretoria in South Africa), show similar characteristics in the summer and winter type of profiles except that the fluctuations in winter (June–August) are more active than those of the northern hemisphere stations.

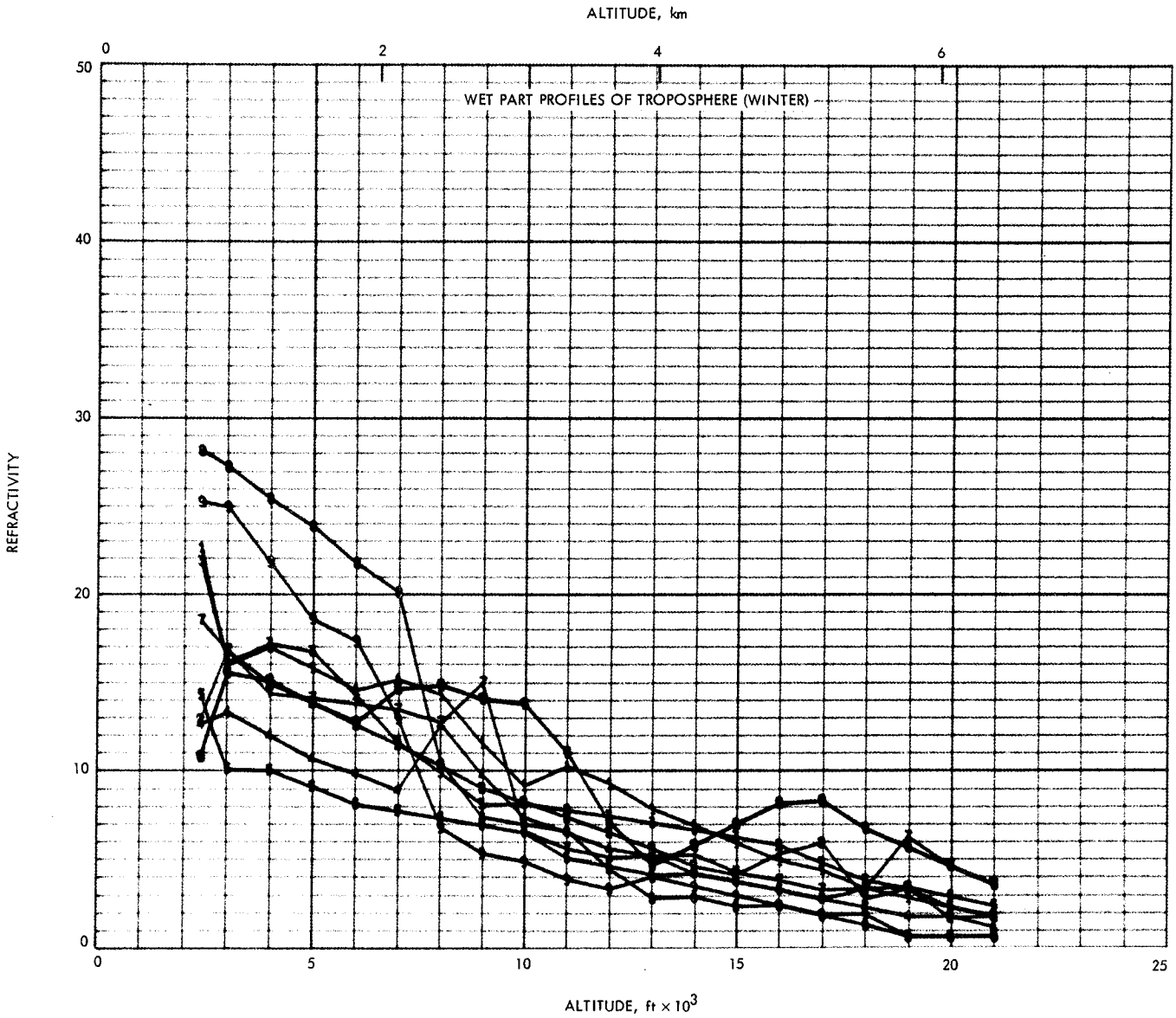

Fig. 5. Wet refractivity profiles for Edwards AFB in January 1967

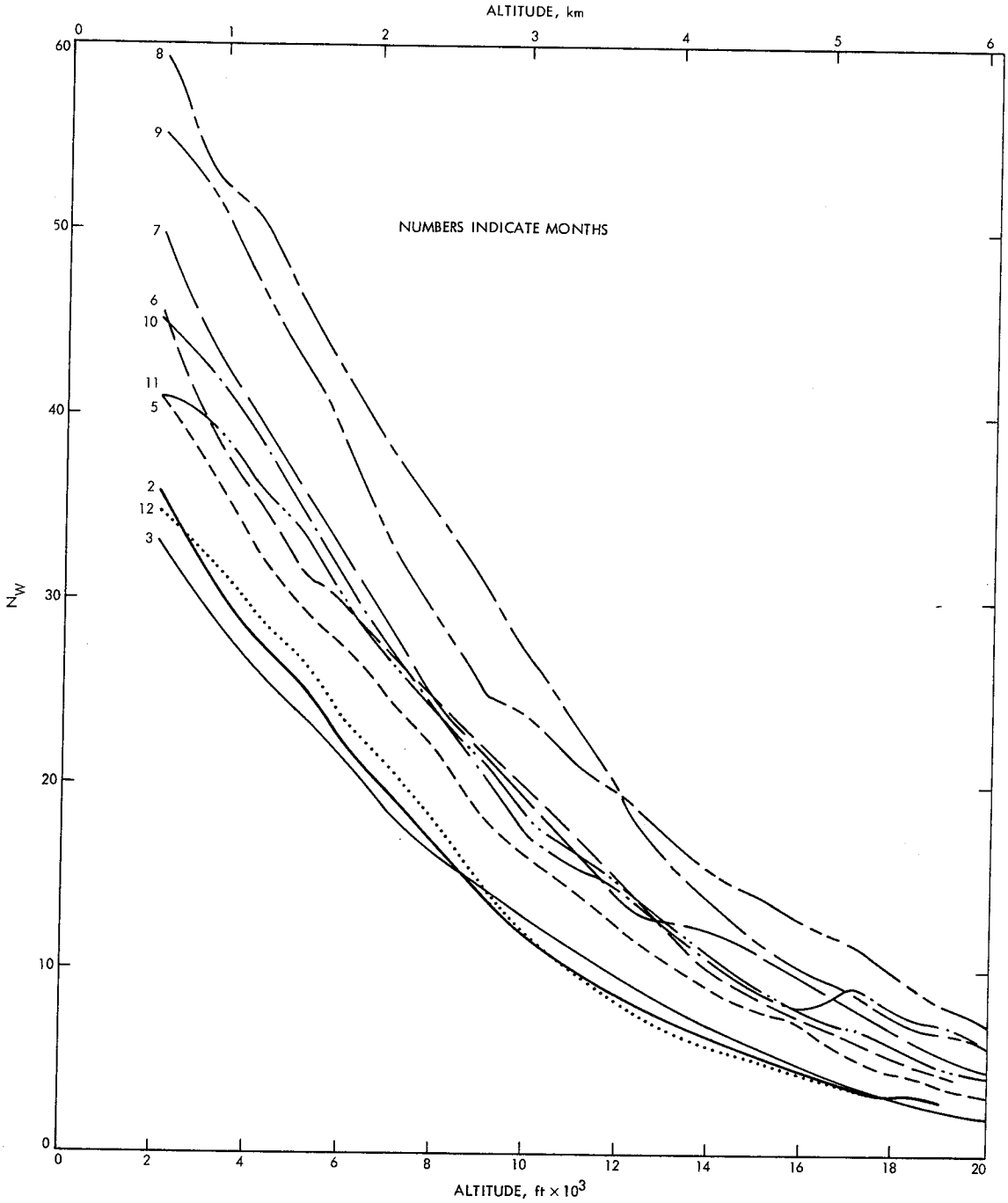

Fig. 8. Monthly mean profiles of wet refractivity, Madrid

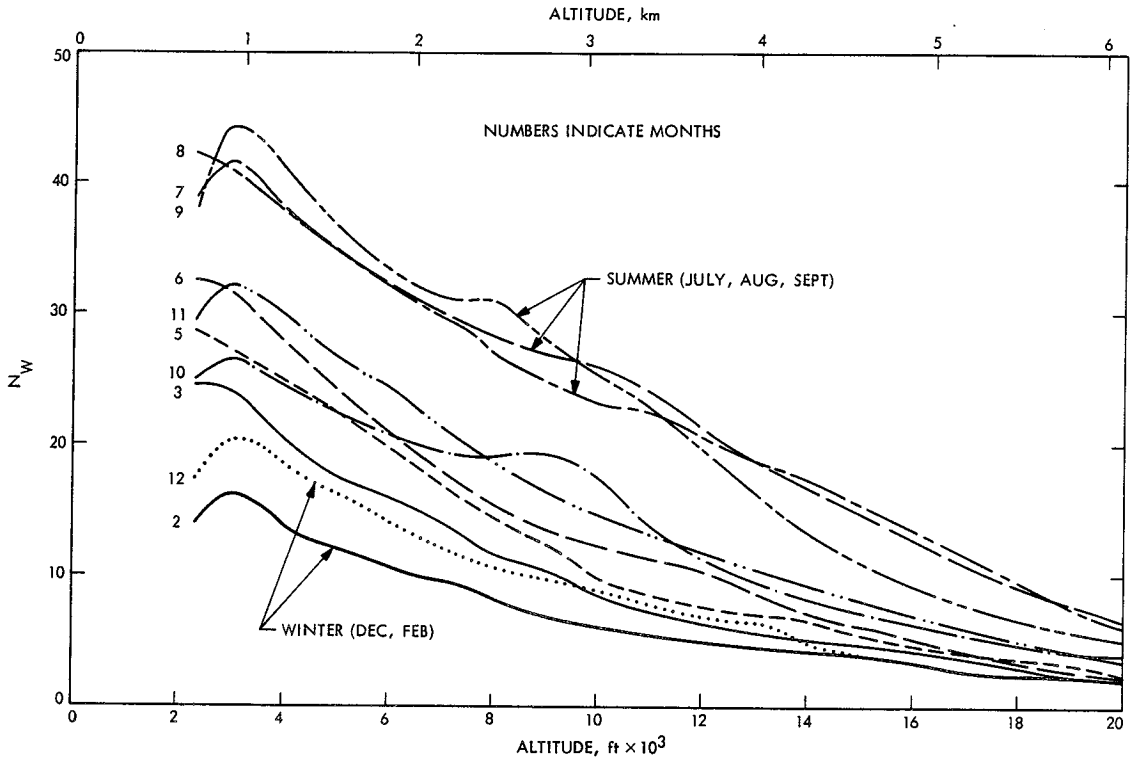

Fig. 7. Monthly mean profiles of wet refractivity, Edwards AFB

the low altitude, where a maximum usually occurs at a height of about 0.35 km (1000 ft) above the surface. It should be noted that the magnitudes of short-term fluctuations in winter, spring, and fall are generally several times smaller than those of the long-term fluctuations. In the summer, the short-term fluctuation becomes so active that it is almost equal to the long-term fluctuation in magnitude. The range of standard deviations from the monthly mean is shown in Table 5. It has higher deviations than the dry part.

It is also important to examine the repeatability of the seasonal variation at each station. Thuleen and Ondrasik (Ref. 7) recently made a comparison of the 2-year zenith range effects at the six weather stations, and the results showed good repeatability of the seasonal variations at each station. The results of this analysis also indicate that the seasonal variations in the shape of both dry and wet profiles repeat quite well based on 1967 and 1968 data. Figures 5 and 6 and Figs. 9 and 10 give a sample of wet refractivity profiles in the same months of the two years. Their agreement is generally good. The differences between the 1967 and 1968 data are of the same magnitude as that of the short-term fluctuations. This gives us confidence that a new calibration model with seasonal adjustment can significantly reduce the uncertainties in range and range rate calibrations caused by seasonal fluctuations.

Table 5. Summary of uncertainties (1σ) from monthly mean of wet refractivity at various altitudes for the six stations

Season	Surface	1.83 km (6000 ft)	3.66 km (12,000 ft)	7.32 km (24,000 ft)
Summer months	10 to 17	7 to 10	5 to 8	0.5 to 1.5
Winter months	4.5 to 9	3.5 to 7.5	2.5 to 6	<0.5

c. Uncertainty of range effect due to seasonal fluctuations at various elevation angles. The range and range rate corrections for the troposphere are derived directly from the profiles of refractivity obtained from radiosonde balloon measurement. Table 6 shows the average uncertainties ($1\ \sigma$) in range correction at various elevation angles of a fixed calibration model (2-year mean) and a seasonally adjusted model (monthly mean). Values in Table 6 were computed by a ray trace program (Ref. 2).

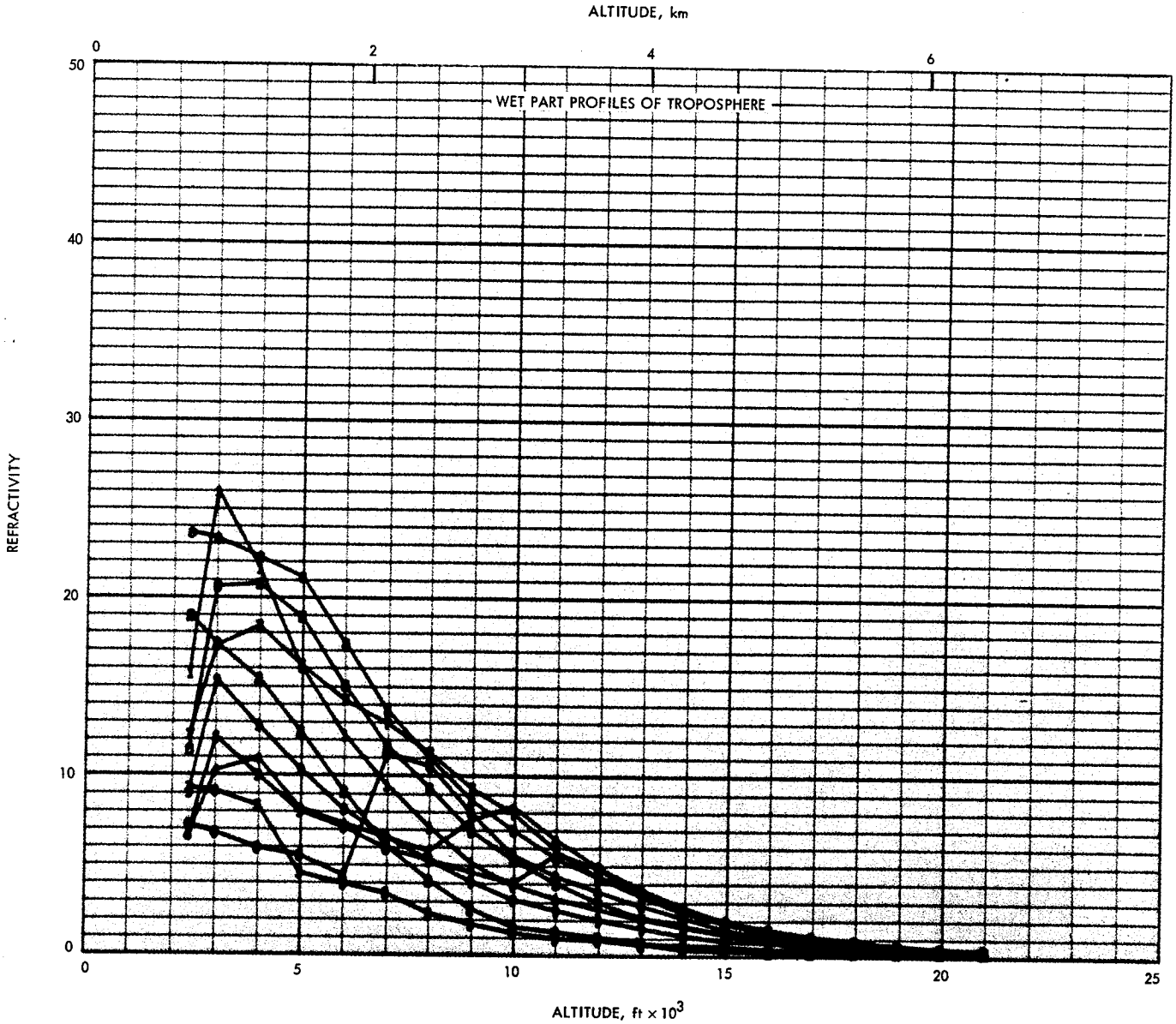

Fig. 10. Wet refractivity profiles for Edwards AFB in July 1968

It is seen that the fixed model based on the 2-year mean profile at each station has an uncertainty of about 0.11 m (5%) at zenith and 1.6 m (6.5%) at 5 deg of elevation angle. When the monthly mean profiles are used, the uncertainty in the range correction is reduced by almost a factor of 3. The greatest part of the uncertainty is due to the fluctuations in the wet component. The values at zenith, as shown in Table 6, seem to agree with the results in Ref. 1.

III. The Current TSAC Calibration Technique

A. Prediction From Surface Measurement

It is expected that frequent radiosonde balloon measurements will reduce the uncertainty due to temporal fluctuations. However, it is not practically possible to take balloon measurements as frequently as one desires, say, once every hour. Thus a method for predicting the profiles and zenith range effect through surface measure-

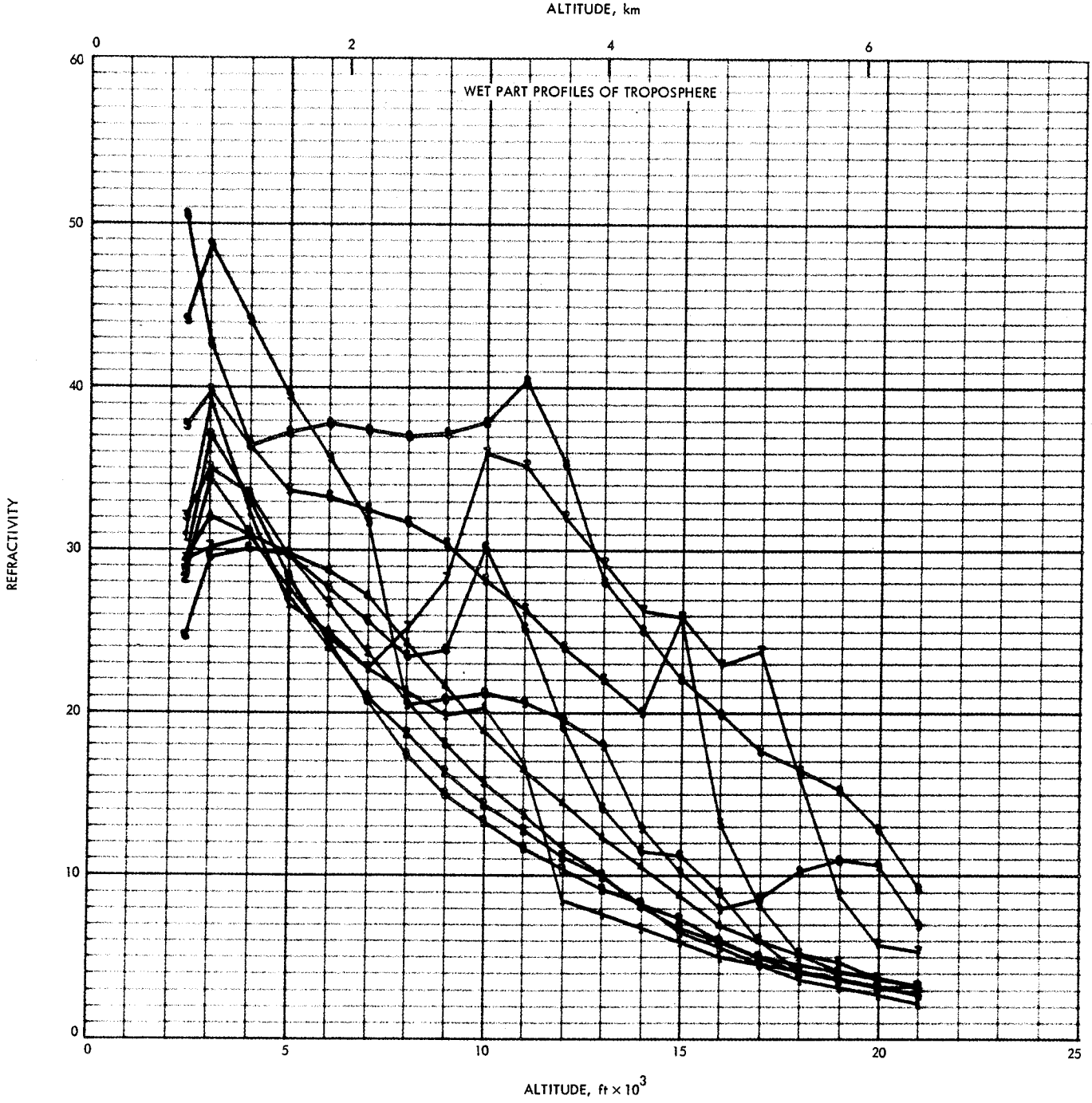

Fig. 9. Wet refractivity profiles for Edwards AFB in January 1968

with monthly means of the four parameters (P_0, $(RH)_0$, γ, and T_0) obtained from 2 years (1967 and 1968) of radiosonde balloon measurements taken near the deep space stations (Ref. 10). To overcome the inadequacy of Eq. (14) for the possible variations of RH with altitude, the monthly means of $(RH)_0$ were averaged over each month. The values of the monthly means calculated from the 2-year data are tabulated in the Tables 7–11 for those deep space stations (DSSs 11, 12, 13, 14, 41, 42, 61, 62, 51).

Table 7. Averaged surface weather parameters for DSSs 12 and 14 (11,[a] 13[b])

Month	Pressure, mbar (10^2 N/m^2)	Temperature, °C	Relative humidity, %	Lapse rate, °C/km
1	906.72	20.08	19.30	6.20
2	906.66	18.12	27.83	6.74
3	902.70	16.18	27.48	6.53
4	900.03	16.16	25.04	6.08
5	898.66	20.78	29.78	7.01
6	895.46	22.96	30.70	6.40
7	900.91	30.50	33.12	7.11
8	900.54	31.60	35.61	7.53
9	899.64	23.41	43.84	6.25
10	904.38	27.96	21.29	6.23
11	903.62	19.28	28.14	6.00
12	902.58	12.54	30.26	6.18

[a]Corrections to DSS 11: pressure −1.8 mbar; temperature −0.1°C.
[b]Corrections to DSS 13: pressure −8.7 mbar; temperature −0.6°C.

Table 8. Averaged surface weather parameters for DSSs 61 and 62

Month	Pressure, mbar (10^2 N/m^2)	Temperature, °C	Relative humidity, %	Lapse rate, °C/km
1	931.37	12.14	52.67	6.66
2	928.26	12.14	62.45	6.60
3	926.73	16.05	50.92	6.53
4	923.12	13.97	67.05	6.72
5	924.43	15.09	60.73	5.84
6	927.58	20.08	52.80	6.25
7	926.55	27.13	39.27	6.55
8	925.93	24.13	48.57	6.23
9	926.18	21.05	57.18	6.01
10	927.74	19.07	57.38	5.95
11	925.67	13.92	74.04	6.04
12	929.24	11.42	60.41	6.09

Table 9. Averaged surface weather parameters for DSS 41

Month	Pressure, mbar (10^2 N/m^2)	Temperature, °C	Relative humidity, %	Lapse rate, °C/km
1	992.46	34.94	28.39	7.26
2	994.72	28.68	30.29	5.79
3	1003.85	21.44	45.55	5.59
4	1001.52	28.66	36.21	7.10
5	1003.90	18.92	47.09	5.86
6	1005.05	20.13	42.01	6.28
7	1000.80	13.70	53.16	5.50
8	936.61	14.00	46.22	5.21
9	1001.92	18.68	34.18	5.61
10	1000.70	21.37	31.37	5.75
11	997.60	19.70	36.62	5.36
12	996.81	24.97	36.69	6.14

Table 10. Averaged surface weather parameters for DSS 42

Month	Pressure, mbar (10^2 N/m^2)	Temperature, °C	Relative humidity, %	Lapse rate, °C/km
1	946.50	22.24	46.39	5.59
2	950.80	23.24	37.79	5.69
3	948.60	20.99	39.87	5.71
4	943.50	15.29	47.96	5.25
5	949.60	12.21	55.23	5.51
6	951.20	14.22	46.89	6.14
7	952.40	10.42	62.16	6.00
8	944.50	9.52	76.16	6.30
9	951.40	13.22	63.95	6.29
10	949.20	16.10	54.92	6.01
11	945.10	17.22	50.61	5.56
12	946.00	20.20	53.62	6.34

C. Standard Mapping Tables for Both Dry and Wet Components

Once the zenith range correction is carefully determined, the next step is to map it down to lower elevation angles by employing a correct refractivity profile.

A cursory examination of the sensitivity of the tropospheric range effect to the shape of the refractivity profile has been made in Ref. 2. It indicates that for a slight variation in the refractivity profile, the effect on the ratio

Table 6. Uncertainties in tropospheric zenith range correction (one-way) based on the two-year radiosonde balloon data (in meters)

γ, deg	$\sigma\Delta\rho_{dry}$		$\sigma\Delta\rho_{wet}$		$\sigma\Delta\rho_{total}$	
	Fixed N[a]	Variable N[b]	Fixed N[a]	Variable N[b]	Fixed N[a]	Variable N[b]
1	1.502	0.711	6.00	2.055	6.20	2.175
3	0.609	0.326	2.581	0.810	2.680	0.875
5	0.321	0.157	1.543	0.521	1.585	0.545
15	0.101	0.048	0.433	0.148	0.453	0.154
45	0.038	0.017	0.152	0.051	0.160	0.055
90	0.026	0.012	0.105	0.036	0.109	0.038

[a]Fixed N based on 2-year average of surface weather data.
[b]Variable N based on monthly average of surface weather data.

ments that can be taken frequently or even continuously becomes very helpful.

Recently, Berman (Ref. 8) derived a set of formulas which can predict the dry and wet component of the zenith range effect from ground surface measurement:

$$\Delta\rho_{z_{dry}} = 2.276\, P_0 \tag{13}$$

$$\Delta\rho_{z_{wet}} = 0.566\,\frac{(RH)}{\gamma}\left(1-\frac{c}{T_0}\right)^2 \exp\left(\frac{AT_0 - B}{T_0 - C}\right) \tag{14}$$

where

$\Delta\rho_z$ = zenith range correction, m

P_0 = surface pressure, bar (1 bar = 10^5 N/m^2)

γ = temperature lapse rate, K/km

T_0 = linearly extrapolated surface temperature, K

$(RH)_0$ = surface relative humidity ($0 \leq (RH)_0 \leq 1$)

A = 17.1486

B = 4684.1331

C = 38.45

Equation (13) is obtained under the assumption of static equilibrium, perfect gas of the troposphere, and constant gravitation acceleration g. If these assumptions are true, Eq. (13) has the potential to predict the dry zenith range effect with an uncertainty of ±2 mm for a precision of ±1 mbar in surface pressure measurement (Ref. 9). According to Ref. 8, the uncertainty of the wet zenith range effect computed from Eq. (14) is 2.8 cm (1 σ). Thus the total zenith range effect can be predicted from surface measurement with an accuracy approaching that obtained from radiosonde measurements.[1] Two of the four parameters, P_0 and $(RH)_0$, can be measured continuously at each tracking station; for example, the microbarograph measures surface pressure continuously.

The temperature lapse rate γ and T_0 can be estimated from less frequent (perhaps every several days, or monthly mean) radiosonde measurement. Another advantage of Eq. (13) is that it gives the dry zenith range effect of the entire troposphere, while most of the radiosonde balloon data end at about 24.4 km (80,000 ft), and the contribution due to the rest of the troposphere has to be estimated. Besides, the balloon, instead of ascending along the zenith direction, may fly along a 30- to 45-deg elevation, due to the local wind. Equation (14) is derived under the assumption of constant RH. When RH varies drastically with altitude, the wet zenith range effect should be obtained directly from radiosonde measurement.

B. Computed Monthly Mean From Two-Year Radiosonde Measurement

It has been shown that the seasonal variations of the refractivity profiles at each station repeat satisfactorily over a 2-year period. The tropospheric calibration for the MM'71 mission was made by using Eqs. (13) and (14),

[1]Later comparisons of the wet component estimate (as expressed in Eq. 14) with the radiosonde balloon results showed that errors as large as 5 cm can occur. However, a great part of this discrepancy can be attributed to the fact that the assumption of a constant relative humidity at all altitudes is generally not true.

Table 11. Averaged surface weather parameters for DSS 51

Month	Pressure, mbar (10^2 N/m^2)	Temperature, °C	Relative humidity, %	Lapse rate, °C/km
1	855.74	22.11	47.06	4.82
2	859.30	22.72	49.39	6.07
3	857.35	18.71	54.65	5.63
4	856.01	21.53	42.52	6.30
5	860.60	18.02	39.61	5.84
6	864.11	15.45	33.49	5.55
7	863.10	19.25	30.79	6.56
8	863.82	20.70	39.24	6.89
9	862.40	18.75	49.30	4.93
10	858.63	21.61	54.57	6.25
11	858.80	22.30	60.13	6.24
12	859.03	27.50	51.65	6.72

of mapping zenith range effect to lower elevation is very small. According to measured data (Table 4), the variations in the shape of the dry refractivity profile are insignificantly small for most of the troposphere. Thus a mean profile closely approximating the real data can be used to generate a standard table of scale factors. This table may then be used to map the dry zenith range error down to a 3-deg elevation angle within 3% uncertainty. After fitting the measured data with the previously derived function (Eqs. 9 and 10), a best-fit profile for the dry portion of the refractivity is found:

$$N_{\text{dry}} = 269\left(1 - \frac{h}{42.7}\right)^4, \qquad h \leq 12.2\,\text{km} \tag{15}$$

$$N_{\text{dry}} = 70\exp\left(-\frac{h - 12.2}{6.4}\right), \qquad h \geq 12.2\,\text{km} \tag{16}$$

Although the wet profiles were found to vary drastically from time to time, most of them seem to have similar monotonically decreasing shapes (Figs. 5 and 6). They can be approximated by the following expression without loss of significant accuracy, if the deviations in shape are not too great:

$$N_{\text{wet}} = N_S\left(1 - \frac{h}{13}\right)^4, \qquad h \leq 13\,\text{km} \tag{17}$$

$$N_{\text{wet}} = 0, \qquad h \leq 13\,\text{km} \tag{18}$$

In case of bad weather, when the shape of the profile from special balloon measurements is significantly different from the quartic profile of Eq. (17), a special ray tracing should be made for the mapping.

The above calibration, which is based on Berman's formula for zenith range correction from monthly mean parameters and the mapping table for range correction at lower elevation angles, was adopted as the new model for tropospheric correction for orbit determination during the Mariner Mars 1971 mission. The values of the standard mapping table can be found in Ref. 11.

D. Computation of Range Correction

The one-way range correction can be computed by the following expression:

$$\Delta\rho(\gamma) = \Delta\rho_{z_{\text{dry}}} R_{\text{dry}}(\gamma) + \Delta\rho_{z_{\text{wet}}} R_{\text{wet}}(\gamma)$$

where $R_{\text{dry}}(\gamma)$ and $R_{\text{wet}}(\gamma)$ are the ratios for mapping zenith range down to a given elevation ange γ. They can be obtained by interpolation from the standard mapping table given in Ref. 11. For approximate analysis, a simple formula can be used for the mapping:

$$\underset{\text{wet}}{R_{\text{dry}}} = \frac{1}{\sin\gamma + \dfrac{A}{\tan\gamma + B}} \tag{19}$$

$$\text{dry} \quad \begin{cases} A = 0.00143 \\ B = 0.0445 \end{cases}$$

$$\text{wet} \quad \begin{cases} A = 0.00035 \\ B = 0.017 \end{cases}$$

The two formulas above are good to within 1% from the ray trace range correction for an elevation angle higher than 1 deg. The value of the elevation angle γ can be computed from the following formula:

$$\sin\gamma = \sin\delta\sin\phi + \cos\delta\cos\phi\cos\omega t \tag{20}$$

where δ is the spacecraft declination, ϕ is the latitude of the tracking station, and t is the time past the station meridian. A simple computer subroutine is available for the tropospheric calibration of range and range rate based on the emprical equation (Eq. 19) when the four parameters are known. This program is not recommended for values below 1 deg of elevation angle.

References

1. Ondrasik, V. J., and Thuleen, K. L., "Variations in the Zenith Tropospheric Range Effect Computed From Radiosonde Balloon Data," in *The Deep Space Network*, Space Programs Summary 37-65, Vol. II, pp. 25–35. Jet Propulsion Laboratory, Pasadena, Calif., Sept. 30, 1970.

2. Miller, L. F., Ondrasik, V. J., and Chao, C. C., "A Cursory Examination of the Sensitivity of the Tropospheric Range and Doppler Effects to the Shape of the Refractivity Profile," in *The Deep Space Network Progress Report*, Technical Report 32-1526, Vol. I, pp. 22–30. Jet Propulsion Laboratory, Pasadena, Calif., Feb. 15, 1971.

3. Williams, J. G., "Very Long Baseline Interferometry and Its Sensitivity to Geophysical and Astronomical Effects," in *The Deep Space Network*, Space Programs Summary 37-62, Vol. II, pp. 49–55. Jet Propulsion Laboratory, Pasadena, Calif., Mar. 31, 1970.

4. Bean, B. R., and Dutton, E. J., *Radio Meteorology*, Monograph 92, p. 11, National Bureau of Standards, 1966.

5. Smith, E. K., and Weintraub, S., "The Constants in the Equation for Atmospheric Refractive Index at Radio Frequencies," *Proc. IRE*, Vol. 41, pp. 1035–1037, Aug. 1953.

6. Hopfield, H. S., "Two-Quartic Tropospheric Refractivity Profile for Correcting Satellite Data," *J. Geophys. Res.*, Vol. 74, No. 18, pp. 4487–4499, 1969.

7. Thuleen, K. L., and Ondrasik, V. J., "The Repetition of Seasonal Variations in the Tropospheric Zenith Range Effect," in *The Deep Space Network Progress Report*, Technical Report 32-1526, Vol. VI, pp. 83–98. Jet Propulsion Laboratory, Pasadena, Calif., Dec. 15, 1971.

8. Berman, A. L., "A New Tropospheric Range Refraction Model," in *The Deep Space Network*, Space Programs Summary 37-65, Vol. II, pp. 140–153. Jet Propulsion Laboratory, Pasadena, Calif., Sept. 30, 1970.

9. Hopfield, H. S., "Tropospheric Range Error at the Zenith," Preprint for 14th Plenary Meeting, July 1971, The John Hopkins University, Baltimore, Md.

10. Winn, F. B., Chao, C. C., and Leavitt, R. K., *TSAC Tropospheric Refraction Calibration Polynomials—Revised*, IOM 391.3-462, Sept. 22, 1971 (JPL internal document).

11. Chao, C. C., *Improved Estimation of the Parameters and Mapping Tables of Tropospheric Calibration for MM'71*, IOM 391.3-352, May 1971 (JPL internal document).

Time and Polar Motion

H. F. Fliegel and R. N. Wimberly

I. Introduction

This article discusses the time and polar motion calibration support provided to the MM'71 mission. Specifically, it describes the data-gathering system and the data-processing system by which calibrations were obtained. An introductory discussion of the effects of timing and polar motion error on spacecraft navigation, along with a description of the system used to support Mariners 6 and 7, is given in Ref. 1. A complete discussion of the way in which timing is used in orbit determination is given in Ref. 2.

The need for increased accuracy in determining Deep Space Network (DSN) coordinates to support MM'71 made necessary two major changes at JPL in obtaining timing and polar motion parameters. The first major change from the procedure used to support MM'69 was to secure astronomical data from a worldwide network of observatories rather than from the United States Naval Observatory (USNO) alone. The primary reason for this change was to obtain polar motion values with standard deviation not exceeding 0.7 m, according to the committed TSAC error budget. Polar position cannot be obtained by United States observatories alone. For many years, the Bureau International de l'Heure (BIH) had collected, reduced, and published polar motion and timing data from cooperating national time services throughout the world. However, the most recent published data have been from 40 to 70 days old, and errors due to extrapolating such data were often 1 to 3 m. Beginning in 1971, JPL sponsored a contract with BIH to obtain time and latitude data from at least 12 cooperating observatories by teletype, as soon as obtained, to provide the world's first rapid time and polar motion service. Another important benefit of this service was to reduce the random error in UT1 to less than 5 ms. Systematic errors of any one observatory tended to average out; bad weather in any one part of the world did not seriously affect the service; and real-time measurements of polar motion improved the accuracy of UT1, which was computed therefrom.

The second major change in JPL procedure was to replace the former TPOLY computer program with the PLATO system and a variety of supporting programs. Very stringent requirements were imposed on the ability of the system to detect bad data, to indicate sudden changes in the earth's rotation or in polar motion, and to avoid those "roller coaster" oscillations of a fitted curve which result from using higher-order terms in the fit that are not statistically significant. Since timing parameter decks were generated for this mission virtually on a real-

time basis, an error-free system, coupling a flexible output format with numerous internal and external checks for accuracy, became essential.

II. The BIH Rapid Time and Polar Motion Service

The Bureau International de l'Heure is the agency sponsored by the International Astronomical Union (IAU) and the International Union of Geodesy and Geophysics (IUGG) to collate, reduce, and publish timing data from all cooperating national time services throughout the world, and by means of such data to secure scientifically accurate and internationally accepted standards of time. The BIH receives support from the Federation of Astronomical and Geophysical Services (FAGS), which is assisted by UNESCO. By resolution of the IAU, BIH uses its astronomical data to solve both for UT1 and for the instantaneous coordinates X and Y of the terrestrial pole, which three quantities specify the orientation of the earth in space. Published final values of these quantities appear in BIH *Circular D* about one month after observation. However, since the causes of the variation of the earth's rotation are many and are not completely known, the parameters of that rotation, UT1, X, Y, cannot be predicted accurately in advance, and the time-lag between observation and publication had been a vexing source of error to many users. In particular, JPL could not use *Circular D* information for real-time mission operations. Therefore, Dr. Bernard Guinot, the director of BIH, decided to enlist the cooperation of a limited number of highly accurate time and latitude observatories to form the world's first rapid time and polar motion service. (The strategy is somewhat similar to that of the old Rapid Latitude Service, but the present service embraces time and polar motion in a single solution.)

One must distinguish between the astronomical service itself, which is exclusively a BIH function currently financed by JPL, and the use of the service to provide machine-readable timing and polar motion parameter decks suitable for space missions, which is a joint effort between BIH and JPL. We will speak of the former as the BIH Rapid Service, and of the latter as the JPL–BIH Operation.

The BIH Rapid Service hinges on the cooperation of a select list of observatories. Data from 76 observatories were included in the BIH *Circular D* solutions for time and/or latitude in 1969 (the year of the Mariner 6 and 7 missions), but the observatories were far from equal in weight. Weights in the BIH system are inversely proportional to the squares of the measured standard deviations of the data and are chosen to be the squares of integers; for example, in the timing solutions for the year 1969, ten stations had weight 49, ten had weight 25, six had weight 16, and the sum of the weights of all the rest was only 114. These weights, of course, are far greater for modern instruments observing stars of well-determined positions than for either the older types of visual instruments or for new observatories just beginning to establish their catalogs. Thus, the 10 observatories of weight 49 contribute more than half the total weight of the final solution for time, and a similar situation obtains for latitude. Therefore, an efficient and reasonably accurate rapid service can be organized by obtaining data by teletype from only those observatories of high weight. Furthermore, since the systematic errors of these observatories persist from year to year, they can be measured from the final solution for previous months and corrected in advance. Thus, the accuracy of the BIH Rapid Service can be made even greater than the weights of the contributing observatories alone would indicate. Such, then, is the strategy of the Service: first, to select for participation well-established observatories, and, second, to apply systematic corrections based on past performance. Note that even observatories which do not contribute directly to the Rapid Service are important to it, for they help determine the systematic corrections to those which do.

The BIH reduced the data from the observatories contributing to its Rapid Service by the same procedures it uses to prepare *Circular D* or the *Rapport Annuel*; thus all BIH publications are on the same system. Rapid Service reductions were made at 3.5-day intervals, rather than at the 5-day intervals used for *Circular D*. Each week until about mid-October 1971, BIH computed straight-line segments (initial values and rates) that characterized the behavior of X, Y, and UT1 during that week, and teletyped them to JPL. It was not practical for BIH to force the values at the beginning of one week to agree with the values at the end of the previous week, since raw time and latitude data are notoriously noisy, and frequently an apparent upward trend one week was shown by the following week's data to have been an illusion. Thus, straight-line segments were not joined at the ends; they constituted a discontinuous function. Near the end of October 1971, BIH proposed a slightly different operation. Rapid Service timing values were estimated for the current week according to a more or less continuous function; and, if new data showed that those values could be improved, a new set of estimates was sent for the same week. Thus, on November 11, 3 days

before encounter, BIH warned us that the earth had been slowing down more rapidly than previous estimates had showed, and that 5 ms should be subtracted from all previously teletyped values. One might compare the BIH Rapid Service to a Weather Bureau issuing a 48-h forecast, a 24-h forecast, and a 12-h forecast, with the understanding that a later forecast always supplants the earlier. The important point of difference is that one always knows what the weather is, and only the future is uncertain; but one does not know exactly what the earth is doing now because of the noise on the data, and even real-time estimates must be revised.

III. The JPL-BIH Operation: The PLATO System

The general requirements on timing and polar motion for all deep space mission support are as follows:

(1) The quantities UT1, X, and Y should be specified in the form of functions, readily computable, continuous in the first derivative.

(2) The precision of computation should be as high as the best available data warrants. For example, for the MM'71 mission, the standard deviations of the computed X and Y of polar position were not to exceed 0.7 m, and that of timing was not to exceed 4 ms.

(3) Parameters should be predicted and supplied as far in advance as possible, but it is especially important that unexpected changes in the earth's rotation be reported as rapidly as possible.

(4) Since the timing and polar motion routines form only a tiny part of the orbit determination program, and since no one person can have an intuitive feel for all the factors entering into a given day's solution for spacecraft position, it is essential that operations be fully automatic, with high redundancy and numerous safeguards to avoid error.

In order to accomplish these general requirements, we imposed the following special data reduction procedures for the MM'71 mission:

(1) All timing and polar motion data for mission operations were to be supplied in a single deck, called a PLATO deck (*PLAT*form *O*bservables). Each week during the normal cruise and orbiting phases of the mission, a new deck was issued, based on the latest data from BIH, supplanting the old deck. During a week prior to course correction or encounter, we received data daily from BIH over the NASA Communications Network (NASCOM) via London, and issued new decks daily when required. The NASCOM link proved so inexpensive and efficient that we stopped all commercial teletype messages by November 8.

(2) Verification of the BIH data would be accomplished by comparing their raw data from the United States Naval Observatory with our own independently collected data from the same sources. The BIH raw data consisted of copies of the data sheets submitted by each observatory (including the USNO) contributing to the Rapid Service. We then reduced the raw astronomical measurements of time and latitude to X, Y, and UT1 and compared these measurements to the data we normally get from the USNO at Washington and Richmond. The reduction was made by program THALES (*T*ime *H*andling *A*nd *L*atitude *E*valuation *S*ystem), which computes the check sums which verify that the data has been received properly, computes X, Y, and UT1 for each batch of data corrected to whatever epoch the operator supplies by NAMELIST input, and lists the residuals of each observation from the mean solution, computing the largest residual, the mean residual, and the standard deviation for each observatory.

(3) To avoid copying errors, only the original output deck from the 1108 computer was issued to mission personnel, and each such deck was checked for cards out of order, inconsistent labels, and the like by a program called CYNIC (*C*hecklisting *Y*es–*N*o *I*ndicator of *C*onsistency).

(4) To make certain that timing data could be delivered even in emergencies when the fairly intricate program PLATO might not be operable, a simple backup program was written called STOIC (*S*tand-by *T*iming *O*peration *I*n *C*ontingencies). Although STOIC has a very rigid output format with none of the versatility of PLATO, it proved faster to run and more nearly foolproof against operator error, and was used to generate PLATO-style decks beginning November 1, 1971.

IV. Performance of the JPL–BIH Operation

The following four sets of numbers characterize the precision of the operation.

(1) The standard deviations of the Rapid Service values received by teletype from the final values adopted by BIH and published in *Circulars D*.

From June through November, 1971, the standard deviations are

$$\sigma_X = 0''.0126 = 0.390 \text{ m}$$

$$\sigma_Y = 0''.0198 = 0.612 \text{ m}$$

$$\sigma_{UT1} = 2.23 \text{ ms} = 0.845 \text{ m at Goldstone}$$

(2) The standard deviations of the values for the current month on the PLATO decks delivered to the mission from the final values published in *Circular D*.

The values appearing on the 12 weekly decks issued from October 12 through December 22 give

$$\sigma_X = 0''.0078 = 0.241 \text{ m}$$

$$\sigma_Y = 0''.0149 = 0.461 \text{ m}$$

$$\sigma_{UT1} = 2.86 \text{ ms} = 1.08 \text{ m at Goldstone}$$

These sigma values can be smaller than those quoted under Item (1), above, because the Rapid Service numbers are raw values, whereas the PLATO decks contain values from the fit to a simple model contained in program STOIC. In fact, these sigma values are so small that the limit to the precision attainable by the DPODP (Double-Precision Orbit Determination Program) is set by the width of the interval over which the program performs Hermitian interpolation, an interval made three times wider for polar motion (in current operation, 3 months) than for timing.

(3) The standard deviations of extrapolated values given on PLATO decks from the final values published in *Circular D*.

Decks containing all data through the previous Tuesday were normally issued to mission personnel each Thursday, except during crucial mission periods, such as the week prior to maneuver (originally scheduled for October 26, 1971) and the week prior to encounter (November 14, 1971), when BIH data were received daily and a new deck issued. The daily service during crucial periods is required because extrapolation over 3 to 10 days would increase timing errors by 1 to 2½ ms and polar errors by 0.001 to 0.003 arc seconds (equal to 3 to 10 cm) in each coordinate. The additional polar error is negligible, but the timing error is not.

(4) The standard deviations of the final values adopted by BIH and published in *Circular D*, the standard of reference for the above three items, from the true values of time and pole.

Biases between BIH polar coordinates and those from other independent sources are typically 0.8 to 1.7 m (Ref. 3). Thus, the systematic errors in polar coordinates are expected to exceed the random errors by factors of 2 to 4. Systematic errors of 2 or 3 ms are expected to be introduced into BIH timing by catalog errors (Ref. 4); hence the systematic errors are about equal to the random errors.

V. Conclusions

The standard deviations of timing and polar motion information supplied to the MM'71 mission were cut to about half those of previous missions by means of the BIH Rapid Service and the PLATO system. Random errors in timing were at the 1-m level, and in polar coordinates were definitely below 1 m. Further improvements in navigational accuracy require a means of removing the systematic errors in the optical data by advanced techniques, such as VLBI.

We are continuing to generate timing decks on the same weekly schedule used to support Mariner 9. They are currently being used for Pioneer 10 navigation, advanced predictions for "moon-bounce" timing synchronization, lunar laser timing predictions, and the extended Mariner 9 mission.

References

1. Muller, P. M., and Chao, C. C., "Timing Errors and Polar Motion," in *Tracking System Analytic Calibration Activities for the Mariner Mars 1969 Mission,* Technical Report 32-1499, pp. 35–43. Jet Propulsion Laboratory, Pasadena, Calif., Nov. 15, 1970.

2. Moyer, T. D., *Mathematical Formulation of the Double-Precision Orbit Determination Program (DPODP),* Technical Report 32-1527. Jet Propulsion Laboratory, Pasadena, Calif., May 15, 1971.

3. Chao, C. C., and Fliegel, H. F., "Polar Motion: Doppler Determinations Using Satellites Compared to Optical Results," in *The Deep Space Network,* Space Programs Summary 37-66, Vol. II, pp. 23–26. Jet Propulsion Laboratory, Pasadena, Calif., Nov. 30, 1970.

4. Fliegel, H. F., and Lieske, J. H., "Inherent Limits of Accuracy of Existing UT1 Data," in *The Deep Space Network,* Space Programs Summary 37-62, Vol. II, pp. 46–49. Jet Propulsion Laboratory, Pasadena, Calif., Mar. 31, 1970.

N74-16985

Calibration Effects on Orbit Determination

G. A. Madrid, F. B. Winn, J. W. Zielenbach, and K. B. Yip

I. Introduction

This article discusses the effects of the charged particle and tropospheric calibrations on the orbit determination (OD) process. The preparation of these calibrations is discussed in separate articles in this report.[1] These articles describe the techniques used to obtain estimates of the group delay effects of the charged and neutral media on a radio signal. The calibration process consisted of correcting the doppler observables for the media effects.

Calibrated and uncalibrated doppler data sets were used to obtain OD results for past missions as well as Mariner Mars 1971. Comparisons of these doppler reductions show the significance of the calibrations. For the MM'71 mission, the media calibrations proved themselves effective in diminishing the overall **B**-plane[2] error and reducing the doppler residual signatures.

[1]"Charged Particles," by G. A. Madrid, and "The Tropospheric Calibration Model for Mariner Mars 1971," by C. C. Chao.

[2]A plane normal to the approach asymptote used to estimate aiming accuracy (see Fig. 1).

II. Charged Particle Calibration Results

The primary benefit of calibrating doppler for charged particle effects was expected to be the improvement of short arc solutions just prior to or subsequent to a maneuver. It was predicted that the Mariner 9 solutions at E − 30 days (final maneuver) would have a 1σ uncertainty of about 60 km due to charged particle effects over a 2-week span. Since the mission required an 83.3 km, 1σ navigation accuracy at this point, the calibrations promised to be a decisive factor in determining the parameters for this maneuver. The maneuver was never performed because Mariner 9 was well within the accuracy required at E − 30 days. Thus, the need to demonstrate the improvement that could be realized from a short-arc fit never arose. The most important test of the calibrations came during the fitting of a long arc of data (July 7 to September 26), which was collected prior to the scheduled maneuver date. Predictions for the long-arc effect placed the uncertainty at 33 km, 1σ. This is in accord with a study by Reynolds, Mottinger, and Ondrasik (Ref. 1), who predicted plasma effects for MM'71 of 18 km for a 32-day arc and 35 km for a 6-day arc, using simulated

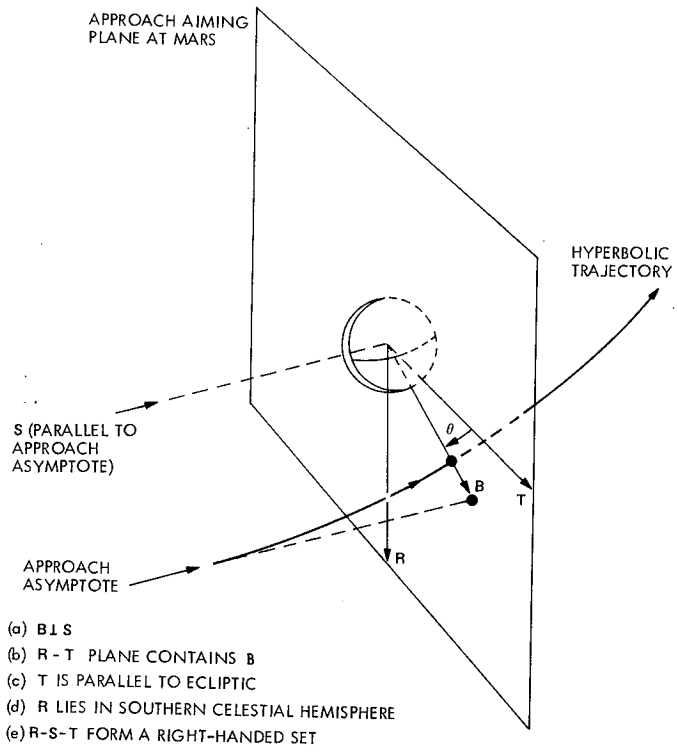

Fig. 1. Aiming plane coordinate system

data. For a particular short arc of 14 days reported in Section C, we observed changes in the targeting coordinated ranging from 180 to 200 km.

A. Calibration Strategy for Long Data Arcs

S. K. Wong, S. Reinbold, G. Sievers, and J. W. Zielenbach first applied charged particle calibration to the orbit determination of Mariner 9 in early July. They were able to calibrate 67 ten-minute doppler points acquired during June with differenced range vs integrated doppler (DRVID) data taken during the same period. Their results indicated that calibration of these 67 points changed the B-plane parameter estimate by 12 km in $\mathbf{B}\cdot\mathbf{R}$ and 10 km in $\mathbf{B}\cdot\mathbf{T}$ (a B-distance change of approximately 16 km). On September 27, the authors began calibrating all data in the span from July 7 to September 26 and determining the effects on the OD solutions.

The strategy for applying the calibrations was that Faraday rotation corrections would be used in lieu of DRVID for those passes where the DRVID data did not exist or was otherwise deficient.[3] Faraday rotation data was used extensively because of the lack of acceptable DRVID data.[4] To determine the effects of the calibrations, three types of runs (Table 1) were made over the same data:

(1) A set of runs using only the uncalibrated doppler.

(2) A set of runs using the calibrated doppler (combined DRVID and Faraday, and Faraday alone).

(3) A set of runs in which the calibrations were the only residuals, so as to isolate the calibration effects.

Two major sets of data were used to perform this study:

(1) Set DF contained all the doppler data from July 7 to September 26 for which either DRVID or Faraday calibrations were available.

(2) Set F contained all the doppler data from July 7 to September 26 for which Faraday calibrations alone were available.

Although these two sets have many points in common, there are differences due to the distinct acquisition pattern of the two types of calibrations.

To evaluate the calibrations at lower elevation angles, each of the above sets was considered both with 15 deg and 5 deg as the minimum allowable elevation angle γ_0.

Orbit determination solutions for these runs were obtained using the Orbit Determination Program (ODP) (Ref. 2). The solution parameter sets chosen for each of these runs are described in Table 2. The ODP solutions and statistics are dependent on the following weighting model (Ref. 2):

$$\sqrt{Weight} = \left\{\sigma_{i0}\left[1 + \frac{18}{(\gamma+1)^2}\right]\sqrt{\frac{60}{\tau_c}}\right\}^{-1}$$

where

σ_{i0} = the standard deviation associated with the data (hertz)

γ = the elevation angle (degrees)

τ_c = the count time (seconds)

Doppler observables acquired at the lower elevation angles are given less weight because of the greater uncertainties in the tropospheric and ionospheric effects.

[3]Doppler data was discarded outside the region of acceptable DRVID or Faraday rotation calibrations. Partial DRVID passes were not completed with Faraday rotation data.

[4]See "Charged Particles," by G. A. Madrid.

Table 1. Run identifications

Data type	Data set DF (combined calibration)		Data set F (Faraday only)	
	$\gamma_0 \geq 15$ deg	$\gamma_0 \geq 5$ deg	$\gamma_0 \geq 15$ deg	$\gamma_0 \geq 5$ deg
Uncalibrated doppler, $\sim$	$\widetilde{DF}_{15}$	$\widetilde{DF}_5$	$\widetilde{F}_{15}$	$\widetilde{F}_5$
Calibrated doppler, $\wedge$	$\widehat{DF}_{15}$	$\widehat{DF}_5$	$\widehat{F}_{15}$	$\widehat{F}_5$
Calibrations only, $\circ$	$\mathring{DF}_{15}$	$\mathring{DF}_5$	$\mathring{F}_{15}$	$\mathring{F}_5$

Table 2. Orbit determination solution parameter set

Solution	Parameter	ODP symbol[a]
A	Mariner 9 heliocentric state[b]	X, Y, Z, $\dot{X}$, $\dot{Y}$, $\dot{Z}$
B	Mariner 9 heliocentric state	X, Y, Z, $\dot{X}$, $\dot{Y}$, $\dot{Z}$
	Solar pressure	GR, GX, GY
	Mass of the earth's moon	GMM
C	Mariner 9 heliocentric state	X, Y, Z, $\dot{X}$, $\dot{Y}$, $\dot{Z}$
	Solar pressure	GR, GX, GY
	Attitude control force	ATAR, ATAX, ATAY
D	Mariner 9 heliocentric state	X, Y, Z, $\dot{X}$, $\dot{Y}$, $\dot{Z}$
	Solar pressure	GR, GX, GY
	DSS 12 location	CU12, CU12, LO12
	DSS 14 location	CU14, CU14, LO14
E	Mariner 9 heliocentric state	X, Y, Z, $\dot{X}$, $\dot{Y}$, $\dot{Z}$
	DSS 12 location	CU12, CU12, LO12
	DSS 14 location	CU14, CU14, LO14
	Mass of earth's moon	GMM
	Solar pressure	GR, GX, GY
F	Mariner 9 heliocentric state	X, Y, Z, $\dot{X}$, $\dot{Y}$, $\dot{Z}$
	Solar pressure	GR, GX, GY
	DSS 12 location	CU12, CU12, LO12
	DSS 14 location	CU14, CU14, LO14
	Attitude control force	ATAR, ATAX, ATAY
	Mass of the earth's moon	GMM

[a]ODP symbols used to represent parameters. A more detailed description of parameters is available in Ref. 2.

[b]Referenced to earth equator and equinox of 1950.0.

B. Analysis of Long-Arc Results

Tables 3 and 4 provide a compendium of the solutions obtained from the long-arc calibrations over the period from July 7 to September 26, 1971.

Table 3 presents the solutions for runs that use the actual doppler data ($\widetilde{DF}$, $\widehat{DF}$, $\widetilde{F}$, $\widehat{F}$). The results include the corrections to the **B**-plane coordinates $\mathbf{B}\cdot\mathbf{R}$ and $\mathbf{B}\cdot\mathbf{T}$ as well as the resultant correction to B. Table 4 tabulates the solutions obtained by treating the calibrations as the only residuals ($\mathring{DF}$, $\mathring{F}$).

To facilitate analysis, the results were plotted on the **B**-plane with arrows drawn from the uncalibrated doppler solutions to the calibrated solutions for each of the solve-for parameter sets defined in Table 2. Solid-line arrows connect solutions with 15 deg elevation angle data while the dotted-line arrows connect those that include data down to 5 deg.

Figure 2 presents the solutions using the combined DRVID and Faraday calibratable data set. Figure 3 shows the results for the data calibratable by Faraday data only. Figure 4 combines the information in Figs. 3 and 4 by differencing the combined data set (DP) effects from the Faraday only (F) effects. Figure 5 shows the $\Delta\mathbf{B}\cdot\mathbf{R}$ and $\Delta\mathbf{B}\cdot\mathbf{T}$ values that arise from cases $\mathring{DF}_5$, $\mathring{DF}_{15}$, $\mathring{F}_5$, and $\mathring{F}_{15}$ and indicates the contributions of the calibrations themselves.

The "C" and "F" solution sets are not represented in any of these plots because they were not felt to be realistic results. There were gas leaks present and the doppler-only arcs under investigation here could not determine them well. The "anomalous" solutions are predictable by covariance analysis, but an explanation of why the state behaves the way it does will require an in-depth study of the correlations between the calibrations and the attitude control and solar pressure forces in the data. The results of such a study will be reported at a later date.

In Fig. 2, the results with the set DF data indicate that calibrations cause the $\mathbf{B}\cdot\mathbf{R}$ coordinates to move from 10 to 35 km, depending on the solution set, and all the solutions except the "state only" (A) solutions converge to within 20 km of each other. It is of interest to note that all solutions except those with solar pressure parameters (B)

Table 3. Solutions for calibrated doppler

Solution	B	B·R	B·T
Case $\widetilde{DF}_{15}$			
A	8297.38	6111.08	5612.60
B	8307.16	6149.85	5585.64
C	8252.36	6187.51	5460.40
D	8301.78	6140.36	5587.08
E	8300.25	6139.65	5585.59
F	8269.59	6218.97	5450.74
Case $\widetilde{DF}_{5}$			
A	8301.21	6115.61	5613.32
B	8313.01	6162.89	5578.98
C	8272.02	6219.48	5453.84
D	8289.18	6126.97	5583.08
E	8290.59	6127.71	5584.36
F	8271.88	6209.83	5464.61
Case $\widehat{DF}_{15}$			
A	8314.01	6131.10	5615.36
B	8318.66	6162.83	5587.46
C	8240.51	6157.52	5476.40
D	8324.43	6170.34	5589.35
E	8325.64	6170.50	5589.38
F	8261.20	6203.17	5556.01
Case $\widehat{DF}_{5}$			
A	8315.95	6133.52	5615.59
B	8318.81	6166.29	5583.86
C	8271.98	6186.09	5491.62
D	8310.76	6154.03	5585.40
E	8311.32	6153.54	5586.66
F	8253.52	6177.54	5473.43

Solution	B	B·R	B·T
Case $\widetilde{F}_{15}$			
A	8327.54	6157.16	5606.91
B	8303.64	6158.24	5570.14
C	8314.98	6271.76	5459.30
D	8270.93	6120.32	5563.27
E	8290.97	6139.07	5572.43
F	8266.59	6229.73	5433.87
Case $\widetilde{F}_{5}$			
A	8336.12	6167.44	5608.36
B	8308.69	6167.65	5567.26
C	8404.10	6385.13	5464.34
D	8250.00	6092.97	5562.21
E	8266.11	6610.97	5570.76
F	8314.83	6314.14	5409.99
Case $\widehat{F}_{15}$			
A	8321.92	6148.30	5608.28
B	8302.74	6150.40	5577.46
C	8367.85	6281.44	5528.50
D	8260.64	6102.57	5567.48
E	8281.00	6121.63	5576.79
F	8303.09	6227.16	5492.15
Case $\widehat{F}_{5}$			
A	8324.71	6151.28	5609.15
B	8303.24	6152.52	5576.01
C	8463.12	6398.40	5539.41
D	8234.14	6068.56	5565.40
E	8250.19	6082.47	5574.98
F	8356.53	6312.15	5476.16

have a very small component of change in the **B·T** (equivalent to right ascension) direction.

In Fig. 3, the solutions decrease from the uncalibrated position by 10 to 30 km, again depending on the solution set selected. The solutions here remain dispersed at about 100 km of one another in the **B·R** direction and within 10 km in the **B·T** direction.

One is tempted to attribute the difference between the uncalibrated solutions of Figs. 2 and 3 to the difference in the number and location of data points in sets DF and F. However, in Fig. 3, we see that for the "state only" (A) solutions, the calibrations move the results for the different data sets to within 20 km of each other. We must conclude that the previous difference in results using two data sets was due more to the absence of calibrations on the noncommon points than to the location of the noncommon points themselves. Although the solutions sets B, D, and E do not demonstrate the same behavior, this may be understandable because none of their additional parameters is particularly well determined in this portion of the cruise. A more substantial explanation will derive from further analysis.

An evaluation of the absolute accuracy of the calibrations relative to the aim plane was not possible, due to the lack of a standard. The most accurate determination of the spacecraft's final position on the **B**-plane prior to insertion was based on a trajectory whose terminus was within the radius of influence of Mars and that utilized a more precise planetary ephemeris. Other estimates based on data arcs roughly corresponding to ours obtained solu-

Table 4. Solutions for calibrations only

Solution	ΔB	Δ(B•R)	Δ(B•T)
Case $\mathring{DF}_{15}$			
A	21.56	21.48	1.26
B	21.50	21.30	−2.96
C	51.08	16.79	43.18
D	26.92	26.45	−4.99
E	26.91	26.46	−4.92
F	12.95	−2.39	12.73
Case $\mathring{DF}_{5}$			
A	16.42	16.40	0.87
B	5.88	5.88	0.21
C	77.12	12.98	76.02
D	19.22	18.68	−4.53
E	19.18	18.66	−4.47
F	36.14	−25.11	25.99
Case $\mathring{F}_{15}$			
A	1.83	0.11	1.83
B	3.35	1.85	2.79
C	142.60	75.13	121.21
D	32.81	−32.54	−4.17
E	31.94	−31.72	−3.77
F	92.73	22.98	89.84
Case $\mathring{F}_{5}$			
A	14.45	−14.30	−2.06
B	13.02	−11.56	6.00
C	156.60	80.78	134.16
D	44.79	−44.39	−5.97
E	44.47	44.09	−5.79
F	101.71	18.90	99.94

tions within the area of our solutions, but because of differences in their application they were not considered suitable for this purpose. It may be noted that the predictions of the long-arc effects for MM'71 (33 km) were corroborated, in that we observed effects averaging 30 km.

A plan for establishing a standard has been devised, and a program for establishing the absolute accuracy of these calibrations will be undertaken in conjunction with our ongoing investigation into the short-arc effects.

C. Preliminary Short-Arc Results

A study of the effect of the ionosphere alone was performed on data obtained in the period from November 1, 1971 to November 14, 1971. Tests were first run without including the day of encounter (November 14, 1971) and then inclusive of that day's data. The effects of ionospheric

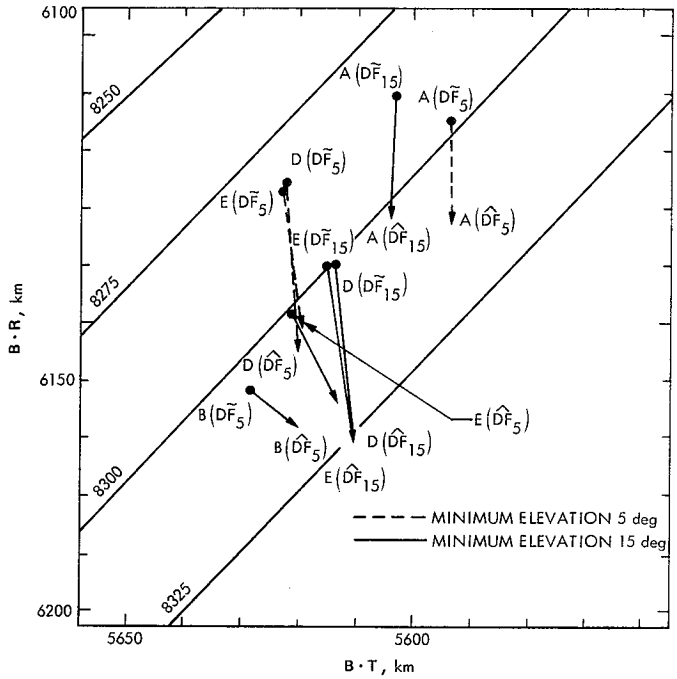

Fig. 2. Charged particle effects on MM'71 B-plane solutions (Combined DRVID and Faraday calibrations)

charged particles on the OD solution were determined by replacing the actual doppler residuals with the expected effect on the doppler observables. These estimates of the effects were derived from Faraday rotation data taken at DSS 13.

The results of this short-arc study indicate that if the data just prior to encounter is not included, ionospheric calibrations could cause changes in the targeting plane that exceed 200 km (state only solution, Table 5). When the solution set includes the observing station's location parameters the changes in the targeting plane remain at a 180-km level. The latter result merely indicates that the state and station parameters were insufficiently correlated with the ionospheric effects to be absorbed into the solution. Inclusion of the encounter data produced a more predictable result, namely, that charged particle effects on navigation became negligible due to the increased influence of the planetary mass on the trajectory.

D. Conclusions

The preceding discussion has established the effectiveness of charged particle calibration for both long- and short-arc fits. The long-arc fit made over a period of 80 days showed changes of from 20 to 35 km in the targeting plane. The 14-day short-arc fit indicated possible effects

Table 5. Ionospheric effect on state and station location solutions in the OD process

Solution	Parameter	Ionospheric effect		Magnitudes of **B** vectors	
		Nov. 1–Nov. 13 arc	Nov. 1–Nov. 14[a] arc	Nov. 1–Nov. 13 arc	Nov. 1–Nov. 14 arc
A[b]				8217.40 km	8396.20 km
	X	169.50 km	−3.26 km		
	Y	−478.51 km	−421.53 km		
	Z	344.67 km	590.69 km		
	$\dot{X}$	-0.126×10^{-4} km/s	-0.162×10^{-5} km/s		
	$\dot{Y}$	0.118×10^{-4} km/s	-0.312×10^{-4} km/s		
	$\dot{Z}$	0.157×10^{-3} km/s	0.125×10^{-3} km/s		
	B•T	−232.38 km	0.173 km		
	B•R	−16.52 km	−0.570 km		
B[c]				8344.61 km	8396.50 km
	X	−535.79 km	8.30 km		
	Y	386.10 km	−19.97 km		
	Z	−48.76 km	14.07 km		
	$\dot{X}$	0.557×10^{-5} km/s	-0.618×10^{-6} km/s		
	$\dot{Y}$	-0.112×10^{-3} km/s	0.136×10^{-5} km/s		
	$\dot{Z}$	-0.667×10^{-4} km/s	0.499×10^{-5} km/s		
	B•T	−182.83 km	−0.024 km		
	B•R	114.47 km	−0.001 km		
	Δr_s[d]	2.30 m	3.52 m		
	$\Delta\lambda$[e]	−4.12 m	4.92 m		

[a]Mars encounter on Nov. 14, 1971.
[b]State only.
[c]State and station location.
[d]Distance from the spin axis.
[e]Longitude of the DSS.

of from 180 to 200 km if the day immediately preceding encounter was not included in the fit.

The long-arc effects, while substantially smaller in magnitude than those for the short arc are important in that they demonstrate the consistency and convergence of OD solutions where charged particle effects have been applied. The short-arc results, while requiring further study, indicate that fits over short data spans late in the mission, especially after a maneuver, could be critical in determining the accuracy of planetary approach.

III. Tropospheric Refraction Calibration Results

The effectiveness of the new tropospheric seasonal model was evaluated by tests prior to and during the MM'71 mission. Corrections produced by this model were applied to both simulated and real tracking data during the OD process. The results of these tests indicate that:

(1) The new model is, in fact, an improvement over that used in past missions.

(2) The real data fits reveal that the new model does not remove all of the elevation observed minus computed observables (O−C) residual signature believed due to refraction.

(3) The calibrations are more important for short data arcs (10 days) than for long data arcs (30 days).

A. A General Consideration: Residual Signatures

All doppler data acquired at low terrestrial elevations (< 25 deg) exhibit elevation-dependent signatures. These

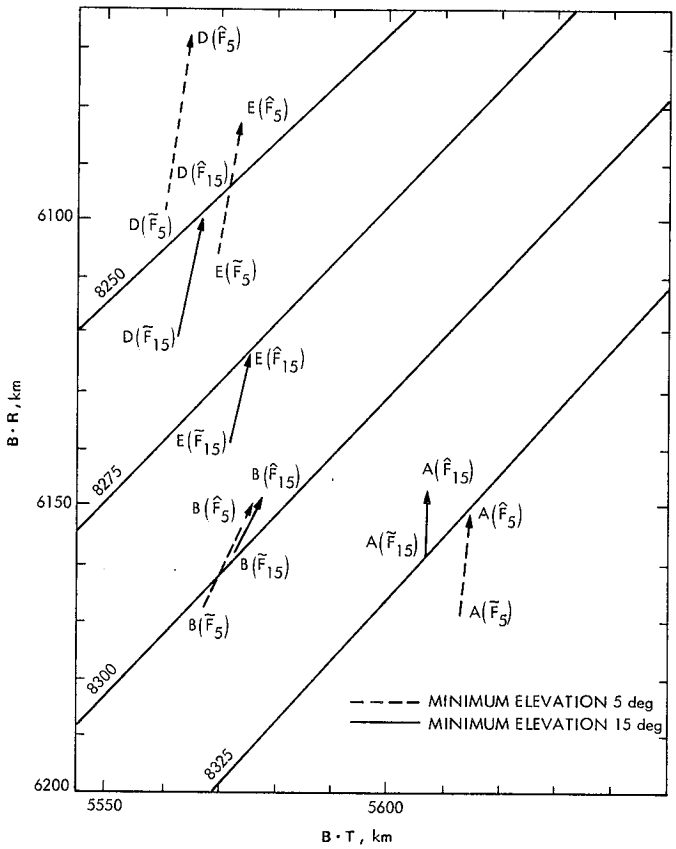

Fig. 3. Charged particle effects on MM'71 B-plane solutions (Faraday calibrations only)

PARAMETER SET CODE	MINIMUM ELEVATION 15 deg		MINIMUM ELEVATION 5 deg	
	UNCALIBRATED	CALIBRATED	UNCALIBRATED	CALIBRATED
A	DF 46.08 F -5.69	DF 17.20 F -7.08	DF 51.83 -4.96 F	DF 17.76 F -6.44
B	DF +18.39 F -14.5	F -12.43 DF -10.0	DF 4.76 -11.72 F	F -13.77 DF -7.85
D	CONVENTION ΔB · R, km; ΔB · T, km; F -20.04 DF -23.81	F -67.77 DF -21.87	F -34.0 DF -20.87	F -85.47 DF -20.0
E	F -0.58 DF -13.16	F -48.8 DF -10.59	F -20.74 DF -13.6	F -71.17 DF -12.18

PARAMETER SET CODES:

A = STATE ONLY

B = STATE, SOLAR PRESSURE, MASS OF MOON

D = STATE, SOLAR PRESSURE, DSS LOCATION

E = STATE, SOLAR PRESSURE, DSS LOCATION, MASS OF MOON

VECTOR REPRESENTS RESULTANT OF ΔB · R AND ΔB · T DUE TO CHANGE FROM F TO DF SET

DIRECTION OF VECTOR INDICATES SIGN OF CHANGES

Fig. 4. Comparison of charged particle B-plane effects upon changing from the Faraday set (F) to the combined data set (DF) of doppler data

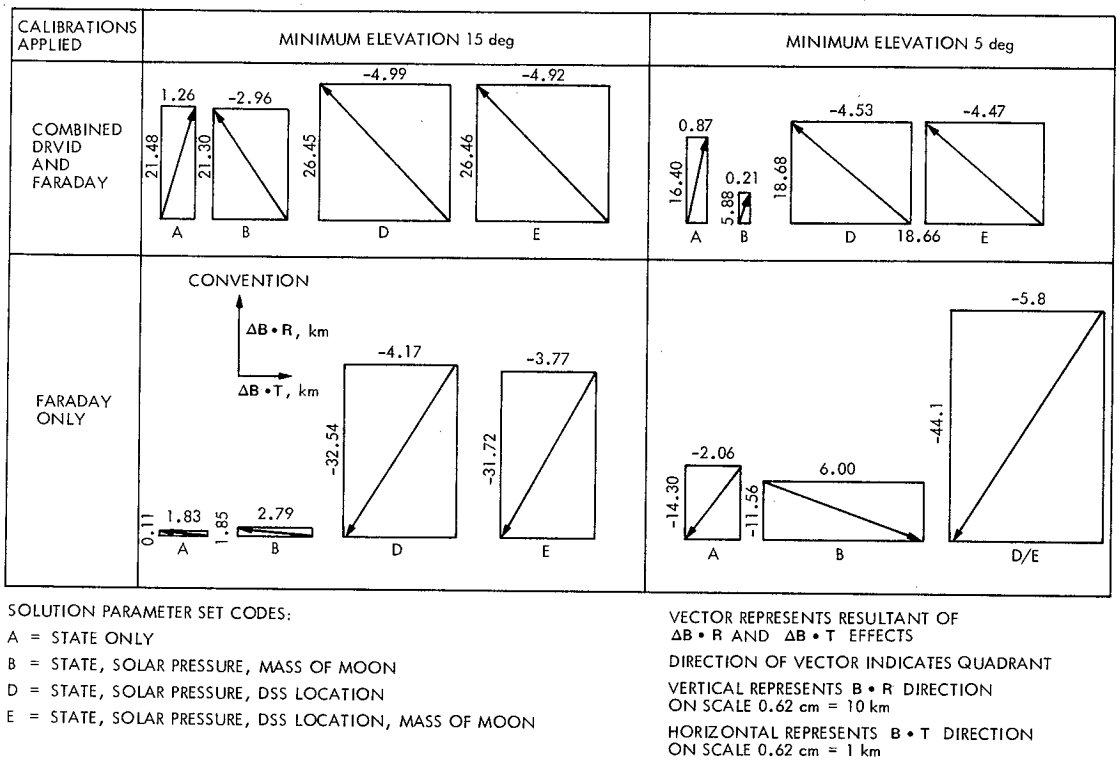

Fig. 5. Charged particle effects as seen on B-plane for various solution sets

elevation-dependent structures are present in the after-the-fit residuals of the tracking data of all past missions examined—Mariners 2, 4, 5, and 6, Surveyors 1, 2, 3, 5, 6, and 7, and the Lunar Orbiters (Ref. 3).

Terrestrial error sources known to produce such doppler error signatures are the troposphere and ionosphere. Other unknown error sources may exist—and most certainly do—but it is solely refraction that is under investigation here and other error sources are not considered in the real tracking data analysis.

B. Comparison With Past Missions

The after-the-fit, doppler O−C residuals from the Surveyors reveal elevation-dependent structures. These structures are present (1) regardless of the ODP[5] solution parameter set chosen, and (2) despite the application of tropospheric refraction[6] and ionospheric charged particle[7] calibrations of the doppler data.

[5]Only parameters of JPL's ODP are investigated (Ref. 4).

[6]Tropospheric refraction is modeled by the MM'71 refraction calibration algorithm (Refs. 5, 6).

[7]Faraday rotation data, provided by the Stanford Radio Science Laboratory, is used to calibrate charged particle effects on the doppler.

Table 6 shows the second moment (μ_2), $\Sigma(O-C)^2/n$, of residuals resulting from least-square fits to 14-day arcs of 2-way, S-band doppler radiometric data from Surveyors 5, 6, and 7. All the doppler was calibrated for charged particle effects. The solution parameters were:

$\lambda_{\mathbb{C}}$ = selenographic longitude of lunar landed Surveyor

$\phi_{\mathbb{C}}$ = selenographic latitude of lunar landed Surveyor

λ_{DSS} = geocentric longitude of the DSS

$r_{s_{DSS}}$ = distance of the DSS from the earth's spin axis

The second moments, μ_2, are reduced on the average by 70% when the MM'69 refraction model is replaced by the MM'71 model. It is of interest to note that when 14 days of doppler data are fit using the above parameter set, some elevation-dependent doppler O−C residual structure exists regardless of the refraction model used. The amount of this O−C structure is nonetheless smaller for the MM'71 refraction model.

When the DSS coordinates are the sole solution parameters, the 14-day arcs behave similarly. However, as one

Table 6. Difference between MM'71 − MM'69 refraction models seen in the second moment of doppler data residuals

Surveyor	Second moment of doppler residuals in Hz²	
	MM'69 algorithm	MM'71 algorithm
5	0.849×10^{-5}	0.187×10^{-5}
6	0.135×10^{-5}	0.418×10^{-6}
7	1.950×10^{-5}	0.819×10^{-5}

decreases the number of days in the fit, the signature associated with any individual pass diminishes until, in the limit, the single-pass fits do not have any apparent residual structures after the fit. This stems from the increased ability of the DSS coordinate parameters to absorb this type of error as the data arc is shortened.

Figure 6 presents the second moment of the residuals from Surveyor 6 as a function of length of data arc. It shows that after the data set is increased to approximately 14 days or more, the pass-by-pass contribution to μ_2 is nearly constant. All the Surveyor data processed behaves this way. The solution parameters are insensitive to refraction-induced doppler error signatures for fits including 14 or more days of data.

In an attempt to study the insensitivity to refraction alone, without the effect of other modeling errors, the actual Surveyor residuals were replaced by fictitious ones that represented the differences between the calibrations predicted by MM'69 and MM'71 refraction models for these data. Table 7 shows that as the length of the data set is increased from one to 14 passes, the size of the parameter adjustments decreases.

When the coordinates of the landed probe are the solution parameters, the same behavior is evident. The data reductions for Surveyor 6 show the effect of the refraction modeling change as a function of the number of passes quite clearly (Fig. 7). Due to the relatively high linear correlation between $\lambda_{\mathbb{C}}$ and $\phi_{\mathbb{C}}$ for Surveyors 5 and 7, however, the parameter changes do not decrease as well as might be predicted.

The declination changes experienced by all of these Surveyors over the two-week periods that the doppler data was acquired from each amounts to almost 50 deg. These declination changes alter the doppler-refraction effects dramatically from pass to pass over the fit interval. The doppler-refraction effects are fairly repetitive from

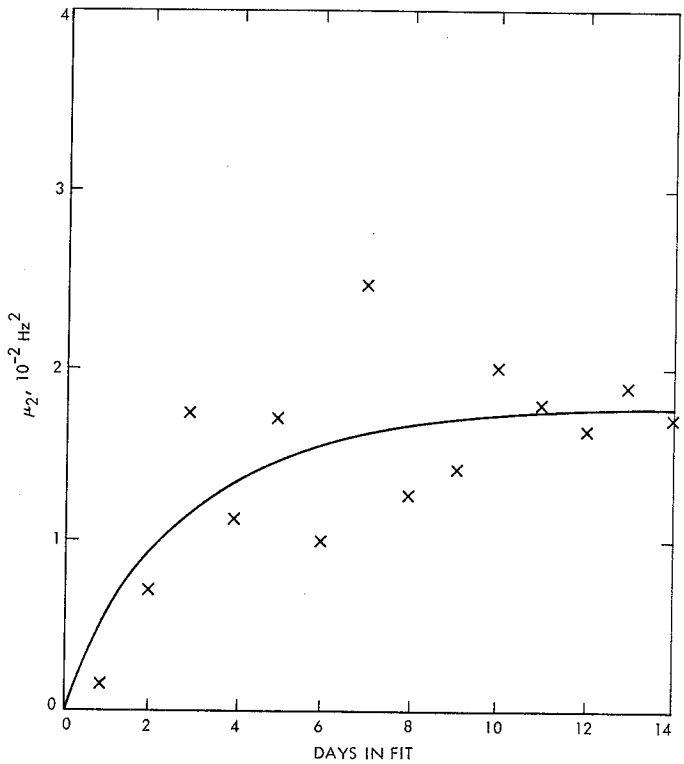

Fig. 6. Surveyor 6 300-s doppler data at DSS 11

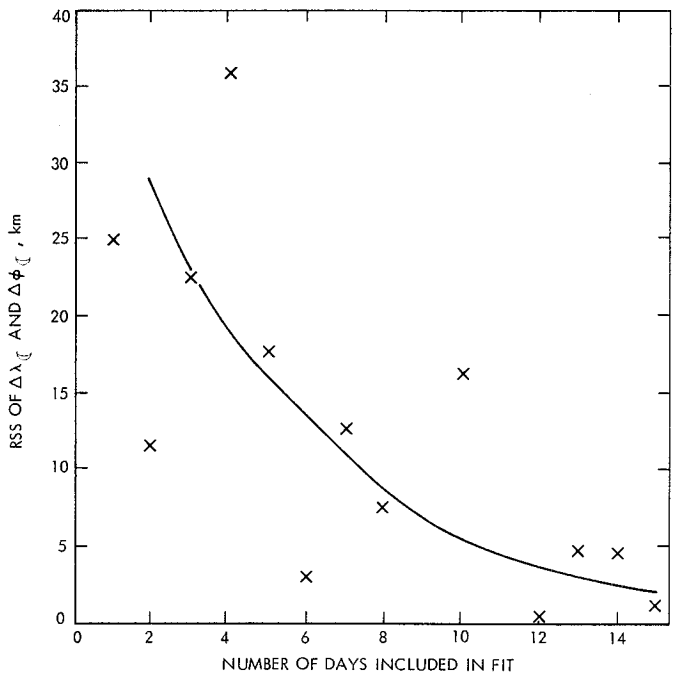

Fig. 7. $\lambda_{\mathbb{C}}$ and $\phi_{\mathbb{C}}$ adjustments due to MM'69-MM'71 refraction modeling differences

pass to pass for doppler data acquired from a spacecraft during planetary cruise for time periods on the order of a few weeks.

The effect of using different refraction models was also tested on the MV'67 spacecraft state estimates. The extent to which the state estimate is altered by the refraction modeling change depends on the length of the data-arc fit and the parameters adjusted. Figure 8 shows the MV'67 state adjustments due to the difference in models plotted as a function of arc length. To simplify this discussion, state parameter only solutions are presented.

The doppler data set being fit spans the time interval of June 25 to August 20, 1967. The doppler used is calibrated for charged particle influences using the Faraday polarization data provided by the Stanford Radio Science Laboratory. The data (600-s, count-time doppler) was acquired at DSS 14.

The doppler is sub-divided into the following sets:

Set	Date, 1967	Total days
1	June 25 to July 2	7
2	June 25 to July 9	14
3	June 25 to July 16	21
4	June 25 to July 23	28
5	June 25 to July 30	35
6	June 25 to August 6	42
7	June 25 to August 13	49
8	June 25 to August 20	56

Each doppler set is used to estimate the MV'67 spacecraft geocentric, cartesian state at the June 25, 1967, epoch.

When the entire 56-day period is fit at one time, the μ_2 associated with the MM'71 refraction model is ~50% less than the μ_2 associated with the MM'69 refraction model.

The significance of this improvement can be found if the difference between the two models is projected into the state parameter space. For the 56-day fit, the root-sum-square (RSS) positional error amounts to ~11 km and the RSS speed error is $\sim 7 \times 10^{-5}$ km/s.

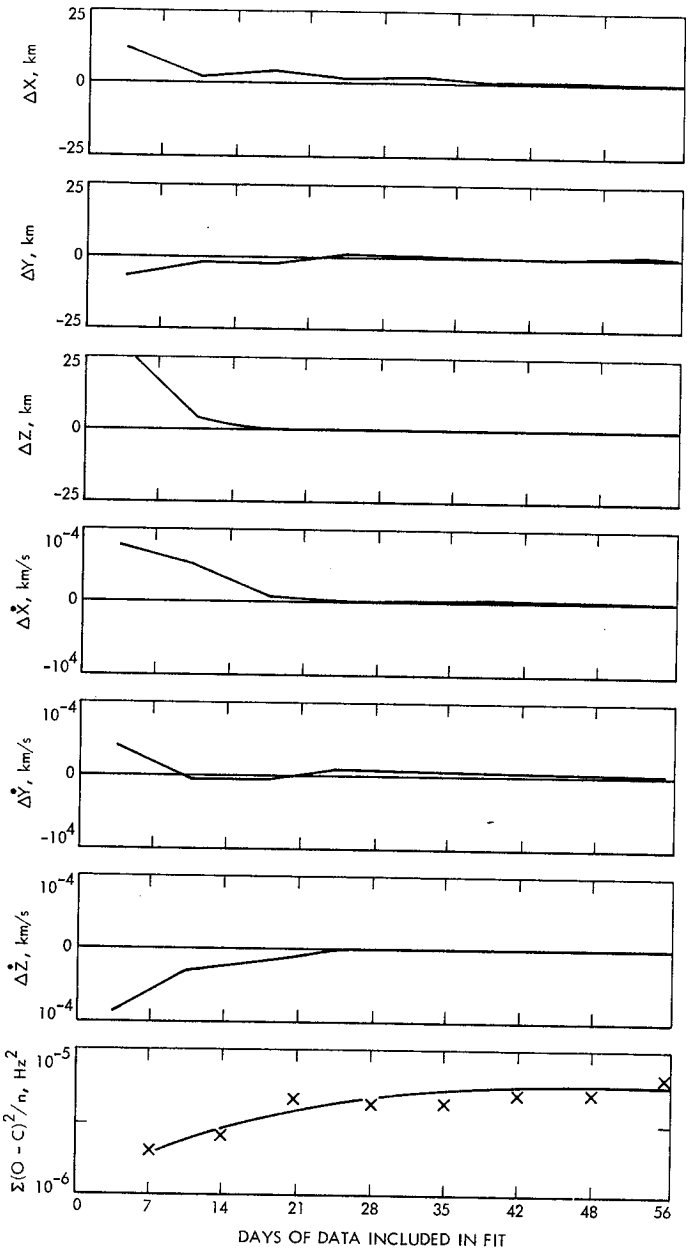

Fig. 8. MV'67 cruise state adjustments due to differences in tropospheric refraction models as a function of arc length

If shorter time periods of the doppler arc were fit, the results of Fig. 8 are obtained. This figure shows the individual state parameter adjustments for the different data-arc fits. Also, the μ_2 of each fit are shown. In general, the message is similar to the theme presented for the Surveyors. The state parameters are most sensitive to refraction modeling errors when short data arcs are fit. The preponderance of the elevation-dependent signature remains in the residuals after the fit.

Table 7. DSS coordinate adjustments as a function of number of tracking data passes included in doppler fit[a]

Number of passes	Surveyor 5		Surveyor 6		Surveyor 7	
	$\Delta r_{s_{11}}$, m	$\Delta\lambda_{11}$, m	$\Delta r_{s_{11}}$, m	$\Delta\lambda_{11}$, m	$\Delta r_{s_{11}}$, m	$\Delta\lambda_{11}$, m
1	–	–	−6.7	+0.4	−1.4	+12.9
2	–	–	−5.2	+0.8	−3.1	+7.7
3	−5.9	+17.6	−3.9	+0.4	−1.8	+2.9
4	+9.2	+20.1	−10.7	+6.0	–	–
5	−11.3	+14.4	−4.8	+0.3	–	–
6	–	–	−5.1	−1.2	–	–
7	–	–	−1.5	+3.1	−2.9	+1.4
8	–	–	−1.7	−0.6	+1.5	−0.7
9	–	–	−0.6	−0.1	+0.9	+0.0
10	−2.0	+3.7	+0.3	−0.3	+0.6	+0.0
11	+0.2	−2.6	+0.5	−0.1	+0.5	+0.1
12	–	–	+0.7	−0.0	+0.7	+0.0
13	+1.4	−2.3	+0.0	−0.0	–	–
14	+0.9	−1.1	+0.8	+0.0	+0.1	+0.0
15	–	–	+0.4	−0.0	–	–

[a]All the doppler data of Surveyors 6 and 7 are calibrated for ionospheric charged particle effects. Surveyor 5 doppler has not been so calibrated.

Table 8. Projection of the MM'71 – MM'69 refraction differences into MM'71 state parameter estimates

Parameter	Displacement		
	7-day data arc	14-day data arc	21-day data arc
ΔX	30.6 km	53.2 km	34.6 km
ΔY	−283.0 km	158.8 km	81.4 km
ΔZ	−108.4 km	141.6 km	64.5 km
$\Delta\dot{X}$	-0.288×10^{-4} km/s	0.749×10^{-5} km/s	-0.520×10^{-5} km/s
$\Delta\dot{Y}$	0.964×10^{-4} km/s	0.511×10^{-4} km/s	-0.133×10^{-4} km/s
$\Delta\dot{Z}$	-0.220×10^{-5} km/s	0.144×10^{-4} km/s	-0.182×10^{-4} km/s
μ_2	0.745×10^{-5} km/s	0.144×10^{-4} km/s	0.250×10^{-4} km/s
	28-day data arc	35-day data arc	42-day data arc
ΔX	29.8 km	15.2 km	4.3 km
ΔY	−18.7 km	−7.7 km	−3.9 km
ΔZ	29.2 km	9.1 km	2.7 km
$\Delta\dot{X}$	-0.500×10^{-5} km/s	-0.800×10^{-6} km/s	0.417×10^{-6} km/s
$\Delta\dot{Y}$	-0.128×10^{-4} km/s	-0.977×10^{-5} km/s	-0.270×10^{-5} km/s
$\Delta\dot{Z}$	0.165×10^{-4} km/s	0.179×10^{-4} km/s	0.211×10^{-4} km/s
μ_2	0.279×10^{-4} km/s	0.281×10^{-4} km/s	0.284×10^{-4} km/s

C. MM'71 Mission: Earth-Mars Cruise

This study is based on the Goldstone doppler data acquired during the interval from July 7 through September 26, 1971; since, for this period of time, calibrations were available to effectively remove the effects of the earth's ionosphere. Figure 9 shows that portion of the trajectory under study and Fig. 10 provides a measure of the zenith range error[8] that stems from the "wet" and "dry" ideal-atmosphere components (Ref. 5).

When the MM'71 refraction model replaced the MM'69 model, the μ_2 of the doppler residuals was reduced by 70%. The 1σ doppler residual associated with a 600-s count time (doppler observation at 10 deg elevation) was changed from 2.5–3 mm/s to 0.9–1.0 mm/s, a change that amounts to an improvement of ~30%.

Let us now examine how the difference between the two refraction models projects into the solution parameter space for the MM'71 spacecraft state estimates. Table 8 shows the adjustments corresponding to six different data sets. Those results indicate that the MM'71 spacecraft state estimates tend to be "most" sensitive to refraction in the short-arc solutions in a root-sum-square sense. And, as with the other missions discussed, the μ_2 and the elevation-dependent residual structure for the individual passes increase as the data-arc length is increased. In the MV'67 results, for example, μ_2 for the Goldstone-Mariner 9 pass of July 9, 1967 is 0.245×10^{-5} for the one-week fit, 0.376×10^{-5} for the two-week fit, 0.595×10^{-5} for the four-week fit, and 0.893×10^{-5} for the six-week fit. There is a greater than 300% increase between the one-week and six-week fits for the same pass. The July 9, 1967 pass was chosen for this comparison for it has doppler from 7-deg elevation angle (near rise) to 11-deg elevation angle (near set). The μ_2 of the total residual sets associated with the six different fits (Table 8) similarly shows more and more of the refraction errors not to be fitted out as the data-arc length is increased.

[8]Group velocity retardation incurred by a radio signal traveling the atmosphere at the observer's zenith.

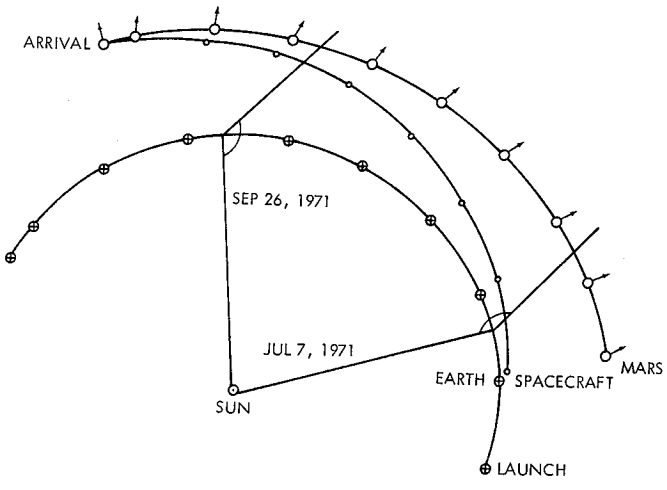

Fig. 9. MM'71 mission geometry

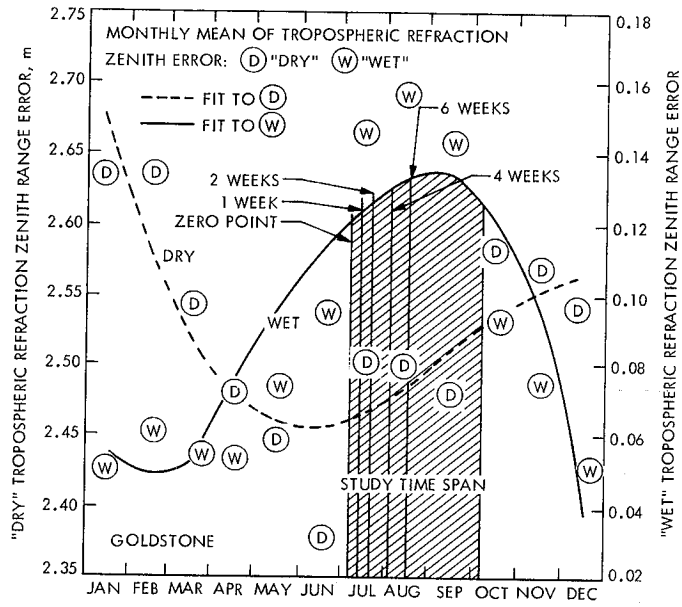

Fig. 10. Tropospheric refraction zenith range errors for the different arc solutions

Although the MM'71 refraction model demonstrated a dramatic improvement in reducing the tropospheric effects in the doppler residuals, an after-the-fit, elevation-dependent signature was still evident (see Fig. 11). *If* it is assumed to be refraction calibration error solely, then the July 7, 1971, doppler error indicates a +10% overcorrection at 10 deg elevation. The doppler error for July 19, 1971, indicates a −12% undercorrection. These apparent over- and undercorrections do not, however, correlate significantly with surface weather data acquired at DSS 14, indicating that a significant segment of investigation yet remains to be accomplished.

IV. Summary

Elevation-dependent residual structures in doppler tracking were reduced by employing a temporal model for tropospheric refraction effects. When the doppler-data arc being fit is short (two weeks or less), the distortion of

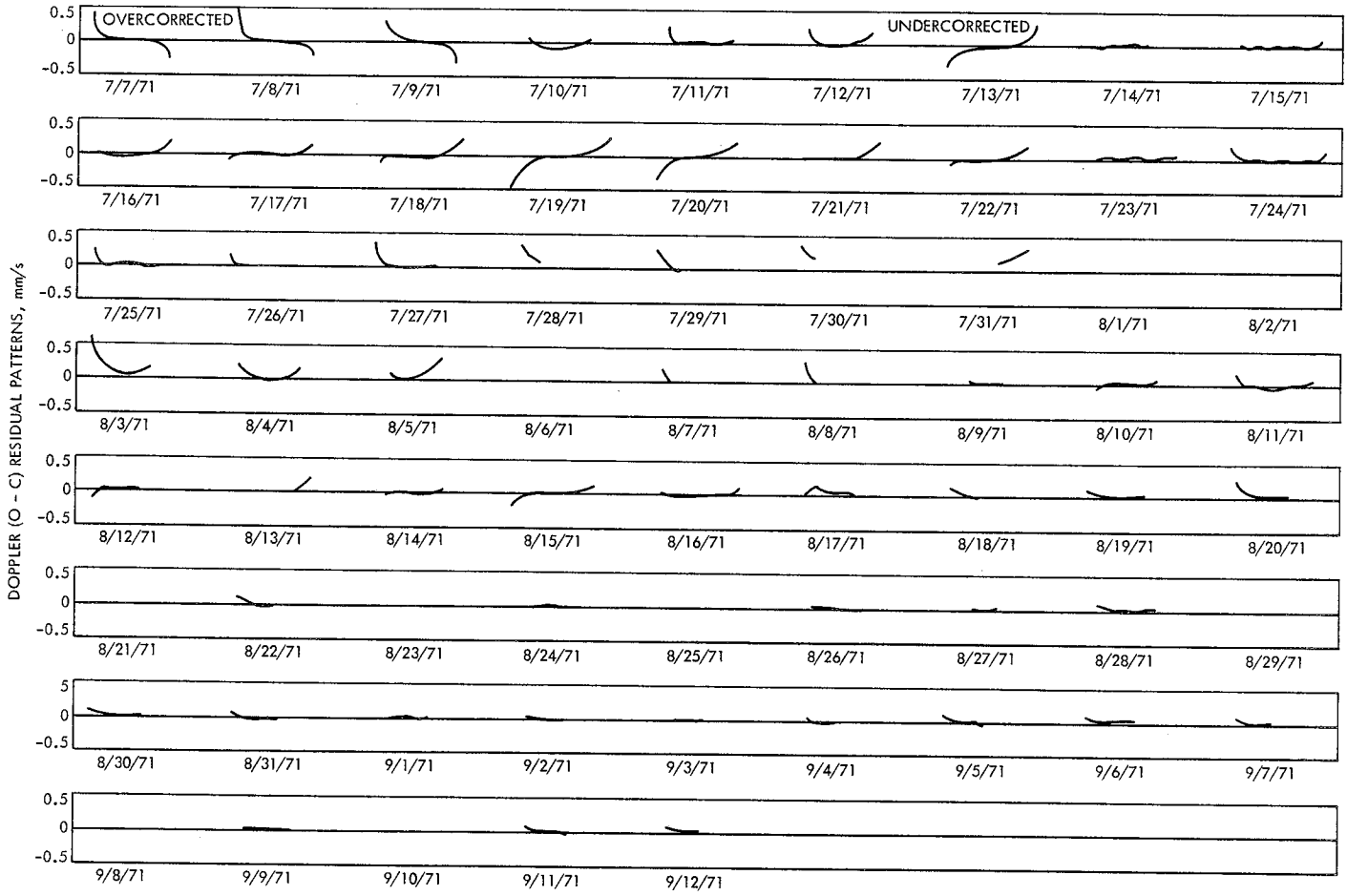

Fig. 11. The elevation-dependent-type structure in the after-the-fit doppler (O – C) residuals, pass by pass

the spacecraft state estimate due to tropospheric refraction is noticeable. As the length of the data-arc is extended to 4 to 6 weeks, the sensitivity of the state to the refraction phenomena diminishes such that errors in modeling are not critical (as long as the model is temporal). Accordingly, the second moment associated with a fit to a data arc in excess of four weeks shows that the spacecraft parameters are unable to absorb much of the relatively short term, "observed-minus-computed" doppler signatures. Static models not only fail to accurately represent the tropospheric effects on doppler but also extremely distort the state estimate for short data-arc lengths.

References

1. Reynolds, G. W., Mottinger, N. A., and Ondrasik, V. J., "An Example of the Space Plasma Effect on the Mariner Mars 1971 Encounter Accuracy," in The Deep Space Network, Space Programs Summary 37-62, Vol. II, pp. 24–28. Jet Propulsion Laboratory, Pasadena, Calif., Mar. 31, 1971.

2. Warner, M. R., "Double Precision Orbit Determination Program," 900-56, EPD-426, Jet Propulsion Laboratory, Pasadena, Calif., Nov. 1966 (JPL internal document).

3. Winn, F. B., and Leavitt, R. K., "Refractivity Influence on DSS Doppler Data," in The Deep Space Network Progress Report for November and December 1970. Technical Report 32-1526, Vol. I, pp. 31–41. Jet Propulsion Laboratory, Pasadena, Calif., Feb. 15, 1971.

4. Moyer, T. D., Mathematical Formulation of the Double-Precision Orbit Determination Program (DPODP), Technical Report 32-1527. Jet Propulsion Laboratory, Pasadena, Calif., May 15, 1971.

5. Chao, C. C., A Model for Tropospheric Refraction Calibration from Daily Surface and Radiosonde Balloon Measurements, Internal Technical Memorandum 391-350. Jet Propulsion Laboratory, Pasadena, Calif., Aug. 8, 1972 (JPL internal document).

6. Winn, F. B., Chao, C. C., and Leavitt, R. K., "TSAC Tropospheric Refraction Calibration Polynomials, Revised," Interoffice Memorandum 391.3-462, Jet Propulsion Laboratory, Pasadena, Calif., Sept. 22, 1971 (JPL internal document).

N74-16986

Polynomial Smoothing of DRVID Data

R. K. Leavitt

I. Introduction

Charged-particle calibrations based on Differenced Range Versus Integrated Doppler (DRVID) are smoothed and fitted with a polynomial prior to its application in the orbit determination process. This article describes the results of the tests performed on the computer program performing these calculations to determine its characteristics and to evaluate the acceptability of its computations. This program, called MEDIA, is described in Ref. 1. A more detailed version of this analysis may be found in Ref. 2.

MEDIA employs a least-squares curve fitting process that automatically determines the appropriate degree of polynomial required to optimize the fit. This process uses an iterative technique in which the data points are smoothed with a moving least-squares polynomial. In each successive iteration, every datum is replaced by the value taken on by this polynomial, which is computed from a subset of k points centered at the point to be replaced. Its degree and the number of points k of the subsets are determined from the total number of data points in the pass.

After each smoothing iteration, the first, second, etc., finite differences of the resulting smoothed points and each of their variances are computed until the minimum variance is determined. When the minimum variances from two successive iterations occur for the same (say, the mth) finite differences, then a statistical F-test is used to compare them.

The smoothing process is ended when the F-test is satisfied. A least-squares polynomial of degree m is then fitted to the smoothed points. A statistical runs test is performed on the original data relative to this fit to detect those cases in which the DRVID data do not resemble a polynomial. When the test fails, the degree is increased, a new fit is computed, and the runs test is again performed with the new fit. This process is repeated until either the test has been satisfied or the degree of fit exceeds its maximum allowable value.

The following two conditions must be satisfied by the data in order to use this process:

(1) The data must occur at equal time intervals.

(2) The data should usually resemble a polynomial.

The first condition is imposed to simplify and to speed up the processing logic. Without it, the computer run time required to process a pass of data would be prohibitive.

The second condition is obvious, since the objective of the process is to fit a polynomial to the points. Violations of this condition should be detected and overcome by the runs test that is applied. Such occurrences, however, should be infrequent; otherwise, the processing time would become excessive.

This curve-fitting technique is not applied unless there are at least 16 data points. If there are fewer then 16 points but at least three, a least-squares polynomial is fit directly to the points. Its degree is set at the largest integer contained in the square root of the number of points.

II. Test Results

Various sets of both simulated and real data were processed by the MEDIA program to evaluate and to demonstrate its curve-fitting ability. The simulated sets provided a controlled situation in which the parameters were known. The real sets were used to demonstrate how the process would function in a real-life situation. A comparison with Faraday rotation calibration polynomials was also performed.

The following paragraphs describe various statistical tests that are performed on the least-squares fits that result from this process. These tests include the chi-square over degree of freedom, linear regression, and analysis of covariance. The primary parameter used in these tests is the variance of the points about the polynomial fit to them. For simulated data, this variance is compared to the known variance that was artificially constructed in the data. For real data, it is compared with the variance of the actual noise in the radiometric data. In comparing the resulting polynomials with Faraday rotation calibration polynomials, the mean and variance of the differences of the derivatives of the corresponding polynomials are analyzed.

A. Simulated Data

Two equations were used to synthesize DRVID data: a cubic and a tenth-degree polynomial. These equations are defined as

$$\Delta\rho(t) = 1 + t + t^2 + t^3$$

$$\Delta\rho(t) = 0.15 + 0.15t + 0.15t^2 + \cdots + 0.15t^{10}$$

The cubic equation is used to produce three cases of 100 points each by superimposing on it 0-, 5-, and 10-ns Gaussian noise. For the 5- and 10-ns noise cases, the variance s^2 of the data points about the least-squares polynomial is an efficient parameter for testing the fit (Ref. 3). The statistic used is s^2/σ^2, where σ is either 5 or 10 ns. The distribution of s^2/σ^2 is the chi-squared over degree of freedom (χ^2/df) density function (Ref. 4). The 10% level of confidence is used for this test so that the requirements for rejecting the fit are not too stringent.

The acceptance criteria for 100 points are

$$0.777 < s^2/\sigma^2 < 1.24$$

The following tabulation summarizes the results of this test:

σ	s	s^2/σ^2
5	4.53	0.821
10	10.41	1.083

Both are within the acceptance criteria; therefore, both fits are acceptable according to the test.

The tenth-degree polynomial was chosen to produce a curve with a relatively steep slope. A 10-ns noise was superimposed on this curve to obscure its slope. It is believed that DRVID data may behave in a similar manner in extreme cases.

Samples of 125, 250, and 500 evenly spaced points over the interval $-1 < t < 1$ were taken, converted to DRVID data, and used as input. The variances about these poly-

nomials were subjected to the χ^2/df test. The results are summarized below:

Points	s	s^2/σ^2	Criteria
125	11.23	1.26	0.801–1.22
250	10.24	1.05	0.858–1.15
500	10.38	1.08	0.898–1.11

Although s^2/σ^2 is within the acceptance criteria for the samples of 250 and 500, it is not for the 125-point sample. These results seem to indicate that the sample rate should be increased as the noise increases to detect local or irregular trends in the data.

In conclusion, the results from the simulated data demonstrate that the process is performing in an acceptable manner, except possibly for extreme and unlikely cases. In such cases, the user will have to override the process by specifying the degree of fit. Input options built into the process make such action possible.

B. Real Data

Mariner Mars 1971 (MM'71) is the primary source of real data used to evaluate the curve-fitting ability of the process in an actual data-processing environment. The early part of the flight, when MM'71 was relatively close to earth, was selected for the evaluation to minimize the number and effect of the variables involved and to make the analysis easier. Figure 1a shows a typical fit produced for day 188. The derivative of this fitted polynomial is shown in Fig. 1b. The least-squares polynomials produced appear to reasonably represent the data points in each pass, and their derivatives seem believable, except possibly at some of the ends of the passes. The data points in these cases exhibit slight trends at the ends of the passes that probably would disappear in the smoothing process if the passes were extended.

The variances of the deviations of the points from the fitted polynomials are used to evaluate the fits as in the case of simulated data. They are a measure of the dispersion of the data caused by noise in the received signal. The fit is considered to be good if the resulting variance is an accurate measure of this dispersion. Table 1 lists the statistics for the tracking passes early in the flight that are used in this evaluation. In the last column on the right,

Table 1. Dispersion about the least-squares fits

Day	N	s	$1/s^2$	dBmW
188	417	0.5183	3.7225	35.71
189	245	0.5639	3.1448	34.98
191	370	0.6387	2.4514	33.89
195	146	0.8261	1.4653	31.66
198	415	0.8681	1.3270	31.23
199	423	0.9024	1.2280	30.89
200	209	0.9500	1.1080	30.45
201	363	0.9992	1.0016	30.01
204	423	1.1967	0.6983	28.44
205	424	1.1850	0.7121	28.53
207	401	1.3839	0.5221	27.18
208	384	1.4145	0.4998	26.99
209	423	1.5839	0.3986	26.01
210	227	1.4439	0.4796	26.81

the variances have been converted to dBmW units (Ref. 5), which are comparable to units of power, i.e.,

$$\mu_2 = 10 \log_{10} \frac{s^{-2}}{0.001}$$

where μ_2 is the inverse of the variance in dBmW units and s^2 is the variance.

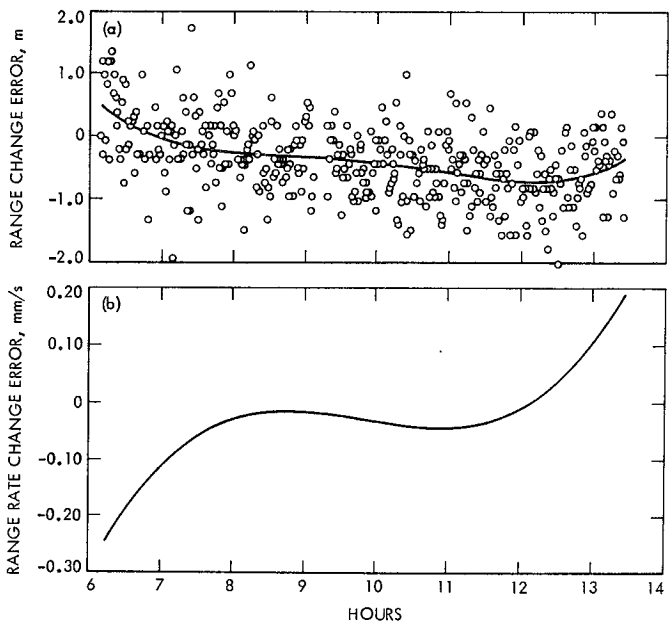

Fig. 1. Typical least-squares fit (a) and derivatives of polynomial fit (b) to DRVID data

The dispersion due to noise is related to the power received at the tracking stations; the less power received, the greater the dispersion (assuming everything else is equal). The following tabulation lists the expected power received at Deep Space Station 12 at 5-day intervals:

Day	Power, dBmW
186	−163.7
191	−165.3
196	−166.8
201	−168.9
206	−170.9
211	−173.0

The relationship between these values and the variances of the deviations from the least-squares polynomials is what will be evaluated.

Linear regression lines and correlation coefficients (Ref. 4) were computed for both the inverse of the variances (dBmW units) and the power received versus days. Their slopes b, correlation r, and 95 percentiles ρ_{95} of the r distribution are listed below:

	Points	b	r	ρ_{95}
Power	6	−0.3737	−0.9977	0.729
Variance	14	−0.4163	−0.9931	0.457

Since $|r| > \rho_{95}$ in both cases, it is concluded that both sets are correlated with days.

The slopes of the two regression lines were compared using the analysis of covariance technique (Ref. 6). If there is no significant difference between these slopes, then the variances are related to the dispersion of the tracking data received at the stations. The F-distribution is used to test the slopes. The required equations are summarized below:

	Sum of squares	*Degrees of freedom*
Denominator	$\sum_{i=1}^{k} \sum_{j=1}^{n_i} (y_{ij} - a_i - b_i x_{ij})^2$	$\sum_{i=1}^{k} (n_i - 2)$
Numerator	$\sum_{i=1}^{k} \sum_{j=1}^{n_i} (x_{ij} - x_i)^2 (b_i - b)^2$	$k - 1$

where

$k = 2$ is the number of data sets

$n_i = 6, 14$ is the number of points in the ith set

(x_{ij}, y_{ij}) are the points

x_i is the mean of the x-values in the ith set

a_i is the y-intercept of the ith set

b_i is the slope of the ith set

and

$$b = \frac{\sum_{i=1}^{k} \sum_{j=1}^{n_i} (x_{ij} - x_i)^2 b_i}{\sum_{i=1}^{k} \sum_{j=1}^{n_i} (x_{ij} - x_i)^2}$$

The F-ratio that results from these equations is

$$F = \frac{1.993}{0.655} = 3.93$$

From the F-distribution tables at the 95% confidence level,

$$F(16, 1) = 4.50$$

Since $3.93 < 4.50$, it can be concluded that the two slopes are the same. Thus, the dispersion of the deviations about the fit is an accurate measure of the noise in the data, and the fits adequately represent DRVID data.

C. Derivatives of the Least-Squares Polynomials

The derivatives of the least-squares polynomials must accurately represent the rate of change of the charged-particle media. It is the rate of change that is important in the calibration of the doppler tracking data. The accuracy of these derivatives is evaluated here using Faraday rotation data (Ref. 7), which measure the charged-particle content of the ionosphere. They are obtained by passing a signal from a stationary satellite through the ionosphere to a tracking station and mapping the results to the line-of-sight of the spacecraft. They should be comparable to DRVID data when the spacecraft is close to earth and the ionosphere is practically the only source of charged particles. The Faraday calibration polynomials used for this comparison were computed by the digital computer program ION (Ref. 7).

Figure 2a and 2b illustrates the derivatives that result from fits to the MM'71 DRVID and Faraday rotation data and the differences between them for a typical day included in this evaluation. The ends of the Faraday derivatives have been deleted from the graphs and from the evaluation because of their erratic and unrealistic movements. The oscillations that are so pronounced in the graphs of the differences are caused almost entirely by the Faraday derivatives. The relatively large differences at the ends of the curves probably result from the end points phenomenon of the DRVID derivatives, as noted earlier. Table 2 lists the statistical parameters from these graphs that are used in the numerical analysis that follows. The last column on the right presents the inverses of the variances in dBmW units. A linear regression line and correlation coefficient were computed for these variances (dBmW units) versus days to determine whether there is any relation between them and the dispersion of DRVID data. The results are summarized below:

$$N = 14$$

$$b = -0.141$$

$$r = -0.261$$

$$\rho_{95} = 0.457$$

Table 2. Statistics of the differences between the derivatives of DRVID and Faraday rotation calibration polynomials

Day	N	x	s	$1/s^2$	dBmW
188	438	0.026	0.046	472.59	56.74
189	250	0.023	0.097	106.28	50.27
191	377	0.022	0.105	90.70	59.58
195	150	−0.176	0.150	44.44	46.48
198	432	0.022	0.066	229.57	53.61
199	432	0.005	0.043	540.83	57.33
200	215	−0.053	0.132	57.39	47.59
201	368	0.042	0.077	168.66	52.27
204	233	−0.105	0.159	39.56	45.97
205	123	0.132	0.077	168.66	52.27
207	436	−0.061	0.090	123.46	50.91
208	436	0.071	0.077	168.66	52.27
209	436	−0.036	0.061	268.74	54.29
210	298	−0.032	0.084	141.72	51.51

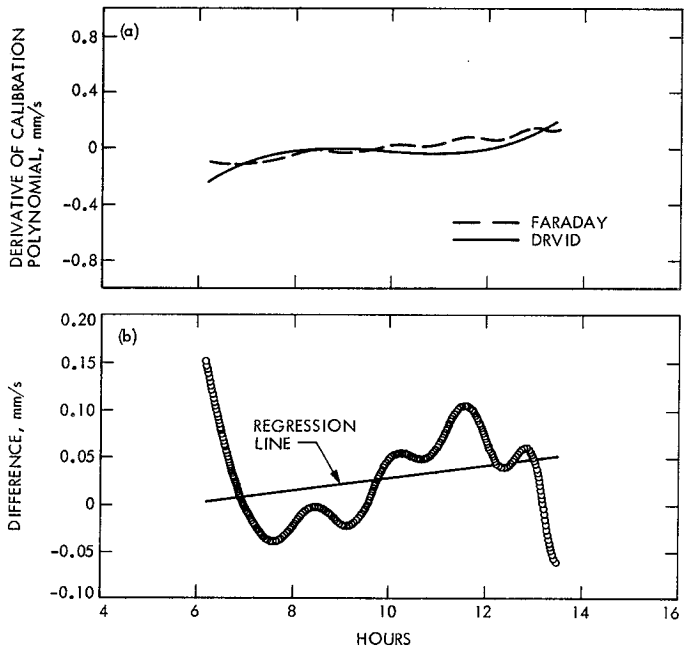

Fig. 2. Comparison (a) and difference (b) between derivatives of polynomials fitted to DRVID and Faraday data

Since $|r| < \rho_{95}$, the variances are not correlated with days; i.e., the slope b of the regression line is not significantly different from zero. Therefore, the differences of the derivatives are not related to the dispersion of the DRVID data or to the signal noise, both of which (as noted above)

are correlated with days and have the same slope. This result indicates that the least-squares process has successfully filtered the noise from the data.

From the values in Table 2, the total mean and standard deviation of the differences of derivatives are −0.0031 and 0.0881 mm/s, respectively. Although the mean is relatively small, the standard deviation does indicate a rather large spread considering the size of the derivatives. However, computing error percentages at this time does not seem worthwhile since it is not known whether DRVID or Faraday contributes the greater error. A more profitable approach might be to apply these calibrations to a simplified orbit determination process and evaluate its convergence.

In conclusion, the derivatives of the resulting DRVID calibration polynomials are acceptable provided the tracking passes are not overly short in duration. The successful filtering of random noise from the data has minimized the dangers inherent in computing derivatives of raw data such as these. This accomplishment is one of the most important results of the process. Another significant attribute of the process is the fact that it has not introduced into the fit such distortions as "ringing" or other similar deformations, which too often appear in least-squares polynomial approximations. Such distortions are often amplified in the derivatives of these polynomials to the extent that the subsequent application of the derivatives is impractical. Although the differences between the derivatives of DRVID and Faraday polynomials have what seems to be a relatively large dispersion, they do average out as indicated by the small total mean. This anomaly is not yet fully understood; however, there are several likely causes that might contribute to it:

(1) The end points phenomenon.

(2) The mapping of the Faraday rotation calibrations to the spacecraft line-of-sight.

(3) The lack of pronounced trends in the DRVID data. (The data used in this evaluation were all sampled during the "flat" portion of the ionosphere's diurnal charged-particle content curve.)

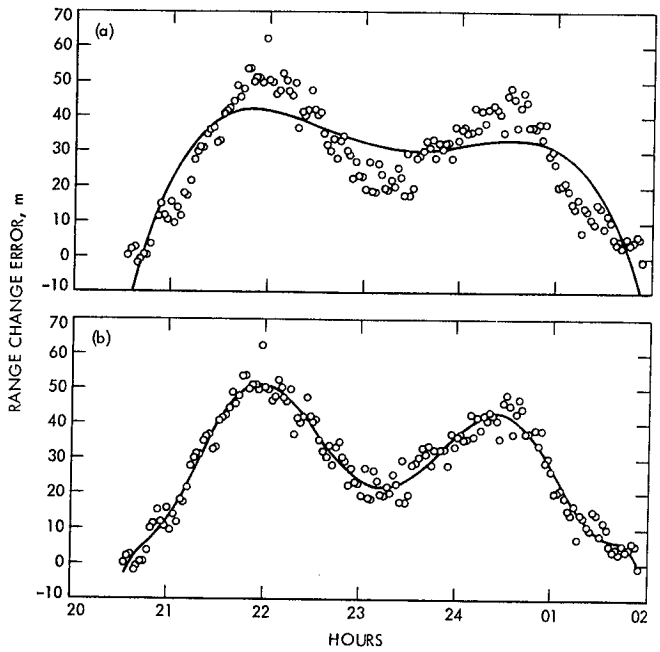

Fig. 3. Least-squares fit without (a) and with (b) runs test applied

D. Statistical Runs Test

The need for a statistical runs test is demonstrated in Fig. 3a. As shown in this figure, the least-squares process determined that a fourth-degree polynomial would fit the points. Their configuration, however, is such that this degree is not adequate. An exponential function would probably fit these points better than a polynomial.

The runs test, upon detecting such situations, causes the degree to be increased until the test is satisfied. In this example, a tenth-degree polynomial was required to fit the points adequately enough to satisfy the test. The resulting fit is shown in Fig. 3b.

References

1. Leavitt, R. K., *DEPD, Transmission MEDIA, A Subassembly of the Tracking System Analytical Calibration Assembly (TSAC), Phase A*, Document DEPD 315-59, Jet Propulsion Laboratory, Pasadena, Calif., Jan. 1971 (JPL internal document).

2. Leavitt, R. K., *The Least-Squares Process of MEDIA for Computing DRVID Calibration Polynomials*, Technical Memorandum 33-542, Jet Propulsion Laboratory, Pasadena, Calif., May 15, 1972.

3. Hildebrand, F. B., *Introduction to Numerical Analysis*, McGraw-Hill Book Co., Inc., New York, N. Y., 1956.

4. Dixon, W. G., and Massey, F. J., *Introduction to Statistical Analysis*, McGraw-Hill Book Co., Inc., New York, N. Y., 1957.

5. Ryder, J. D., *Electron Engineering Principles*, Prentice-Hall, Inc., Englewood Cliffs, N. J., 1952.

6. Mood, A. M., *Introduction to the Theory of Statistics*, McGraw-Hill Book Co., Inc., New York, N. Y., 1950.

7. Mulhall, B. D., et al., "The Ionosphere," in *Tracking System Analytic Calibration Activities for the Mariner Mars 1969 Mission*, Technical Report 32-1499, pp. 45–68, Jet Propulsion Laboratory, Pasadena, Calif., Nov. 15, 1970.